Shock-wave structure for a polyatomic gas with large bulk viscosity

Shingo Kosuge[1] and Kazuo Aoki[2,3]

[1]*Center for Global Leadership Engineering Education, Graduate School of Engineering, Kyoto University, Kyoto 615-8540, Japan*
[2]*Mathematics Division, National Center for Theoretical Sciences, National Taiwan University, Taipei 10617, Taiwan*
[3]*Department of Mathematics, National Cheng Kung University, Tainan 70101, Taiwan*

The structure of a standing plane shock wave in a polyatomic gas is investigated on the basis of kinetic theory, with special interest in gases with large bulk viscosities, such as CO_2 gas. The ellipsoidal statistical model for a polyatomic gas is employed. First, the shock structure is computed numerically for various upstream Mach numbers and for various (large) values of the ratio of the bulk viscosity to the shear viscosity, and different types of profiles, such as the double-layer structure consisting of a thin upstream layer with a steep change and a much thicker downstream layer with a mild change, are obtained. Then, an asymptotic analysis for large values of the ratio is carried out, and an analytical solution that describes the different types of profiles obtained by the numerical analysis, such as the double-layer structure, correctly is obtained.

I. INTRODUCTION

A shock wave is described as a discontinuous surface, across which the density, the velocity normal to the surface, and the temperature of a gas exhibit jumps in inviscid gas dynamics. In reality, however, the shock wave has a structure; that is, physical quantities undergo steep but continuous changes across a thin layer of a few mean free paths. To describe such a structure, one has to use, in principle, kinetic theory of gases instead of ordinary gas dynamics.

The structure of a standing plane shock wave is one of the most fundamental problems in kinetic theory and has been investigated by many authors experimentally [1–3], theoretically [4,5], and numerically [6,7] (see also, e.g., Refs. [8–13]). In the present study, we consider this classical problem with special interest in polyatomic gases with large bulk viscosities, such as carbon dioxide (CO_2) gas.

Recently, the shock-structure problem was investigated for polyatomic gases on the basis of extended thermodynamics [14–16], and some interesting results were obtained. In Ref. [14], relatively weak shock waves were considered, and it was shown that for CO_2 gas, macroscopic quantities exhibit profiles of three different types (types A, B, and C in Refs. [14–16]), depending on the upstream Mach number, as shown by the schematic density profile in Fig. 1. When the Mach number is very close to 1, i.e., the shock wave is very weak, the profiles of the density, velocity, and temperature are almost symmetric with respect to the centers of the respective profiles (type A). When the Mach number is increased slightly, the profiles become nonsymmetric and exhibit a corner upstream (type B; the corner is not a real corner but is *almost* a corner). If the Mach number is increased slightly more, one obtains profiles with a double-layer structure, consisting of a thin front layer with a steep change and a thick rear layer over which the quantities slowly approach the downstream equilibrium values (type C). In the present paper, we borrow the notation types A, B, and C from Ref. [14]. The type-C profiles have been obtained also for higher Mach numbers ($M_- = 1.3$, 3, and 5, where M_- is
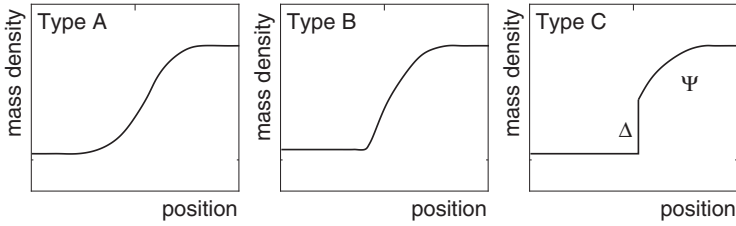
FIG. 1. Schematic figure of the profiles of types A, B, and C. The figure is a reproduction of Fig. 1 in Ref. [14] (courtesy of S. Taniguchi).

the Mach number at upstream infinity) on the basis of the nonlinear extended thermodynamics [16]. The existence of the type-C profiles had been known for a long time [17–19]. The reader is referred to Refs. [14,16] and references therein.

In Ref. [16], the authors make some effort to validate the nonlinear extended thermodynamics for polyatomic rarefied gases in strong nonequilibrium conditions. In addition, the macroscopic equation (with 14 macroscopic variables) used in Ref. [14], which was derived by the extended thermodynamics in Ref. [20], is shown to be obtained [21] also from the Boltzmann equation, with a modeling of the internal modes by a single continuous variable [22], by a moment closure. Nevertheless, it would be important and interesting to confirm the results of Refs. [14,16] directly from kinetic theory. As mentioned in Refs. [14,16], however, it is not an easy task because of the extreme complexity of the collision integral of the Boltzmann equation for a polyatomic gas. This obliges us to introduce phenomenological models at some point in the theory or numerical analysis. Nevertheless, it is still an interesting problem to see whether type-A, B, and C solutions appear or not for the CO_2 gas on the basis of kinetic theory. This was the motivation of our preliminary note [23].

In Ref. [23], we adopted, as the basic equation, the polyatomic version of the ellipsoidal statistical (ES) model [24], which was proposed in Ref. [25] and was rederived in a systematic way in Ref. [26] (note that it is different from the model for a polyatomic gas proposed in Ref. [24]). This model has a simple structure in which the internal degrees of freedom are expressed by an additional (continuous) energy variable associated with the internal modes. Although it is simple, it satisfies the basic properties of the Boltzmann equation for a polyatomic gas [25], such as the conservation laws and the H theorem [27].

It is known that the ratio of the bulk viscosity μ_b to the viscosity μ is quite large for CO_2 gas and is of the order of 1000 [28,29]. This large value of the ratio μ_b/μ causes a large shock thickness, which gives a computational difficulty, in particular, for type-C profiles, since a very large computational domain as well as a fine grid system inside the thin front layer is required. For this reason, in our previous paper [23], we considered an artificial CO_2 gas with a smaller values of the ratio μ_b/μ ($\leqslant 100$), which was called a pseudo-CO_2 gas. It was shown that the pseudo-CO_2 gases with increasing ratio μ_b/μ tended to reproduce the double-layer structure (type C) well.

The present study is a continuation and extension of Ref. [23]. First, we carry out an accurate numerical computation based on the same ES model for the pseudo-CO_2 gases with larger values of the ratio μ_b/μ up to the real CO_2 gas with μ_b/μ being of the order of 1000 and show that the solutions corresponding to type-A, B, and C profiles are obtained. Then, we derive a set of macroscopic equations that describes the thick rear layer in type-C profile (with the help of an appropriate jump condition corresponding to the thin front layer), as well as entire type-A and B profiles, by an asymptotic analysis for large μ_b/μ under a slowly varying assumption. It should be mentioned that the shock-structure problem for a polyatomic gas has been studied in a recent paper [30] using essentially the same macroscopic equations (with six macroscopic variables), which were obtained by different approaches, that is, by the extended thermodynamics [31] and by a moment closure based on kinetic theory [31,32]. Mention should also be made of a recent paper [33] that has

investigated a shock structure for the CO_2 gas using the Navier-Stokes equations with accurate CO_2 physical properties.

The paper is organized as follows. After this introduction in Sec. I, the problem and assumptions are described in Sec. II, and the problem is formulated both in dimensional and dimensionless forms in Sec. III. Section IV is devoted to the description of the numerical method and the result of the numerical analysis. In Sec. V, the asymptotic analysis for large μ_b/μ is carried out to derive the set of macroscopic equations, and its solution is compared with the numerical solution. Section VI contains short concluding remarks. In addition, we summarize the basic properties of the ES model in Appendix A and provide some materials supplementary to the numerical analysis in Appendix B and to the asymptotic analysis in Appendix C.

II. PROBLEM AND ASSUMPTIONS

Let us consider a stationary plane shock wave standing in a flow of an ideal polyatomic gas. We take the X_1 axis of the coordinate system (X_1, X_2, X_3) perpendicular to the shock wave. The gas at upstream infinity $(X_1 \to -\infty)$ is in an equilibrium state with density ρ_-, flow velocity $\boldsymbol{v}_- = (v_-, 0, 0)$, and temperature T_-, and that at downstream infinity $(X_1 \to \infty)$ is in another equilibrium state with density ρ_+, flow velocity $\boldsymbol{v}_+ = (v_+, 0, 0)$, and temperature T_+. We investigate the steady behavior of the gas under the following assumptions:

(i) The behavior of the gas is described by the ellipsoidal statistical (ES) model of the Boltzmann equation for a polyatomic gas [25,26].

(ii) The problem is spatially one dimensional, so that the physical quantities are independent of X_2 and X_3.

Let us denote by γ the ratio of the specific heats, that is, $\gamma = c_p/c_v$, where c_p and c_v are the specific heat at constant pressure and that at constant volume, respectively. In this paper, we assume that c_p, c_v, and thus γ are constant (*calorically perfect gas*; it is also called *polytropic gas* in the literature). Then, γ is expressed in terms of the internal degrees of freedom δ of a molecule as

$$\gamma = (\delta + 5)/(\delta + 3), \tag{1}$$

where δ can be any positive real number (not restricted to an integer). We denote by M_- the Mach number of the flow at upstream infinity, i.e., $M_- = v_-/\sqrt{\gamma R T_-}$, where R is the gas constant per unit mass ($R = k/m$ with the Boltzmann constant k and the mass of a molecule m). Then, the Rankine-Hugoniot relations give the following expressions of the downstream quantities ρ_+, v_+, and T_+ in terms of the upstream quantities ρ_-, v_-, and T_- and the upstream Mach number M_- (see Appendix A 2):

$$\rho_+ = \frac{(\gamma + 1)M_-^2}{(\gamma - 1)M_-^2 + 2} \rho_-, \tag{2a}$$

$$v_+ = \frac{(\gamma - 1)M_-^2 + 2}{(\gamma + 1)M_-^2} v_-, \tag{2b}$$

$$T_+ = \frac{[2\gamma M_-^2 - (\gamma - 1)][(\gamma - 1)M_-^2 + 2]}{(\gamma + 1)^2 M_-^2} T_-. \tag{2c}$$

Incidentally, the Mach number of the flow at downstream infinity M_+, i.e., $M_+ = v_+/\sqrt{\gamma R T_+}$, is given as

$$M_+ = \left[\frac{(\gamma - 1)M_-^2 + 2}{2\gamma M_-^2 - (\gamma - 1)} \right]^{1/2}. \tag{3}$$

III. FORMULATION OF THE PROBLEM

A. Basic equations

Let us consider a polyatomic gas with internal degrees of freedom δ. Let t be the time variable, X (or X_i) the position vector in the physical space, $\boldsymbol{\xi}$ (or ξ_i) the molecular velocity, and $\mathcal{E}$ the energy associated with the internal modes. We denote the number of the gas molecules contained in an infinitesimal volume $dX d\boldsymbol{\xi} d\mathcal{E}$ around a point $(X, \boldsymbol{\xi}, \mathcal{E})$ in the seven-dimensional space consisting of $X, \boldsymbol{\xi}$, and $\mathcal{E}$ at time t by

$$\frac{1}{m} f(t, X, \boldsymbol{\xi}, \mathcal{E}) dX d\boldsymbol{\xi} d\mathcal{E}. \tag{4}$$

We call $f(t, X, \boldsymbol{\xi}, \mathcal{E})$ the velocity-energy distribution function of the gas molecules. It is governed by the ES model of the Boltzmann equation for a polyatomic gas [25,26]. In the present time-independent and spatially one-dimensional case, where $f = f(X_1, \boldsymbol{\xi}, \mathcal{E})$, the equation is written in the following form:

$$\xi_1 \frac{\partial f}{\partial X_1} = Q(f), \tag{5}$$

where

$$Q(f) = A_c(T)\rho(\mathcal{G} - f), \tag{6a}$$

$$\mathcal{G} = \frac{\rho \mathcal{E}^{\delta/2-1}}{(2\pi)^{3/2}[\det(\mathsf{T})]^{1/2}(RT_{\text{rel}})^{\delta/2}\Gamma(\delta/2)} \exp\left(-\frac{1}{2}(\xi_i - v_i)(\mathsf{T}^{-1})_{ij}(\xi_j - v_j) - \frac{\mathcal{E}}{RT_{\text{rel}}}\right), \tag{6b}$$

$$(\mathsf{T})_{ij} = (1-\theta)[(1-\nu)RT_{\text{tr}}\delta_{ij} + \nu p_{ij}/\rho] + \theta RT\delta_{ij}, \tag{6c}$$

$$\rho = \iint_0^\infty f d\mathcal{E} d\boldsymbol{\xi}, \tag{6d}$$

$$v_i = \frac{1}{\rho} \iint_0^\infty \xi_i f d\mathcal{E} d\boldsymbol{\xi}, \tag{6e}$$

$$p_{ij} = \iint_0^\infty (\xi_i - v_i)(\xi_j - v_j) f d\mathcal{E} d\boldsymbol{\xi}, \tag{6f}$$

$$T_{\text{tr}} = \frac{1}{3\rho R} \iint_0^\infty |\boldsymbol{\xi} - \boldsymbol{v}|^2 f d\mathcal{E} d\boldsymbol{\xi}, \tag{6g}$$

$$T_{\text{int}} = \frac{2}{\delta \rho R} \iint_0^\infty \mathcal{E} f d\mathcal{E} d\boldsymbol{\xi}, \tag{6h}$$

$$T = \frac{3T_{\text{tr}} + \delta T_{\text{int}}}{3 + \delta}, \tag{6i}$$

$$T_{\text{rel}} = \theta T + (1-\theta)T_{\text{int}}. \tag{6j}$$

Here, ρ is the density, $\boldsymbol{v}$ (or v_i) $=(v_1, 0, 0)$ the flow velocity, p_{ij} the stress tensor, T_{tr} the temperature associated with translational motion, T_{int} the temperature associated with the energy of the internal modes, T the temperature, $d\boldsymbol{\xi} = d\xi_1 d\xi_2 d\xi_3$, and the domain of integration with respect to $\boldsymbol{\xi}$ is the whole space of $\boldsymbol{\xi}$. The symbol δ_{ij} indicates the Kronecker delta, and $\nu \in [-1/2, 1)$ and $\theta \in (0, 1]$ are the constants that adjust the Prandtl number and the bulk viscosity. In addition, $A_c(T)$ is a function of T such that $A_c(T)\rho$ is the collision frequency of the gas molecules, $\Gamma(z)$ is the gamma function defined by

$$\Gamma(z) = \int_0^\infty s^{z-1} e^{-s} ds, \tag{7}$$

T is the 3×3 positive-definite symmetric matrix whose (i, j) component is defined by Eq. (6c), and $\det(\mathsf{T})$ and T^{-1} are, respectively, its determinant and inverse. Here and in what follows, we basically use the summation convention, i.e., $a_i b_i = \sum_{i=1}^{3} a_i b_i, a_i c_{ij} b_j = \sum_{i,j=1}^{3} a_i c_{ij} b_j$, etc. The pressure p and the heat-flow vector q_i are given by

$$p = R\rho T, \tag{8}$$

$$q_i = \iint_0^\infty (\xi_i - v_i)\left(\frac{1}{2}|\boldsymbol{\xi} - \boldsymbol{v}|^2 + \mathcal{E}\right) f d\mathcal{E} d\boldsymbol{\xi}, \tag{9}$$

where Eq. (8) is the equation of state. It should be noted that in Ref. [25], the variable I, which is related to our $\mathcal{E}$ as $\mathcal{E} = I^{2/\delta}$, is used as an independent variable instead of $\mathcal{E}$. See Appendix A in Ref. [34] for the relation between the notation in Ref. [25] and that of the present paper.

The vanishing of the collision term $Q(f) = 0$ is equivalent to the fact that f is the following local equilibrium distribution:

$$f_{\text{eq}} = \frac{\rho \mathcal{E}^{\delta/2-1}}{(2\pi RT)^{3/2}(RT)^{\delta/2}\Gamma(\delta/2)} \exp\left(-\frac{|\boldsymbol{\xi} - \boldsymbol{v}|^2}{2RT} - \frac{\mathcal{E}}{RT}\right). \tag{10}$$

In addition, for an arbitrary function $g(t, \boldsymbol{X}, \boldsymbol{\xi}, \mathcal{E})$, the following relation holds (see Appendix A):

$$\iint_0^\infty \varphi_r Q(g) d\mathcal{E} d\boldsymbol{\xi} = 0, \tag{11}$$

where φ_r $(r = 0, ..., 4)$ are the collision invariants, i.e.,

$$\varphi_0 = 1, \quad \varphi_i = \xi_i \quad (i = 1, 2, 3), \quad \varphi_4 = \tfrac{1}{2}|\boldsymbol{\xi}|^2 + \mathcal{E}. \tag{12}$$

It should also be mentioned that for Eq. (5), the viscosity μ, the thermal conductivity κ, the Prandtl number Pr, and the bulk viscosity μ_b are obtained as

$$\mu = \frac{1}{1 - \nu + \theta\nu}\frac{RT}{A_c(T)}, \quad \kappa = \frac{\gamma R}{\gamma - 1}\frac{RT}{A_c(T)}, \quad \text{Pr} = \frac{1}{1 - \nu + \theta\nu}, \quad \mu_b = \frac{1}{\theta}\left(\frac{5}{3} - \gamma\right)\frac{\mu}{\text{Pr}}. \tag{13}$$

The boundary condition at upstream infinity and that at downstream infinity are given as follows:

$$f = \frac{\rho_- \mathcal{E}^{\delta/2-1}}{(2\pi RT_-)^{3/2}(RT_-)^{\delta/2}\Gamma(\delta/2)} \exp\left(-\frac{(\xi_1 - v_-)^2 + \xi_2^2 + \xi_3^2}{2RT_-} - \frac{\mathcal{E}}{RT_-}\right), \quad (X_1 \to -\infty), \tag{14a}$$

$$f = \frac{\rho_+ \mathcal{E}^{\delta/2-1}}{(2\pi RT_+)^{3/2}(RT_+)^{\delta/2}\Gamma(\delta/2)} \exp\left(-\frac{(\xi_1 - v_+)^2 + \xi_2^2 + \xi_3^2}{2RT_+} - \frac{\mathcal{E}}{RT_+}\right), \quad (X_1 \to \infty). \tag{14b}$$

We investigate the shock-wave structure on the basis of the system, Eqs. (5), (6), and (14), with special interest in the case of large μ_b/μ. When $\mu_b/\mu = \infty$ (i.e., $\theta = 0$), the Rankine–Hugoniot relations take a different form, which is derived in Appendix A 3 [Eq. (A20)]. This plays an important role in the present study.

B. Dimensionless system

In this subsection we introduce dimensionless variables and present our basic system in dimensionless form. Let us introduce the dimensionless quantities $[x_i, \zeta_i, \hat{\mathcal{E}}, \hat{f}, \hat{\mathcal{G}}, \hat{A}_c(\hat{T}), \hat{\rho}, \hat{v}_i, \hat{p}_{ij}, \hat{T}_{\text{tr}}, \hat{T}_{\text{int}}, \hat{T}, \hat{T}_{\text{rel}}, \hat{p}, \hat{q}_i]$, which correspond to the original dimensional quantities $[X_i, \xi_i, \mathcal{E}, f, \mathcal{G}, A_c(T), \rho, v_i, p_{ij}, T_{\text{tr}}, T_{\text{int}}, T, T_{\text{rel}}, p, q_i]$, by the following relations:

$$x_i = X_i/l_-, \quad \zeta_i = \xi_i/(2RT_-)^{1/2}, \quad \hat{\mathcal{E}} = \mathcal{E}/RT_-, \quad (\hat{f}, \hat{\mathcal{G}}) = (f, \mathcal{G})/2\rho_-(2RT_-)^{-5/2},$$

$$\hat{A}_c(\hat{T}) = A_c(T)/A_c(T_-), \quad \hat{\rho} = \rho/\rho_-, \quad \hat{v}_i = v_i/(2RT_-)^{1/2}, \quad \hat{p}_{ij} = p_{ij}/p_-,$$

$$(\hat{T}_{\text{tr}}, \hat{T}_{\text{int}}, \hat{T}, \hat{T}_{\text{rel}}) = (T_{\text{tr}}, T_{\text{int}}, T, T_{\text{rel}})/T_-, \quad \hat{p} = p/p_-, \quad \hat{q}_i = q_i/p_-(2RT_-)^{1/2}, \tag{15}$$

where $p_- = R\rho_- T_-$, and $l_- = (2/\sqrt{\pi})(2RT_-)^{1/2}/A_c(T_-)\rho_-$ is the mean free path of the gas molecules in the equilibrium state at rest with density ρ_- and temperature T_-. We occasionally use the bold-faced letters x, ζ, $\hat{v}$, and $\hat{q}$ for x_i, ζ_i, $\hat{v}_i$, and $\hat{q}_i$, respectively.

Using these dimensionless quantities, we obtain the following dimensionless form of the ES model (5):

$$\zeta_1 \frac{\partial \hat{f}}{\partial x_1} = \frac{2}{\sqrt{\pi}} \hat{Q}(\hat{f}), \tag{16}$$

where

$$\hat{Q}(\hat{f}) = \hat{A}_c(\hat{T})\hat{\rho}(\hat{\mathcal{G}} - \hat{f}), \tag{17a}$$

$$\hat{\mathcal{G}} = \frac{\hat{\rho}}{\pi^{3/2}[\det(\hat{\mathsf{T}})]^{1/2} \hat{T}_{\mathrm{rel}}^{\delta/2} \Gamma(\delta/2)} \hat{\mathcal{E}}^{\delta/2-1} \exp\left(-(\zeta_i - \hat{v}_i)(\hat{\mathsf{T}}^{-1})_{ij}(\zeta_j - \hat{v}_j) - \frac{\hat{\mathcal{E}}}{\hat{T}_{\mathrm{rel}}}\right), \tag{17b}$$

$$(\hat{\mathsf{T}})_{ij} = (1 - \theta)[(1 - \nu)\hat{T}_{\mathrm{tr}}\delta_{ij} + \nu \hat{p}_{ij}/\hat{\rho}] + \theta \hat{T} \delta_{ij}, \tag{17c}$$

$$\hat{\rho} = \iint_0^\infty \hat{f} d\hat{\mathcal{E}} d\zeta, \tag{17d}$$

$$\hat{v}_i = \frac{1}{\hat{\rho}} \iint_0^\infty \zeta_i \hat{f} d\hat{\mathcal{E}} d\zeta, \tag{17e}$$

$$\hat{p}_{ij} = 2 \iint_0^\infty (\zeta_i - \hat{v}_i)(\zeta_j - \hat{v}_j) \hat{f} d\hat{\mathcal{E}} d\zeta, \tag{17f}$$

$$\hat{T}_{\mathrm{tr}} = \frac{2}{3\hat{\rho}} \iint_0^\infty |\zeta - \hat{v}|^2 \hat{f} d\hat{\mathcal{E}} d\zeta, \tag{17g}$$

$$\hat{T}_{\mathrm{int}} = \frac{2}{\delta\hat{\rho}} \iint_0^\infty \hat{\mathcal{E}} \hat{f} d\hat{\mathcal{E}} d\zeta, \tag{17h}$$

$$\hat{T} = \frac{3\hat{T}_{\mathrm{tr}} + \delta\hat{T}_{\mathrm{int}}}{3 + \delta}, \tag{17i}$$

$$\hat{T}_{\mathrm{rel}} = \theta \hat{T} + (1 - \theta)\hat{T}_{\mathrm{int}}. \tag{17j}$$

Here, $d\zeta = d\zeta_1 d\zeta_2 d\zeta_3$, and the domain of integration with respect to ζ is the whole space of ζ. The (dimensionless) pressure $\hat{p}$ and heat-flow vector $\hat{q}_i$ are given by

$$\hat{p} = \hat{\rho}\hat{T}, \tag{18}$$

$$\hat{q}_i = \iint_0^\infty (\zeta_i - \hat{v}_i)(|\zeta - \hat{v}|^2 + \hat{\mathcal{E}}) \hat{f} d\hat{\mathcal{E}} d\zeta. \tag{19}$$

Corresponding to the statement including Eq. (10), $\hat{Q}(\hat{f}) = 0$ is equivalent to the fact that $\hat{f}$ is the dimensionless local equilibrium distribution given by

$$\hat{f}_{\mathrm{eq}} = \frac{\hat{\rho}\hat{\mathcal{E}}^{\delta/2-1}}{(\pi\hat{T})^{3/2}\hat{T}^{\delta/2}\Gamma(\delta/2)} \exp\left(-\frac{|\zeta - \hat{v}|^2}{\hat{T}} - \frac{\hat{\mathcal{E}}}{\hat{T}}\right). \tag{20}$$

In addition, the dimensionless version of the statement containing Eqs. (11) and (12) reads as follows: For an arbitrary function $\hat{g}(\hat{t}, x, \zeta, \hat{\mathcal{E}})$, the relation

$$\iint_0^\infty \hat{\varphi}_r \hat{Q}(\hat{g}) d\hat{\mathcal{E}} d\zeta = 0 \tag{21}$$

holds, where $\hat{\varphi}_r$ ($r = 0, ..., 4$) are the dimensionless collision invariants, i.e.,

$$\hat{\varphi}_0 = 1, \quad \hat{\varphi}_i = \zeta_i \quad (i = 1, 2, 3), \quad \hat{\varphi}_4 = |\boldsymbol{\zeta}|^2 + \hat{\mathcal{E}}. \tag{22}$$

The boundary conditions (14) are nondimensionalized as follows:

$$\hat{f} = \frac{\hat{\mathcal{E}}^{\delta/2-1}}{\pi^{3/2}\Gamma(\delta/2)} \exp\left(-[(\zeta_1 - \hat{v}_-)^2 + \zeta_2^2 + \zeta_3^2] - \hat{\mathcal{E}}\right), \quad (x_1 \to -\infty), \tag{23a}$$

$$\hat{f} = \frac{\hat{\rho}_+ \hat{\mathcal{E}}^{\delta/2-1}}{(\pi \hat{T}_+)^{3/2} \hat{T}_+^{\delta/2} \Gamma(\delta/2)} \exp\left(-\frac{(\zeta_1 - \hat{v}_+)^2 + \zeta_2^2 + \zeta_3^2}{\hat{T}_+} - \frac{\hat{\mathcal{E}}}{\hat{T}_+}\right), \quad (x_1 \to \infty), \tag{23b}$$

where

$$\hat{v}_- = \frac{v_-}{(2RT_-)^{1/2}} = \sqrt{\frac{\gamma}{2}} M_-, \quad \hat{v}_+ = \frac{v_+}{(2RT_-)^{1/2}} = \sqrt{\frac{\gamma}{2}} \frac{(\gamma-1)M_-^2 + 2}{(\gamma+1)M_-}, \tag{24a}$$

$$\hat{\rho}_+ = \frac{\rho_+}{\rho_-} = \frac{(\gamma+1)M_-^2}{(\gamma-1)M_-^2 + 2}, \quad \hat{T}_+ = \frac{T_+}{T_-} = \frac{[2\gamma M_-^2 - (\gamma-1)][(\gamma-1)M_-^2 + 2]}{(\gamma+1)^2 M_-^2}. \tag{24b}$$

We will investigate Eqs. (16) and (23) numerically in Sec. IV and analytically in Sec. V. To analyze the system, we first specify the internal degrees of freedom δ or the ratio of the specific heats γ [cf. Eq. (1)] for the gas under consideration, and then determine the functional form of $A_c(T)$ and the values of ν and θ on the basis of the transport coefficients (13).

From the conservation laws (see Appendix A 2), the following relations hold for any x_1:

$$\hat{\rho}\hat{v}_1 = \hat{v}_-, \quad \hat{p}_{11} + 2\hat{\rho}\hat{v}_1^2 = 1 + 2\hat{v}_-^2, \quad \hat{p}_{12} = \hat{p}_{13} = 0, \tag{25a}$$

$$\hat{q}_1 + \hat{p}_{11}\hat{v}_1 + \hat{v}_1\left(\frac{3+\delta}{2}\hat{p} + \hat{\rho}\hat{v}_1^2\right) = \hat{v}_-\left(\frac{5+\delta}{2} + \hat{v}_-^2\right). \tag{25b}$$

These relations can be used for the accuracy tests in the numerical analysis.

When $\mu_b/\mu = \infty$, the Rankine-Hugoniot relation is given by Eq. (A20), which is different from Eq. (2). For later convenience, we introduce the dimensionless density $\hat{\rho}_{**}$, flow velocity $\hat{v}_{**}$, and translational temperature $\hat{T}_{**}$ at the downstream condition of the Rankine-Hugoniot relations for $\mu_b/\mu = \infty$. That is, because $T_{\text{tr}-} = T_{\text{int}-} = T_-$ holds in the present problem, Eq. (A20) gives the following expression of them:

$$\hat{\rho}_{**} = \frac{\rho_+}{\rho_-} = \frac{4\widetilde{M}_-^2}{\widetilde{M}_-^2 + 3}, \quad \hat{v}_{**} = \frac{v_+}{\sqrt{2RT_-}} = \sqrt{\frac{5}{6}} \frac{\widetilde{M}_-^2 + 3}{4\widetilde{M}_-}, \tag{26a}$$

$$\hat{T}_{**} = \frac{T_{\text{tr}+}}{T_-} = \frac{(5\widetilde{M}_-^2 - 1)(\widetilde{M}_-^2 + 3)}{16\widetilde{M}_-^2}, \tag{26b}$$

where

$$\widetilde{M}_- = \frac{v_-}{\sqrt{5RT_-/3}}. \tag{27}$$

IV. NUMERICAL ANALYSIS

A. Preliminaries

Since we are considering the case where $\hat{v}_2 = \hat{v}_3 = 0$, we can assume that the velocity-energy distribution function $\hat{f}$ is cylindrically symmetric with respect to ζ_1 in the $\boldsymbol{\zeta}$ space, that is,

$$\hat{f} = \hat{f}(x_1, \zeta_1, \zeta_\rho, \hat{\mathcal{E}}), \quad \zeta_\rho = \left(\zeta_2^2 + \zeta_3^2\right)^{1/2}. \tag{28}$$

This form makes some components of $\hat{p}_{ij}$, $\hat{q}_i$, and thus $(\hat{\mathsf{T}})_{ij}$ trivial in addition to $\hat{v}_2 = \hat{v}_3 = 0$, i.e.,

$$\hat{p}_{12} = \hat{p}_{13} = \hat{p}_{23} = 0, \quad \hat{q}_2 = \hat{q}_3 = 0, \quad (\hat{\mathsf{T}})_{12} = (\hat{\mathsf{T}})_{13} = (\hat{\mathsf{T}})_{23} = 0. \tag{29}$$

Then, we introduce the following marginal velocity distribution functions:

$$\phi_1(x_1, \zeta_1) = 2\pi \int_0^\infty \int_0^\infty \zeta_\rho \hat{f}(x_1, \zeta_1, \zeta_\rho, \hat{\mathcal{E}}) d\hat{\mathcal{E}} d\zeta_\rho, \tag{30a}$$

$$\phi_2(x_1, \zeta_1) = 2\pi \int_0^\infty \int_0^\infty \zeta_\rho^3 \hat{f}(x_1, \zeta_1, \zeta_\rho, \hat{\mathcal{E}}) d\hat{\mathcal{E}} d\zeta_\rho, \tag{30b}$$

$$\phi_3(x_1, \zeta_1) = 2\pi \int_0^\infty \int_0^\infty \zeta_\rho \hat{\mathcal{E}} \hat{f}(x_1, \zeta_1, \zeta_\rho, \hat{\mathcal{E}}) d\hat{\mathcal{E}} d\zeta_\rho. \tag{30c}$$

If we multiply Eq. (16) with Eq. (28) by $2\pi(\zeta_\rho, \zeta_\rho^3, \zeta_\rho \hat{\mathcal{E}})$, integrate the resulting equations from 0 to ∞ with respect to ζ_ρ and $\hat{\mathcal{E}}$, and rewrite the macroscopic quantities in Eq. (17) in terms of ϕ_1, ϕ_2, and ϕ_3, then we obtain the following system of equations for ϕ_1, ϕ_2, and ϕ_3:

$$\zeta_1 \frac{\partial \phi_k}{\partial x_1} = \frac{2}{\sqrt{\pi}} \hat{A}_c(\hat{T}) \hat{\rho} (\Psi_k - \phi_k), \quad (k = 1, 2, 3), \tag{31}$$

where

$$\begin{bmatrix} \Psi_1 \\ \Psi_2 \\ \Psi_3 \end{bmatrix} = \frac{\hat{\rho}}{\sqrt{\pi} \, (\hat{\mathsf{T}})_{11}^{1/2}} \begin{bmatrix} 1 \\ (\hat{\mathsf{T}})_{22} \\ (\delta/2)\hat{T}_{\text{rel}} \end{bmatrix} \exp\left(-\frac{(\zeta_1 - \hat{v}_1)^2}{(\hat{\mathsf{T}})_{11}}\right), \tag{32a}$$

$$(\hat{\mathsf{T}})_{11} = (1 - \theta)[(1 - \nu)\hat{T}_{\text{tr}} + \nu \hat{p}_{11}/\hat{\rho}] + \theta \hat{T}, \tag{32b}$$

$$(\hat{\mathsf{T}})_{22}[=(\hat{\mathsf{T}})_{33}] = (1 - \theta)[(1 - \nu)\hat{T}_{\text{tr}} + \nu \hat{p}_{22}/\hat{\rho}] + \theta \hat{T}, \tag{32c}$$

$$\hat{\rho} = \int_{-\infty}^\infty \phi_1 d\zeta_1, \quad \hat{v}_1 = \frac{1}{\hat{\rho}} \int_{-\infty}^\infty \zeta_1 \phi_1 d\zeta_1, \tag{32d}$$

$$\hat{p}_{11} = 2 \int_{-\infty}^\infty (\zeta_1 - \hat{v}_1)^2 \phi_1 d\zeta_1, \quad \hat{p}_{22}[=\hat{p}_{33}] = \int_{-\infty}^\infty \phi_2 d\zeta_1, \tag{32e}$$

$$\hat{T}_{\text{tr}} = \frac{2}{3\hat{\rho}} \int_{-\infty}^\infty [(\zeta_1 - \hat{v}_1)^2 \phi_1 + \phi_2] d\zeta_1, \quad \hat{T}_{\text{int}} = \frac{2}{\delta \hat{\rho}} \int_{-\infty}^\infty \phi_3 d\zeta_1, \tag{32f}$$

$$\hat{T} = \frac{3\hat{T}_{\text{tr}} + \delta \hat{T}_{\text{int}}}{3 + \delta}, \quad \hat{T}_{\text{rel}} = \theta \hat{T} + (1 - \theta)\hat{T}_{\text{int}}. \tag{32g}$$

The boundary conditions for Eq. (31) can be obtained from Eq. (23) by the same procedure. The result is as follows:

$$\begin{bmatrix} \phi_1 \\ \phi_2 \\ \phi_3 \end{bmatrix} = \frac{1}{\pi^{1/2}} \begin{bmatrix} 1 \\ 1 \\ \delta/2 \end{bmatrix} \exp(-(\zeta_1 - \hat{v}_-)^2), \quad (x_1 \to -\infty), \tag{33a}$$

$$\begin{bmatrix} \phi_1 \\ \phi_2 \\ \phi_3 \end{bmatrix} = \frac{\hat{\rho}_+}{(\pi \hat{T}_+)^{1/2}} \begin{bmatrix} 1 \\ \hat{T}_+ \\ (\delta/2)\hat{T}_+ \end{bmatrix} \exp\left(-\frac{(\zeta_1 - \hat{v}_+)^2}{\hat{T}_+}\right), \quad (x_1 \to \infty). \tag{33b}$$

We will analyze Eqs. (31), (32), and (33) numerically. It should be noted that the molecular velocity components ζ_2 and ζ_3 and the energy variable $\hat{\mathcal{E}}$ have been eliminated in Eqs. (31), (32), and (33), so that we need to handle only two independent variables x_1 and ζ_1.

Finally, we note that the (dimensionless) heat flow is expressed as

$$\hat{q}_1 = \int_{-\infty}^{\infty} (\zeta_1 - \hat{v}_1)[(\zeta_1 - \hat{v}_1)^2 \phi_1 + \phi_2 + \phi_3] d\zeta_1. \tag{34}$$

B. Grid system and finite-different scheme

We limit the range of x_1 to a finite range $-D_n \leqslant x_1 \leqslant D_p$ with sufficiently large positive constants D_n and D_p ($D_n < D_p$) and set the grid points $x_{(i)}$ ($i = -N_n, -N_n + 1, ..., 0, ..., N_p - 1, N_p; N_n < N_p$) in such a way that $x_{(-N_n)} = -D_n$, $x_{(0)} = 0$, and $x_{(N_p)} = D_p$. We also limit the range of the molecular velocity ζ_1 to a finite range $-Z_n \leqslant \zeta_1 \leqslant Z_p$ with large positive constants Z_n and Z_p and set the grid points $\zeta_{(j)}$ ($j = 0, 1, 2, ..., 2M - 1, 2M$) as $\zeta_{(0)} = -Z_n$ and $\zeta_{(2M)} = Z_p$. The grid systems used for the computation are summarized in Appendix B 1.

Then, we denote the values of ϕ_k and Ψ_k ($k = 1, 2, 3$) and those of the macroscopic quantities at the grid points at the nth step of iteration by

$$\phi_k^{[n,i,j]} = \phi_k(x_{(i)}, \zeta_{(j)}) \quad \text{at the } n\text{th iteration} \quad (k = 1, 2, 3), \tag{35a}$$

$$\Psi_k^{[n,i,j]} = \Psi_k(x_{(i)}, \zeta_{(j)}) \quad \text{at the } n\text{th iteration} \quad (k = 1, 2, 3), \tag{35b}$$

$$h^{[n,i]} = h(x_{(i)}) \quad \text{at the } n\text{th iteration}, \tag{35c}$$

where $h = \hat{\rho}, \hat{v}_1, \hat{p}_{11}, \hat{p}_{22}, \dots$.

We adopt the following finite-difference scheme for Eq. (31):

$$\zeta_{(j)} \nabla \phi_k^{[n+1,i,j]} = B^{[n,i]} \left(\Psi_k^{[n,i,j]} - \phi_k^{[n+1,i,j]} \right), \tag{36}$$

where

$$B^{[n,i]} = \frac{2}{\sqrt{\pi}} \hat{A}_c(\hat{T}^{[n,i]}) \hat{\rho}^{[n,i]}, \tag{37}$$

and $\nabla \phi_k^{[n,i,j]}$ indicates the second-order upwind difference for $\partial \phi_k / \partial x_1$ defined as follows:

(i) for $\zeta_{(j)} > 0$,

$$\nabla \phi_k^{[n,i,j]} = \begin{cases} \left(\phi_k^{[n,-N_n+1,j]} - \phi_k^{[n,-N_n,j]} \right)/d_{-N_n+1} & (i = -N_n + 1), \\ w_0(d_i, d_{i-1})\phi_k^{[n,i,j]} - w_1(d_i, d_{i-1})\phi_k^{[n,i-1,j]} \\ \quad + w_2(d_i, d_{i-1})\phi_k^{[n,i-2,j]} & (-N_n + 2 \leqslant i \leqslant N_p), \end{cases} \tag{38a}$$

(ii) for $\zeta_{(j)} < 0$,

$$\nabla \phi_k^{[n,i,j]} = \begin{cases} \left(-\phi_k^{[n,N_p-1,j]} + \phi_k^{[n,N_p,j]} \right)/d_{N_p} & (i = N_p - 1), \\ -w_0(d_{i+1}, d_{i+2})\phi_k^{[n,i,j]} + w_1(d_{i+1}, d_{i+2})\phi_k^{[n,i+1,j]} \\ \quad - w_2(d_{i+1}, d_{i+2})\phi_k^{[n,i+2,j]} & (-N_n \leqslant i \leqslant N_p - 2). \end{cases} \tag{38b}$$

Here,

$$d_i = x_{(i)} - x_{(i-1)}, \quad w_0(a,b) = \frac{2a+b}{a(a+b)}, \quad w_1(a,b) = \frac{a+b}{ab}, \quad w_2(a,b) = \frac{a}{b(a+b)}.$$

If we express $\nabla \phi_k^{[n,i,j]}$ as

$$\nabla \phi_k^{[n,i,j]} = \begin{cases} \alpha_{i,0}^+ \phi_k^{[n,i,j]} + \alpha_{i,1}^+ \phi_k^{[n,i-1,j]} + \alpha_{i,2}^+ \phi_k^{[n,i-2,j]}, & \text{for } \zeta_{(j)} > 0, \\ \alpha_{i,0}^- \phi_k^{[n,i,j]} + \alpha_{i,1}^- \phi_k^{[n,i+1,j]} + \alpha_{i,2}^- \phi_k^{[n,i+2,j]}, & \text{for } \zeta_{(j)} < 0, \end{cases} \tag{39}$$

then, the finite-difference scheme can be written as

$$(B^{[n,i]} + \zeta_{(j)}\alpha_{i,0}^{\pm})\phi_k^{[n+1,i,j]} = B^{[n,i]}\Psi_k^{[n,i,j]} - \zeta_{(j)}\left(\alpha_{i,1}^{\pm}\phi_k^{[n+1,i\mp1,j]} + \alpha_{i,2}^{\pm}\phi_k^{[n+1,i\mp2,j]}\right). \tag{40}$$

C. Process of numerical computation

If we assume that the initial state is a local equilibrium, $\hat{p}_{11} = \hat{p}_{22}$ and $\hat{T}_{tr} = \hat{T}_{int} = \hat{p}_{11}/\hat{\rho}$ hold. We first choose an appropriate initial density distribution $\hat{\rho}^{[0,i]}$. Then, we determine the initial distributions of $\hat{v}_1$, $\hat{p}_{11}$, $\hat{p}_{22}$, $\hat{T}_{tr}$, and $\hat{T}_{int}$ using the above relations and the conservation of mass and momentum, Eq. (25a), as follows:

$$\hat{v}_1^{[0,i]} = \hat{v}_-/\hat{\rho}^{[0,i]}, \quad \hat{p}_{11}^{[0,i]} = \hat{p}_{22}^{[0,i]} = 1 + 2\hat{v}_-\left(\hat{v}_- - \hat{v}_1^{[0,i]}\right), \quad \hat{T}_{tr}^{[0,i]} = \hat{T}_{int}^{[0,i]} = \hat{p}_{11}^{[0,i]}/\hat{\rho}^{[0,i]}. \tag{41}$$

Suppose that the macroscopic quantities $h^{[n,i]}$ ($h = \hat{\rho}$, $\hat{v}_1$, $\hat{p}_{11}$, $\hat{p}_{22}$, $\hat{T}_{tr}$, $\hat{T}_{int}$) are known at all the grid points $x_{(i)}$. Then, the physical quantities at the $(n+1)$th step are obtained by the following process:

(i) Obtain $B^{[n,i]}$ and $\Psi_k^{[n,i,j]}$ ($k = 1, 2, 3$) at each grid point $x_{(i)}$ and $\zeta_{(j)}$.

(ii) For each j for which $\zeta_{(j)} > 0$, obtain $\phi_k^{[n+1,-N_n,j]}$ ($k = 1, 2, 3$) using the boundary condition at upstream infinity and then $\phi_k^{[n+1,i,j]}$ using the finite-difference scheme successively for $i = -N_n + 1, -N_n + 2, \ldots, N_p$.

(iii) For each j for which $\zeta_{(j)} < 0$, obtain $\phi_k^{[n+1,N_p,j]}$ ($k = 1, 2, 3$) using the boundary condition at downstream infinity and then $\phi_k^{[n+1,i,j]}$ using the finite-difference scheme successively for $i = N_p - 1, N_p - 2, \ldots, -N_n$.

(iv) For j for which $\zeta_{(j)} = 0$, let $\phi_k^{[n+1,i,j]} = \Psi_k^{[n,i,j]}$ ($k = 1, 2, 3$).

(v) Obtain the macroscopic quantities $h^{[n+1,i]}$ at each grid point $x_{(i)}$ by integrating the obtained $\phi_k^{[n+1,i,j]}$ numerically (using the Simpson rule).

We repeat the above process until the solution converges.

D. Results of numerical analysis

1. Parameter setting

We first explain our parameter setting. In the following, we set the upstream temperature T_- as 293 K. If we consider upstream Mach numbers $M_- = 1.2$ to 5, then, the downstream temperature T_+ becomes 331 to 1699 K for $\delta = 2$ ($\gamma = 7/5$), 321 to 1313 K for $\delta = 4$ ($\gamma = 9/7$), and 315 to 1092 K for $\delta = 6$ ($\gamma = 11/9$). We consider this temperature range.

In the present paper, we concentrate on the CO_2 gas and present the result only for it though the computation has also been performed for the N_2 gas. According to the data about c_p and γ given in Refs. [35–38], γ is not constant but depends on the temperature. Therefore, if we are based on the relation (1), δ should depend on the temperature. From the data in Refs. [35–38] and Eq. (1), we find that $\delta \approx 4$ at 300 K, 5 at 400 K, 6 at 550 K, 7 at 700 K, and 8 at 1000 K. Since the ES model that we are using has a constant δ, the computation will be performed with a fixed value $\delta = 4$ that corresponds to the upstream temperature. We may also set the values of δ according to the downstream temperature. In order to see the effect of different setting of δ, we will also carry out some computations for other values of δ.

The data of the viscosity μ and the thermal conductivity κ of the CO_2 gas from Refs. [35–39] agree reasonably well, so that we take Ref. [35] as our reference. If we try to fit the data of μ and κ in Ref. [35] with the least squares method assuming the power-law dependence on the temperature, we have

$$\mu(T) = \mu(293\,\text{K}) \times (T/293\,\text{K})^{0.84}, \quad \kappa(T) = \kappa(293\,\text{K}) \times (T/293\,\text{K})^{1.2}. \tag{42}$$

However, since the ES model gives a common temperature dependence for μ and κ [cf. Eq. (13)], we cannot take into account the different power shown in Eq. (42). Therefore, we make an intermediate
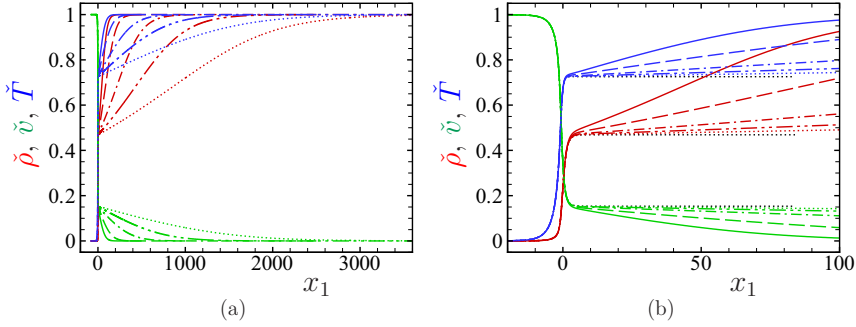
FIG. 2. Profiles of $\check{\rho}$, $\check{v}$, and $\check{T}$ at $M_- = 5$ for $\delta = 4$, Pr $= 0.761$, $A_c = $ const, and $\mu_b/\mu = 100, 200, 500,$ 1000, and 2000. (a) Profiles for $-200 \leqslant x_1 \leqslant 3600$; (b) profiles for $-20 \leqslant x_1 \leqslant 100$. The red curves indicate $\check{\rho}$, the green curves $\check{v}$, and the blue curves $\check{T}$. The solid lines indicate the profiles for $\mu_b/\mu = 100$, the dashed lines for $\mu_b/\mu = 200$, the dot-dashed lines for $\mu_b/\mu = 500$, the dot-dot-dashed lines for $\mu_b/\mu = 1000$, and the dotted lines for $\mu_b/\mu = 2000$. In panel (b), the black dotted lines indicate the profiles of $\check{\rho}$, $\check{v}$, and $\check{T}$ for $\mu_b/\mu = \infty$.

choice $\mu, \kappa \propto T$, i.e., $A_c(T) \propto T^0$, which is reasonably good for $T \lesssim 400$ K, except in the last part of Sec. IV D 2 where the comparison with Ref. [14] is made.

According to Ref. [35], the Prandtl number Pr decreases monotonically with the temperature: Pr $= 0.761$ (293 K), 0.745 (373 K), 0.735 (473 K), and 0.720 (973 K). Since Pr of the ES model is independent of the temperature, we basically fix Pr as Pr $= 0.761$. This looks reasonable because the variation of Pr with the temperature is not large. According to Refs. [28,29], the ratio of the bulk viscosity μ_b to the viscosity μ is large: $\mu_b/\mu \approx 10^3$ to 2×10^3 (Ref. [28], 293 K) and $\mu_b/\mu = 3922$ (Ref. [29], 296.3 K). According to Ref. [29], μ_b/μ decreases rapidly as the temperature increases. From Fig. 13 in Ref. [29], we obtain the following values: $\mu_b/\mu \approx 2400$ at 400 K, 1000 at 600 K, 600 at 800 K, 400 at 1000 K, and 200 at 1300 K. In the present computation, we vary μ_b/μ from 100 to 2000. It should be mentioned that the effect of the bulk viscosity on nonequilibrium CO_2 gas flows has been studied in Ref. [40].

In summary, we assume basically that $\delta = 4$ ($\gamma = 9/7$), $A_c(T) = $ const, Pr $= 0.761$, and $\mu_b/\mu = 100$ to 2000 (the computation is also carried out for $10 \leqslant \mu_b/\mu < 100$, but the result will not be shown in the present paper). The parameters ν and θ are chosen accordingly [cf. Eq. (13)]. In the present paper, we call the gas with these properties the *pseudo-CO_2 gas* and regard it as the real CO_2 gas when $\mu_b/\mu = 1000$ to 2000.

2. Numerical results

We show the results for pseudo-CO_2 gas with large μ_b/μ including the real CO_2 gas (i.e., pseudo-CO_2 gas with $\mu_b/\mu = 1000$ to 2000). In the following, we show the profiles of the density ρ, the flow velocity v_1 (the X_1 component), and the temperatures T, T_{tr}, and T_{int} normalized in the conventional way, that is,

$$\check{\rho} = \frac{\rho - \rho_-}{\rho_+ - \rho_-}, \quad \check{v} = \frac{v_1 - v_+}{v_- - v_+}, \quad \check{T} = \frac{T - T_-}{T_+ - T_-}, \quad \check{T}_{tr} = \frac{T_{tr} - T_-}{T_+ - T_-}, \quad \check{T}_{int} = \frac{T_{int} - T_-}{T_+ - T_-}. \quad (43)$$

We start with $M_- = 5$ and decrease M_- down to $M_- = 1.05$.

(i) Case of $M_- = 5$: Figure 2 shows the profiles of $\check{\rho}$, $\check{v}$, and $\check{T}$ at $M_- = 5$ for pseudo-CO_2 gases with $\mu_b/\mu = 100, 200, 500, 1000,$ and 2000. Figure 2(b) is a magnified figure of Fig. 2(a) in the range $-20 \leqslant x_1 (= X_1/l_-) \leqslant 100$. The red curves indicate $\check{\rho}$, the green curves $\check{v}$, and the blue curves $\check{T}$; the solid lines indicate $\mu_b/\mu = 100$, the dashed lines $\mu_b/\mu = 200$, the dot-dashed
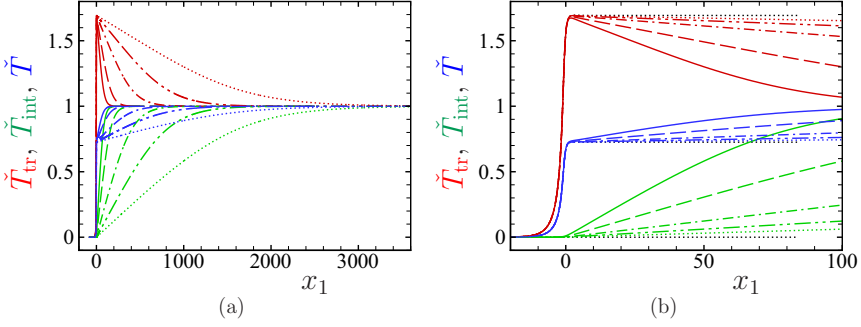
FIG. 3. Profiles of $\check{T}_{tr}$, $\check{T}_{int}$, and $\check{T}$ at $M_- = 5$ for $\delta = 4$, $\mathrm{Pr} = 0.761$, $A_c = \mathrm{const}$, and $\mu_b/\mu = 100, 200, 500$, 1000, and 2000. (a) Profiles for $-200 \leqslant x_1 \leqslant 3600$, (b) profiles for $-20 \leqslant x_1 \leqslant 100$. The red curves indicate $\check{T}_{tr}$, the green curves $\check{T}_{int}$, and the blue curves $\check{T}$. See the caption of Fig. 2 about the types of lines. In panel (b), the black dotted lines indicate the profiles of $\check{T}_{tr}$, $\check{T}_{int}$, and $\check{T}$ for $\mu_b/\mu = \infty$.

lines $\mu_b/\mu = 500$, the dot-dot-dashed lines $\mu_b/\mu = 1000$, and the dotted lines $\mu_b/\mu = 2000$. In Fig. 2(b), we also show by the black dotted lines the profiles of $\check{\rho}$, $\check{v}$, and $\check{T}$ when $\mu_b/\mu = \infty$. Note that in this case the downstream condition is different from that for finite μ_b/μ and is given by the Rankine-Hugoniot relations for $\mu_b/\mu = \infty$ [Eq. (A20) (note that $T_{tr-} = T_-$ in the present problem) or (26)]. In this figure and the following Figs. 3–6, $x_1 = 0$ is set at the position where the density is equal to the average of the upstream and downstream values when $\mu_b/\mu = \infty$, that is, $\hat{\rho} = (1 + \hat{\rho}_{**})/2$ [cf. Eq. (26a)]. The profiles are of type C, consisting of a thin front layer and a thick rear layer. As μ_b/μ increases, the thickness of the rear layer increases and reaches over 3000 mean free paths (l_-), whereas the profiles of the thin front layer are not affected by μ_b/μ and coincide with the shock profiles for $\mu_b/\mu = \infty$. This indicates that the thin front layer corresponds to the shock wave for $\mu_b/\mu = \infty$, and the jump caused by this layer is given by the Rankine-Hugoniot relations for $\mu_b/\mu = \infty$. For any large but finite value of μ_b/μ, $\check{\rho}$ and $\check{T}$ approach 1, and $\check{v}$ approaches 0 as $x_1 \to \infty$. However, for any fixed x_1, the values of $\check{\rho}$, $\check{v}$, and $\check{T}$ approach, as $\mu_b/\mu \to \infty$, the respective values corresponding to the downstream state of the shock wave for $\mu_b/\mu = \infty$.

Figure 3 shows the profiles of $\check{T}_{tr}$, $\check{T}_{int}$, and $\check{T}$ corresponding to Fig. 2. Here, the red curves indicate $\check{T}_{tr}$, the green curves $\check{T}_{int}$, and the blue curves $\check{T}$. As in Fig. 2(b), the black dotted lines indicate the profiles of $\check{T}_{tr}$, $\check{T}_{int}$, and $\check{T}$ for $\mu_b/\mu = \infty$. The thin front layer gives a significant overshoot of $\check{T}_{tr}$.
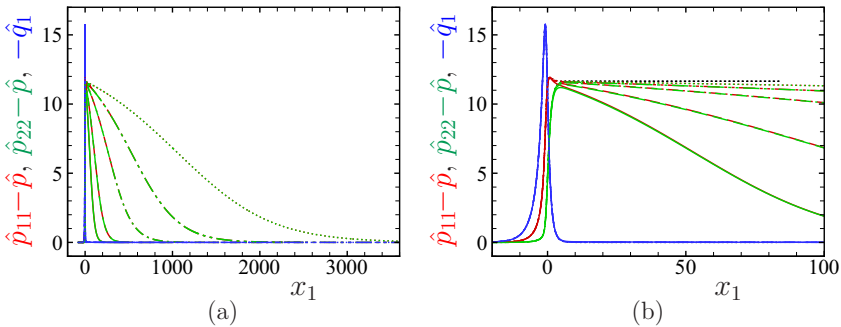

FIG. 4. Profiles of $\hat{p}_{11} - \hat{p}$, $\hat{p}_{22} - \hat{p}$, and $-\hat{q}_1$ at $M_- = 5$ for $\delta = 4$, $\mathrm{Pr} = 0.761$, $A_c = \mathrm{const}$, and $\mu_b/\mu = 100, 200, 500, 1000$, and 2000. (a) Profiles for $-200 \leqslant x_1 \leqslant 3600$; (b) profiles for $-20 \leqslant x_1 \leqslant 100$. The red curves indicate $\hat{p}_{11} - \hat{p}$, the green curves $\hat{p}_{22} - \hat{p}$, and the blue curves $-\hat{q}_1$. See the caption of Fig. 2 about the types of lines. In panel (b), the black dotted lines indicate the profiles of $\hat{p}_{11} - \hat{p}$, $\hat{p}_{22} - \hat{p}$, and $-\hat{q}_1$ for $\mu_b/\mu = \infty$.
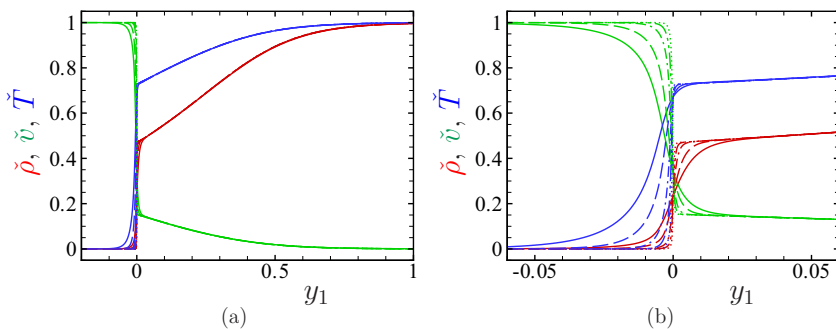
FIG. 5. Profiles of $\check{\rho}$, $\check{v}$, and $\check{T}$ at $M_- = 5$ for $\delta = 4$, Pr $= 0.761$, $A_c = $ const, and $\mu_b/\mu = 100, 200, 500,$ 1000, and 2000 in the new coordinate y_1. (a) Profiles for $-0.2 \leqslant y_1 \leqslant 1$; (b) profiles for $-0.06 \leqslant y_1 \leqslant 0.06$. The red curves indicate $\check{\rho}$, the green curves $\check{v}$ and the blue curves $\check{T}$. See the caption of Fig. 2 about the types of lines.

Figure 4 shows the profiles of $\hat{p}_{11} - \hat{p}$, $\hat{p}_{22} - \hat{p}$, and $-\hat{q}_1$. The $\hat{q}_1$ is nonzero only in the thin front layer and is not affected by μ_b/μ, and $\hat{p}_{11} = \hat{p}_{22}$ holds almost whole range of the thick rear layer.

Here, we introduce the new space coordinate y_1 whose length scale of variation is l_-/θ, i.e.,

$$y_1 = (2/\sqrt{\pi})\theta x_1 = (2/\sqrt{\pi})\theta(X_1/l_-), \tag{44}$$

which is expected to describe the slow variation occurring in the thick rear layer when $\mu_b/\mu \gg 1$ ($\theta \ll 1$). In Fig. 5, we show the profiles of $\check{\rho}$, $\check{v}$, and $\check{T}$, corresponding to Fig. 2, as the functions of y_1. Figure 5(b) is a magnified figure of Fig. 5(a). As one can see, the curves for $\mu_b/\mu = 100, 200,$ 500, 1000, and 2000 coincide perfectly in the thick rear layer. Using this new coordinate y_1, we will derive a set of macroscopic equations that can describe the slow relaxation over the thick rear layer in Sec. V.

Figure 6 shows the effect of the internal degrees of freedom δ in the case of $M_- = 5$ and $\mu_b/\mu = 1000$. The figure corresponds to Fig. 2, and the red, green, and blue curves indicate $\check{\rho}$, $\check{v}$, and $\check{T}$, respectively. In the figure, the solid lines indicate $\delta = 3$, the dashed lines $\delta = 4$, the dot-dashed lines $\delta = 5$, and the dot-dot-dashed lines $\delta = 8$. The difference in δ changes the profile of $\check{\rho}$ significantly.
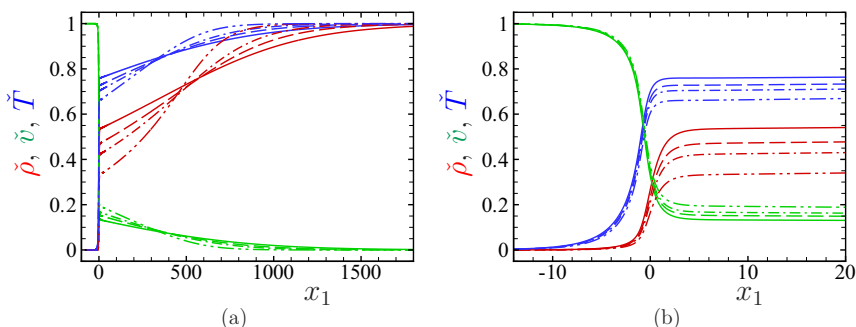

FIG. 6. Profiles of $\check{\rho}$, $\check{v}$, and $\check{T}$ at $M_- = 5$ for Pr $= 0.761$, $A_c = $ const, $\mu_b/\mu = 1000$, and $\delta = 3, 4, 5,$ and 8. (a) Profiles for $-100 \leqslant x_1 \leqslant 1800$; (b) profiles for $-14 \leqslant x_1 \leqslant 20$. The red curves indicate $\check{\rho}$, the green curves $\check{v}$, and the blue curves $\check{T}$. The solid lines indicate the profiles for $\delta = 3$, the dashed lines for $\delta = 4$, the dot-dashed lines for $\delta = 5$, and the dot-dot-dashed lines for $\delta = 8$.
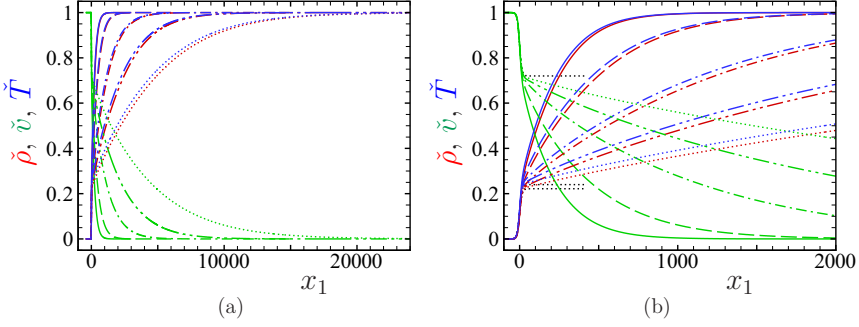
FIG. 7. Profiles of $\check{\rho}$, $\check{v}$, and $\check{T}$ at $M_- = 1.2$ for $\delta = 4$, $\mathrm{Pr} = 0.761$, $A_c = \text{const}$, and $\mu_b/\mu = 100, 200, 500,$ 1000, and 2000. (a) Profiles for $-1000 \leqslant x_1 \leqslant 24\,000$; (b) profiles for $-100 \leqslant x_1 \leqslant 2000$. The red curves indicate $\check{\rho}$, the green curves $\check{v}$, and the blue curves $\check{T}$. The solid lines indicate the profiles for $\mu_b/\mu = 100$, the dashed lines for $\mu_b/\mu = 200$, the dot-dashed lines for $\mu_b/\mu = 500$, the dot-dot-dashed lines for $\mu_b/\mu = 1000$, and the dotted lines for $\mu_b/\mu = 2000$. In panel (b), the black dotted lines indicate the profiles of $\check{\rho}$, $\check{v}$, and $\check{T}$ for $\mu_b/\mu = \infty$.

(ii) Case of $M_- = 1.2$: In Figs. 7–11, we show the profiles for a smaller upstream Mach number $M_- = 1.2$. Figures 7–11 correspond to Figs. 2–6, respectively. In these figures, $x_1 = 0$ is set in the same way as Figs. 2–6. The profile of the density is close to that of the temperature, and the values of $\hat{p}_{11} - \hat{p}$, $\hat{p}_{22} - \hat{p}$, and $-\hat{q}_1$ are small. These profiles are also of type C. However, the jumps due to the thin front layer is smaller compared with the case of $M_- = 5$. For $\mu_b/\mu = 2000$, the thick rear layer extends over $20\,000$ mean free paths.

(iii) Case of $M_- = 1.138\ldots$: This case corresponds to $\widetilde{M}_- = 1$, where $\widetilde{M}_- = v_-/\sqrt{5RT_-/3}$ is a parameter playing the role of the upstream Mach number in the Rankine-Hugoniot relations for $\mu_b/\mu = \infty$ [Eq. (A20) with $T_{\mathrm{tr}-} = T_-$ or (26)]. Figure 12 shows the profiles of $\check{\rho}$, $\check{v}$, and $\check{T}$, and Fig. 13 those of $\check{T}_{\mathrm{tr}}$ and $\check{T}_{\mathrm{int}}$. Figures 12(b) and 13(b) are, respectively, the magnified figures of Figs. 12(a) and 13(a). In the figures, $x_1 = 0$ is set at the position where $\check{\rho} = 0.05$ (i.e., $\hat{\rho} = 0.95 + 0.05\hat{\rho}_+$). The profiles do not show the double layer structure, but the thickness of the shock increases as μ_b/μ becomes large, as in the case of $M_- = 5$ and 1.2. Except $\check{T}_{\mathrm{int}}$, the profiles start abruptly from the upstream uniform state, though the approach of the profiles to the downstream uniform state is slow and smooth. Therefore, the profiles except for $\check{T}_{\mathrm{int}}$ are not symmetric with respect to the centers of the respective profiles, and we can say that the profiles in this case are of type B. As we will
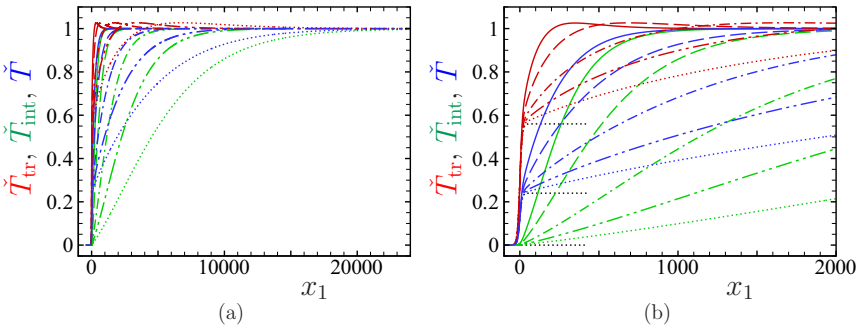

FIG. 8. Profiles of $\check{T}_{\mathrm{tr}}$, $\check{T}_{\mathrm{int}}$, and $\check{T}$ at $M_- = 1.2$ for $\delta = 4$, $\mathrm{Pr} = 0.761$, $A_c = \text{const}$, and $\mu_b/\mu = 100, 200, 500, 1000,$ and 2000. (a) Profiles for $-1000 \leqslant x_1 \leqslant 24\,000$, (b) profiles for $-100 \leqslant x_1 \leqslant 2000$. The red curves indicate $\check{T}_{\mathrm{tr}}$, the green curves $\check{T}_{\mathrm{int}}$, and the blue curves $\check{T}$. See the caption of Fig. 7 about the types of lines. In panel (b), the black dotted lines indicate the profiles of $\check{T}_{\mathrm{tr}}$, $\check{T}_{\mathrm{int}}$, and $\check{T}$ for $\mu_b/\mu = \infty$.
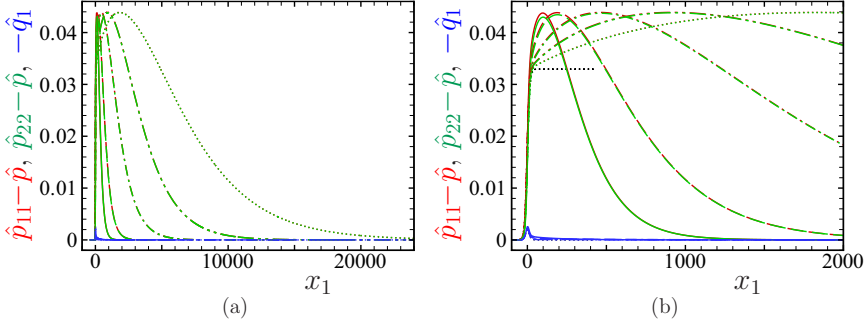
FIG. 9. Profiles of $\hat{p}_{11} - \hat{p}$, $\hat{p}_{22} - \hat{p}$, and $-\hat{q}_1$ at $M_- = 1.2$ for $\delta = 4$, $\mathrm{Pr} = 0.761$, $A_c = \mathrm{const}$, and $\mu_b/\mu = 100, 200, 500, 1000$, and 2000. (a) Profiles for $-1000 \leqslant x_1 \leqslant 24\,000$; (b) profiles for $-100 \leqslant x_1 \leqslant 2000$. The red curves indicate $\hat{p}_{11} - \hat{p}$, the green curves $\hat{p}_{22} - \hat{p}$, and the blue curves $-\hat{q}_1$. See the caption of Fig. 7 about the types of lines. In panel (b), the black dotted lines indicate the profiles of $\hat{p}_{11} - \hat{p}$, $\hat{p}_{22} - \hat{p}$, and $-\hat{q}_1$ for $\mu_b/\mu = \infty$.

see in Sec. V A, the leading-order asymptotic solution for large μ_b/μ (the slowly varying solution) gives the profiles that start suddenly from the upstream uniform state and thus exhibit a corner when $\widetilde{M}_- = 1$. This is the reason why we chose the case $\widetilde{M}_- = 1$ as a typical type-B profile.

(iv) Case of $M_- = 1.05$: Finally, we show the profiles of $\check{\rho}$, $\check{v}$, and $\check{T}$ for $M_- = 1.05$ in Fig. 14. Figure 14(b) is a magnified figure of Fig. 14(a). In the figure, $x_1 = 0$ is set at the position where $\check{\rho} = 1/2$ [i.e., $\hat{\rho} = (1 + \hat{\rho}_+)/2$]. The profiles, which are almost symmetric with respect to the centers of respective profiles, correspond to type-A profile. The thickness of the shock increases with the increase of μ_b/μ and reaches over 50 000 mean free paths for $\mu_b/\mu = 2000$.

In this way, the transition of the profiles from type A to type C at Mach numbers rather close to 1, which was predicted by the extended thermodynamics [14], is also observed in the present computation based on the ES model. The data for the numerical analysis, such as the numbers of the grid points and the accuracy tests, are given in Appendixes B 2 and B 3.

In the rest of this subsection, we compare our result with that of Ref. [14]. Here, we reset the parameters according to this reference. In Ref. [14], c_p, c_v, and thus γ are functions of T (thermally perfect gas), whereas in the present ES model, they do not depend on T (calorically

FIG. 10. Profiles of $\check{\rho}$, $\check{v}$, and $\check{T}$ at $M_- = 1.2$ for $\delta = 4$, $\mathrm{Pr} = 0.761$, $A_c = \mathrm{const}$, and $\mu_b/\mu = 100, 200, 500, 1000$, and 2000 in the new coordinate y_1. (a) Profiles for $-0.5 \leqslant y_1 \leqslant 8$; (b) profiles for $-0.12 \leqslant y_1 \leqslant 0.2$. The red curves indicate $\check{\rho}$, the green curves $\check{v}$, and the blue curves $\check{T}$. See the caption of Fig. 7 for the types of lines.
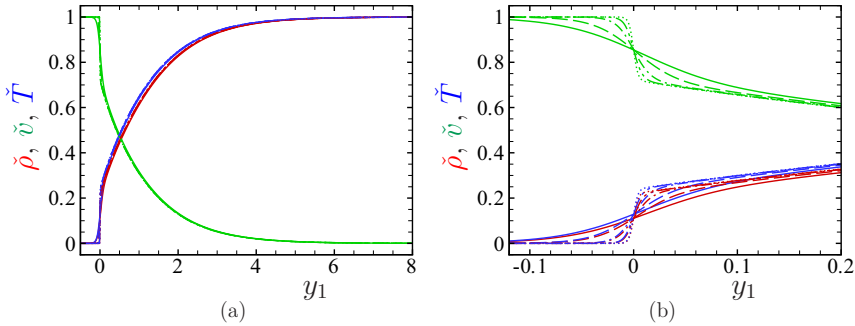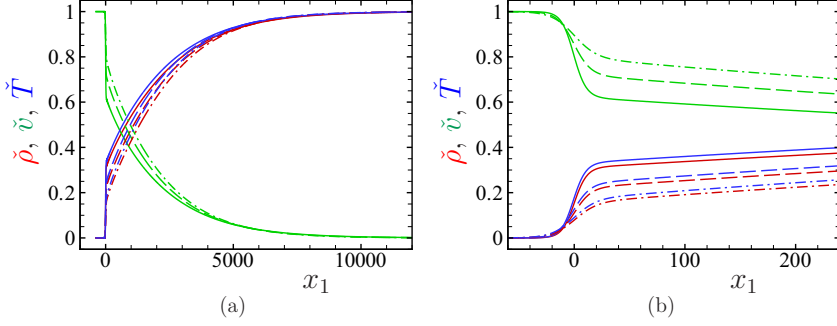
FIG. 11. Profiles of $\check{\rho}$, $\check{v}$, and $\check{T}$ at $M_- = 1.2$ for $\text{Pr} = 0.761$, $A_c = \text{const}$, $\mu_b/\mu = 1000$, and $\delta = 3, 4$, and 5. (a) Profiles for $-1000 \leqslant x_1 \leqslant 12000$; (b) profiles for $-60 \leqslant x_1 \leqslant 240$. The red curves indicate $\check{\rho}$, the green curves $\check{v}$, and the blue curves $\check{T}$. The solid lines indicate the profiles for $\delta = 3$, the dashed lines for $\delta = 4$, and the dot-dashed lines for $\delta = 5$.

perfect gas). Therefore, it is not possible to make a perfect comparison. Nevertheless, we will try the best comparison. In Ref. [14], the (shear) viscosity μ, the bulk viscosity μ_b (ν in Ref. [14]), and the thermal conductivity κ are expressed as (Eq. (7) in Ref. [14]),

$$\mu = p\tau_S, \quad \mu_b = \left(\frac{2}{3} - \frac{R}{c_v}\right)p\tau_\Pi, \quad \kappa = \left(1 + \frac{c_v}{R}\right)Rp\tau_q, \tag{45}$$

where τ_Π, τ_S, and τ_q are the relaxation times for the dynamic pressure, the shear stress, and the heat flux, respectively. It is also assumed that $\mu \propto T^n$, $\mu_b \propto T^n$, and $\kappa \propto T^n c_v(T)/R$ (Eq. (14) in Ref. [14]). Assuming that $\gamma(T) = \text{const} = \gamma_0$ in Eq. (15) in Ref. [14], we obtain

$$\tau_\Pi = \tau_\Pi(\rho_0, T_0)\frac{\rho_0}{\rho}\left(\frac{T_0}{T}\right)^{1-n}, \quad \tau_S = \tau_S(\rho_0, T_0)\frac{\rho_0}{\rho}\left(\frac{T_0}{T}\right)^{1-n}, \quad \tau_q = \tau_q(\rho_0, T_0)\frac{\rho_0}{\rho}\left(\frac{T_0}{T}\right)^{1-n}. \tag{46}$$

Then, we have the following relations:

$$\delta = \frac{2c_v}{R} - 3, \quad \text{Pr} = \frac{\tau_S(\rho_0, T_0)}{\tau_q(\rho_0, T_0)}, \quad \frac{\mu_b}{\mu} = \left(\frac{2}{3} - \frac{R}{c_v}\right)\frac{\tau_\Pi(\rho_0, T_0)}{\tau_S(\rho_0, T_0)}. \tag{47}$$
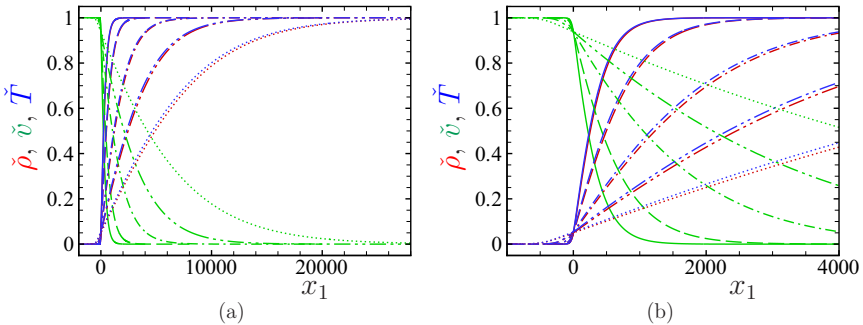

FIG. 12. Profiles of $\check{\rho}$, $\check{v}$, and $\check{T}$ at $M_- = 1.138\ldots$ $(\widetilde{M}_- = 1)$ for $\delta = 4$, $\text{Pr} = 0.761$, $A_c = \text{const}$, and $\mu_b/\mu = 100, 200, 500, 1000$, and 2000. (a) Profiles for $-2000 \leqslant x_1 \leqslant 28\,000$; (b) profiles for $-1000 \leqslant x_1 \leqslant 4000$. The red curves indicate $\check{\rho}$, the green curves $\check{v}$, and the blue curves $\check{T}$. The solid lines indicate the profiles for $\mu_b/\mu = 100$, the dashed lines for $\mu_b/\mu = 200$, the dot-dashed lines for $\mu_b/\mu = 500$, the dot-dot-dashed lines for $\mu_b/\mu = 1000$, and the dotted lines for $\mu_b/\mu = 2000$.
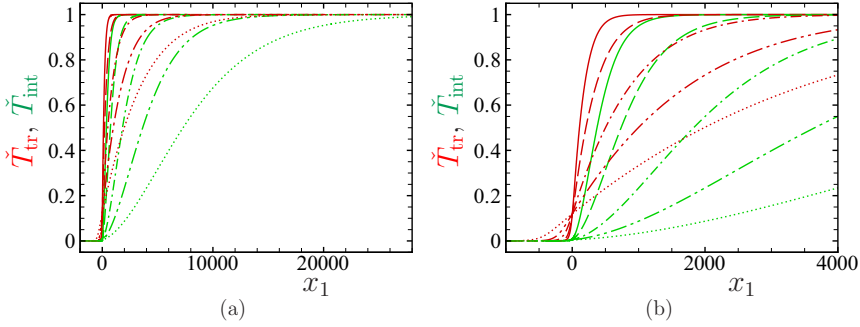
FIG. 13. Profiles of $\check{T}_{tr}$ and $\check{T}_{int}$ at $M_- = 1.138\ldots(\widetilde{M}_- = 1)$ for $\delta = 4$, $\mathrm{Pr} = 0.761$, $A_c = \mathrm{const}$, and $\mu_b/\mu = 100, 200, 500, 1000$, and 2000. (a) Profiles for $-2000 \leqslant x_1 \leqslant 28\,000$; (b) profiles for $-1000 \leqslant x_1 \leqslant 4000$. The red curves indicate $\check{T}_{tr}$, and the green curves $\check{T}_{int}$. See the caption of Fig. 12 about the types of lines.

In Ref. [14], the following values are used: $c_v/R = 3.45$, $\tau_S(\rho_0, T_0) = 1.6 \times 10^{-9}$ s, $\tau_q(\rho_0, T_0) = 2.2 \times 10^{-9}$ s, and $\tau_\Pi(\rho_0, T_0) = 2.2 \times 10^{-5}$ s, so that we have $\delta = 3.9$, $\mathrm{Pr} = 0.73$, and $\mu_b/\mu = 5.2 \times 10^3$. This leads to the following values of the parameters ν and θ in the ES model: $\nu = -0.3698\ldots$ and $\theta = 9.926\ldots \times 10^{-5}$. In addition, since $n = 0.935$ is assumed in Ref. [14], we let $\hat{A}_c = \hat{T}^{0.065}$. The comparison is made with this parameter setting.

Figure 15 shows the comparison between Fig. 6 in Ref. [14] and the present computation for $M_- = 1.47$. Only the profiles of $\hat{\rho}$, $\hat{v}_1$ ($\hat{v}$ in the figure), and $\hat{T}$ are compared. These figures are taken from Fig. 6 in Ref. [14], where the black solid lines indicate the result based on the extended thermodynamics, the dashed lines that based on the Navier-Stokes Fourier theory, and the circles in the profile of $\hat{\rho}$ the experimental result in Ref. [19] (see the caption of Fig. 6 in Ref. [14]). Our results are overdrawn by colored lines. Here, $\hat{x}$ is the coordinate used in Ref. [14], which is related to our x_1 as follows:

$$\hat{x} = x_1 \left(\frac{8}{\pi} \frac{\delta+3}{\delta+5} \right)^{1/2} \frac{\tau_q}{\tau_\Pi} = x_1 \left(\frac{8}{\pi} \frac{\delta+3}{\delta+5} \right)^{1/2} \theta. \tag{48}$$

That is, $\hat{x}$ has the same length scale as y_1 introduced in Eq. (44). In the magnified figures, we have shifted our results slightly to make two results coincide. The figures show very good agreement between the results based on the extended thermodynamics and our results except that there is a very
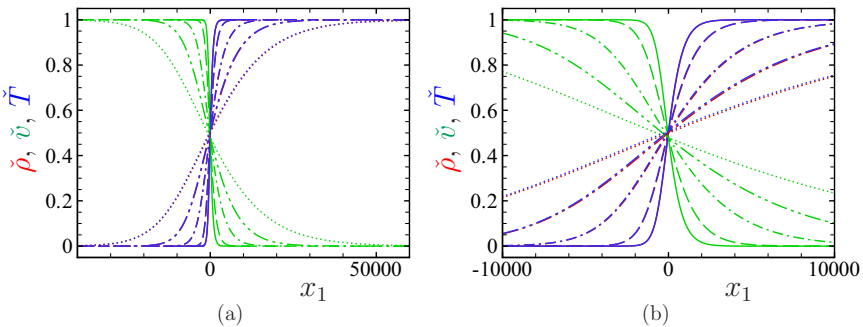

FIG. 14. Profiles of $\check{\rho}$, $\check{v}$, and $\check{T}$ at $M_- = 1.05$ for $\delta = 4$, $\mathrm{Pr} = 0.761$, $A_c = \mathrm{const}$, and $\mu_b/\mu = 100, 200, 500, 1000$, and 2000. (a) Profiles for $-40\,000 \leqslant x_1 \leqslant 60\,000$; (b) profiles for $-10\,000 \leqslant x_1 \leqslant 10\,000$. The red curves indicate $\check{\rho}$, the green curves $\check{v}$, and the blue curves $\check{T}$. The solid lines indicate the profiles for $\mu_b/\mu = 100$, the dashed lines for $\mu_b/\mu = 200$, the dot-dashed lines for $\mu_b/\mu = 500$, the dot-dot-dashed lines for $\mu_b/\mu = 1000$, and the dotted lines for $\mu_b/\mu = 2000$.
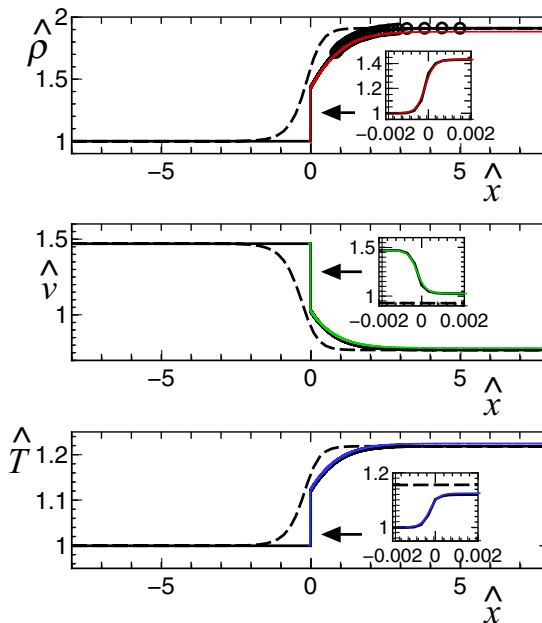
FIG. 15. Comparison between the profiles in Ref. [14] and those in the present computation at $M_- = 1.47$. The figure is a reproduction of a part of Fig. 6 in Ref. [14] (courtesy of S. Taniguchi): The solid lines indicate the result based on the extended thermodynamics, the dashed lines that based on the Navier-Stokes Fourier theory, and the circles in the profile of $\hat{\rho}$ the experimental result in Ref. [19] (see the caption of Fig. 6 in Ref. [14]). The present result is overdrawn by colored lines: The red line is for $\hat{\rho}$, the green line for $\hat{v}_1$ (denoted by $\hat{v}$ in the figure according to Ref. [14]), and the blue line for $\hat{T}$.

slight difference in the downstream uniform state. This is due to the fact that when γ depends on T, the downstream conditions are not the same as those given by the Rankine-Hugoniot relations (2).

V. ASYMPTOTIC ANALYSIS FOR LARGE μ_b/μ

A. Slowly varying solution and shock profile

The numerical results in Sec. IV D suggest that the thick layer behind the thin layer of type-C profile for large μ_b/μ (i.e., small θ) may be described by a slowly varying solution whose length scale of variation is of the order $1/\theta$. Although the results are not shown in Sec. IV D, the replot of the curves in Figs. 12–14 in terms of the variable y_1 [Eq. (44)] shows that the profiles of each macroscopic quantity for large μ_b/μ fall on a single curve for respective M_-, as the profiles of the thick rear layer in Figs. 5(a) and 10(a). Therefore, we expect that the slowly varying solution may also describe the whole profiles of types A and B. In order to obtain the slowly varying solution, we need to introduce the new space coordinates y_i contracted by the small parameter θ, i.e.,

$$y_i = \frac{2}{\sqrt{\pi}} \theta x_i. \tag{49}$$

If we assume that $f = f(y_1, \boldsymbol{\zeta}, \hat{\mathcal{E}})$, then Eq. (16) becomes

$$\theta \zeta_1 \frac{\partial \hat{f}}{\partial y_1} = \hat{A}_c(\hat{T}) \hat{\rho} (\hat{\mathcal{G}} - \hat{f}). \tag{50}$$

We analyze this equation for $\theta \ll 1$ by a Hilbert-type expansion in θ, i.e.,

$$\hat{f} = \hat{f}^{(0)} + \hat{f}^{(1)}\theta + \hat{f}^{(2)}\theta^2 + \cdots. \tag{51}$$

Correspondingly, the macroscopic quantities $\hat{\rho}$, $\hat{v}_i$, $\hat{p}_{ij}$, ..., which we denote by $\hat{h}$, are expanded as

$$\hat{h} = \hat{h}^{(0)} + \hat{h}^{(1)}\theta + \hat{h}^{(2)}\theta^2 + \cdots. \tag{52}$$

We leave the details of the analysis in Appendix C, where the three-dimensional version of Eq. (50) [Eq. (C2)] is analyzed. As the result of the analysis, the macroscopic equations that describe the leading-order quantities $\hat{\rho}^{(0)}$, $\hat{v}_i^{(0)}$, $\hat{T}_{\text{tr}}^{(0)}$, and $\hat{T}_{\text{int}}^{(0)}$ of the expansion Eq. (52) are obtained, i.e., Eqs. (C34a) and (C34b) and two equations out of Eqs. (C34c), (C40), and (C45).

Let us consider the one-dimensional case assuming that $\partial/\partial y_2 = \partial/\partial y_3 = 0$ and $\hat{v}_2^{(0)} = \hat{v}_3^{(0)} = 0$ and omit the superscript (0) for brevity. If we choose Eqs. (C34) and (C45) as the governing equations, these equations reduce to the following system:

$$\frac{d}{dy_1}(\hat{\rho}\hat{v}_1) = 0, \tag{53a}$$

$$\frac{d}{dy_1}\left(\frac{\hat{T}_{\text{tr}}}{\hat{v}_1} + 2\hat{v}_1\right) = 0, \tag{53b}$$

$$\frac{d}{dy_1}\left(\hat{v}_1^2 + \frac{5}{2}\hat{T}_{\text{tr}} + \frac{\delta}{2}\hat{T}_{\text{int}}\right) = 0, \tag{53c}$$

$$\hat{v}_1\frac{d\hat{T}_{\text{int}}}{dy_1} = \frac{3}{3+\delta}\hat{A}_c(\hat{T})\hat{\rho}(\hat{T}_{\text{tr}} - \hat{T}_{\text{int}}), \tag{53d}$$

where the relation (C41), i.e.,

$$\hat{T} = \frac{3\hat{T}_{\text{tr}} + \delta\hat{T}_{\text{int}}}{3+\delta}, \tag{54}$$

has been used except that $\hat{T}$ is still kept in $\hat{A}_c(\hat{T})$. We note here that $(\hat{\rho}, \hat{v}_1, \hat{T}_{\text{tr}}, \hat{T}_{\text{int}})$ are equal to $(1, \hat{v}_-, 1, 1)$ at upstream infinity and to $(\hat{\rho}_+, \hat{v}_+, \hat{T}_+, \hat{T}_+)$ at downstream infinity, and they are related by the dimensionless Rankine-Hugoniot relations (24) or the original conservation laws

$$\hat{\rho}_+\hat{v}_+ = \hat{v}_-, \quad \frac{\hat{T}_+}{\hat{v}_+} + 2\hat{v}_+ = \frac{1}{\hat{v}_-} + 2\hat{v}_-, \quad \hat{v}_+^2 + \frac{5+\delta}{2}\hat{T}_+ = \hat{v}_-^2 + \frac{5+\delta}{2}, \tag{55}$$

which are the dimensionless version of Eq. (A11).

It follows from Eqs. (53a)–(53c) that

$$\hat{\rho}\hat{v}_1 = c_1, \quad \frac{\hat{T}_{\text{tr}}}{\hat{v}_1} + 2\hat{v}_1 = c_2, \quad \hat{v}_1^2 + \frac{5}{2}\hat{T}_{\text{tr}} + \frac{\delta}{2}\hat{T}_{\text{int}} = c_3, \tag{56}$$

where c_1, c_2, and c_3 are constants, or

$$\hat{\rho} = \frac{c_1}{\hat{v}_1}, \quad \hat{T}_{\text{tr}} = \hat{v}_1(c_2 - 2\hat{v}_1), \quad \hat{T}_{\text{int}} = \frac{2}{\delta}\left(c_3 - \frac{5}{2}c_2\hat{v}_1 + 4\hat{v}_1^2\right). \tag{57}$$

The substitution of Eq. (57) into Eq. (53d) with Eq. (54) gives the following equation for $\hat{v}_1$:

$$\hat{v}_1^2\left(\frac{5}{16}c_2 - \hat{v}_1\right)\frac{d\hat{v}_1}{dy_1} = \frac{3(4+\delta)}{8(3+\delta)}c_1\hat{A}_c(\hat{T})\left[\hat{v}_1^2 - \frac{5+\delta}{2(4+\delta)}c_2\hat{v}_1 + \frac{c_3}{4+\delta}\right], \tag{58a}$$

$$\hat{T} = \frac{2}{3+\delta}\left(\hat{v}_1^2 - c_2\hat{v}_1 + c_3\right). \tag{58b}$$

In the case of the type-C profile, the slowly varying solution should be applied to the downstream of the thin front layer, so that c_1, c_2, and c_3 in Eq. (56) are determined from the downstream condition as $c_1 = \hat{\rho}_+\hat{v}_+$, $c_2 = (\hat{T}_+/\hat{v}_+) + 2\hat{v}_+$, and $c_3 = \hat{v}_+^2 + [(5+\delta)/2]\hat{T}_+$. However, these downstream quantities are expressed in terms of the upstream quantities by Eq. (55). Therefore, we can express c_1, c_2, and c_3 using the upstream quantities as

$$c_1 = \hat{v}_-, \quad c_2 = \frac{1}{\hat{v}_-} + 2\hat{v}_-, \quad c_3 = \hat{v}_-^2 + \frac{5+\delta}{2}. \tag{59}$$

Using these relations and the ratio of specific heats $\gamma = (5+\delta)/(3+\delta)$, we can transform Eq. (58) as follows:

$$\hat{v}_1^2(\hat{v}_* - \hat{v}_1)\frac{d\hat{v}_1}{dy_1} = -\frac{3(\gamma+1)}{16}\hat{v}_-\hat{A}_c(\hat{T})(\hat{v}_- - \hat{v}_1)(\hat{v}_1 - \hat{v}_+), \tag{60a}$$

$$\hat{T}(\hat{v}_1) = 1 + (\gamma-1)(\hat{v}_1 - \hat{v}_-)\left(\hat{v}_1 - \frac{1+\hat{v}_-^2}{\hat{v}_-}\right), \tag{60b}$$

where $\hat{v}_*$ and $\hat{v}_+$ (downstream velocity) are expressed in terms of $\hat{v}_-$ as

$$\hat{v}_* = \frac{5}{16}\frac{1+2\hat{v}_-^2}{\hat{v}_-}, \quad \hat{v}_+ = \frac{(\gamma-1)\hat{v}_-^2 + \gamma}{(\gamma+1)\hat{v}_-}. \tag{61}$$

Let us consider the integration of Eq. (60), with an initial condition $\hat{v}_1 = \hat{v}_0$ at $y_1 = y_0$, from $y_1 = y_0$ to ∞. When $\hat{v}_1 < \hat{v}_*$ and $\hat{v}_1 \in (\hat{v}_+, \hat{v}_-)$ (note that $\hat{v}_+ < \hat{v}_-$), $d\hat{v}_1/dy_1$ is negative from Eq. (60). This range of $\hat{v}_1$ is not empty because $\hat{v}_+ < \hat{v}_*$ for $\gamma < 5/3$ and $M_- > 1$. This can be shown easily from the relation

$$\frac{\hat{v}_*}{\hat{v}_+} = \frac{5}{16}(\gamma+1)\frac{2\hat{v}_-^2 + 1}{(\gamma-1)\hat{v}_-^2 + \gamma} = \frac{5}{8}\frac{\gamma+1}{\gamma}\frac{\gamma M_-^2 + 1}{(\gamma-1)M_-^2 + 2}. \tag{62}$$

Therefore, if the initial value $\hat{v}_0$ satisfies $\hat{v}_0 < \hat{v}_*$ and $\hat{v}_0 \in (\hat{v}_+, \hat{v}_-)$, the solution $\hat{v}_1$ monotonically decreases as y_1 increases and approaches $\hat{v}_+$, which is an equilibrium point of $\hat{v}_1$ where $d\hat{v}_1/dy_1$ vanishes. This means that, with an appropriate choice of the initial value $\hat{v}_0$, the solution of Eq. (60) is expected to describe the velocity profile in the downstream range $y_1 \in [y_0, \infty)$ of a shock wave. Once the solution $\hat{v}_1$ is obtained from Eq. (60), other quantities are obtained from Eq. (57). That is,

$$\hat{\rho}(\hat{v}_1) = \frac{\hat{v}_-}{\hat{v}_1}, \quad \hat{T}_{\text{tr}}(\hat{v}_1) = 1 + 2(\hat{v}_- - \hat{v}_1)\left(\hat{v}_1 - \frac{1}{2\hat{v}_-}\right), \tag{63a}$$

$$\hat{T}_{\text{int}}(\hat{v}_1) = 1 + \frac{8}{\delta}(\hat{v}_1 - \hat{v}_-)(\hat{v}_1 - \hat{v}_{**}), \tag{63b}$$

where $\hat{v}_{**}$ is the dimensionless downstream velocity of the shock wave when $\theta = 0$, which is defined by Eq. (26a) and is written in terms of $\hat{v}_-$ as $\hat{v}_{**} = (2\hat{v}_-^2 + 5)/8\hat{v}_-$. Equation (60) with the initial condition $\hat{v}_1(y_0) = \hat{v}_0$ can be solved analytically. More specifically, $\hat{v}_1$ is obtained as the inverse function of the following function $y_1(\hat{v}_1)$:

$$y_1(\hat{v}_1) - y_0 = \frac{16}{3(\gamma+1)\hat{v}_-}\int_{\hat{v}_1}^{\hat{v}_0}\frac{u^2(\hat{v}_* - u)}{\hat{A}_c(\hat{T}(u))(\hat{v}_- - u)(u - \hat{v}_+)}du. \tag{64}$$

Moreover, the integration can be carried out explicitly for special forms of $\hat{A}_c(\hat{T})$, such as $\hat{A}_c(\hat{T}) = 1$, $\sqrt{\hat{T}}$, and $\hat{T}$. The results are given in Appendix D.

Finally, we discuss the possible choices of the initial value $\hat{v}_0$ and the relation between the resulting solution $\hat{v}_1$ [and Eq. (63)] and the profiles of types A, B, and C. Here, we note that $\widetilde{M}_- < M_-$ holds (see the end of Appendix A 3):

(i) Case of $\widetilde{M}_- < 1 < M_-$:

Since $\widetilde{M}_- = \sqrt{6/5}\hat{v}_-$, it follows from Eq. (61) that $\hat{v}_- < \hat{v}_*$. Therefore, the admissible range of the initial value $\hat{v}_0$, i.e., $\hat{v}_0 < \hat{v}_*$ and $\hat{v}_0 \in (\hat{v}_+, \hat{v}_-)$, reduces to just $\hat{v}_0 \in (\hat{v}_+, \hat{v}_-)$. That is, we can take $\hat{v}_0$ as *almost* $\hat{v}_-$, i.e., $\hat{v}_0 = \hat{v}_- - 0$. Therefore, the solution $\hat{v}_1$ is expected to describe the whole profile of the velocity. Let us consider this point in more detail. We consider Eq. (64) for a fixed value of $\hat{v}_1$ in the middle of the profile, $\hat{v}_+ < \hat{v}_1 < \hat{v}_-$. Then, we have the following estimate:

$$y_1(\hat{v}_1) - y_0 > C_y(\hat{v}_1) \int_{\hat{v}_1}^{\hat{v}_0} \frac{1}{\hat{v}_- - u} du = C_y(\hat{v}_1)[-\ln(\hat{v}_- - \hat{v}_0) + \ln(\hat{v}_- - \hat{v}_1)], \qquad (65)$$

where

$$C_y(\hat{v}_1) = \frac{16}{3(\gamma + 1)\hat{v}_-} \frac{\hat{v}_1^2(\hat{v}_* - \hat{v}_0)}{\max_{\hat{v}_1 \leqslant u \leqslant \hat{v}_0}[\hat{A}_c(\hat{T}(u))](\hat{v}_0 - \hat{v}_+)} > 0. \qquad (66)$$

As the initial value $\hat{v}_0$ approaches the upstream velocity $\hat{v}_-$, the coordinate $y_1(\hat{v}_1)$, which expresses the coordinate y_1 inside the shock profile, diverges to $+\infty$. To locate the shock profile in a more comfortable range with finite y_1, we need to shift the coordinate, or take the initial position y_0 as $-\infty$. Theoretically, if we assume that $\hat{v}_0 \to \hat{v}_-$ at $y_1 \to -\infty$, we obtain the whole profile of $\hat{v}_1$, changing from $\hat{v}_-$ to $\hat{v}_+$, in a range of finite y_1. Correspondingly, $\hat{\rho}$ changes from $\hat{\rho}(\hat{v}_-) = 1$ to $\hat{\rho}(\hat{v}_+) = \hat{\rho}_+$, $\hat{T}_{tr}$ changes from $\hat{T}_{tr}(\hat{v}_-) = 1$ to $\hat{T}_{tr}(\hat{v}_+) = \hat{T}_+$, and $\hat{T}_{int}$ changes from $\hat{T}_{int}(\hat{v}_-) = 1$ to $\hat{T}_{int}(\hat{v}_+) = \hat{T}_+$. This solution corresponds to the whole profile of type A.

(ii) Case of $\widetilde{M}_- = 1$:

In this case, it follows from Eq. (61) that $\hat{v}_* = \hat{v}_- = \sqrt{5/6}$. Therefore, the admissible range of the initial value $\hat{v}_0$ is still $\hat{v}_0 \in (\hat{v}_+, \hat{v}_-)$. However, Eq. (64) reduces to

$$y_1(\hat{v}_1) - y_0 = \frac{16}{3(\gamma + 1)\hat{v}_-} \int_{\hat{v}_1}^{\hat{v}_0} \frac{u^2}{\hat{A}_c(\hat{T}(u))(u - \hat{v}_+)} du. \qquad (67)$$

Since the integrand does not have a singularity at $u = \hat{v}_-$, the integral takes a finite value at $\hat{v}_0 = \hat{v}_-$ for a fixed value of $\hat{v}_1$ in the middle of the profile, $\hat{v}_+ < \hat{v}_1 < \hat{v}_-$. This means that y_0 can be a finite value, say $y_0 = 0$, and the velocity profile locates in a range with finite y_1. Therefore, the solution $\hat{v}_1$ can describe the whole velocity profile $\hat{v}_- \to \hat{v}_+$ in the range $y_1 \in [y_0, \infty)$. From Eq. (60), we observe that

$$\left.\frac{d\hat{v}_1}{dy_1}\right|_{y_1=y_0} = -\frac{3(\gamma + 1)}{16}\hat{A}_c(1)\frac{\hat{v}_- - \hat{v}_+}{\hat{v}_-} < 0. \qquad (68)$$

This means that the profile of the velocity suddenly start at $y_1 = y_0$ with a finite gradient and approaches $\hat{v}_+$ as $y_1 \to \infty$. In other words, the velocity profile exhibits a corner at $y_1 = y_0$. From Eq. (63a), it follows that

$$\left.\frac{d\hat{\rho}}{dy_1}\right|_{y_1=y_0} = -\frac{1}{\hat{v}_-}\left.\frac{d\hat{v}_1}{dy_1}\right|_{y_1=y_0} > 0, \quad \left.\frac{d\hat{T}_{tr}}{dy_1}\right|_{y_1=y_0} = -2\left(\hat{v}_- - \frac{1}{2\hat{v}_-}\right)\left.\frac{d\hat{v}_1}{dy_1}\right|_{y_1=y_0} > 0. \qquad (69)$$

Therefore, profiles of $\hat{\rho}$ and $\hat{T}_{tr}$ show the same behavior. However, from Eq. (63b), we have

$$\left.\frac{d\hat{T}_{int}}{dy_1}\right|_{y_1=y_0} = \frac{8}{\delta}(\hat{v}_- - \hat{v}_{**})\left.\frac{d\hat{v}_1}{dy_1}\right|_{y_1=y_0} = 0, \qquad (70)$$

because $\hat{v}_{**} = \hat{v}_{-} = \sqrt{5/6}$ [Eq. (26a)]. Therefore, the profile of $\hat{T}_{int}$ does not exhibit a corner at $y_1 = y_0$. These results are consistent with the numerical solution in Sec. IV D 2 (see Sec. V B). This solution corresponds to the type-B profile.

(iii) Case of $\widetilde{M}_{-} > 1$:

Because $\hat{v}_{*} < \hat{v}_{-}$ in this case, the admissible range for the initial value reduces to $\hat{v}_0 \in (\hat{v}_{+}, \hat{v}_{*})$. Here, we should note that $\hat{v}_{+} < \hat{v}_{**} < \hat{v}_{*}$ holds. Therefore, we can take $\hat{v}_{**}$, which is the dimensionless downstream velocity of the shock wave when $\theta = 0$ [Eq. (26a)], as the initial value $\hat{v}_0$. Then, the solution $\hat{v}_1$ describes the monotonic decrease from $\hat{v}_{**}$ to $\hat{v}_{+}$ as y_1 varies from y_0 to ∞. Correspondingly, $\hat{\rho}$ changes from $\hat{\rho}(\hat{v}_{**}) = \hat{\rho}_{**}$ to $\hat{\rho}(\hat{v}_{+}) = \hat{\rho}_{+}$, $\hat{T}_{tr}$ changes from $\hat{T}_{tr}(\hat{v}_{**}) = \hat{T}_{**}$ to $\hat{T}_{tr}(\hat{v}_{+}) = \hat{T}_{+}$, and $\hat{T}_{int}$ changes from $\hat{T}_{int}(\hat{v}_{**}) = 1$ to $\hat{T}_{int}(\hat{v}_{+}) = \hat{T}_{+}$, where $\hat{\rho}_{**}$ and $\hat{T}_{**}$ are, respectively, the values of $\hat{\rho}$ and $\hat{T}_{tr}$ downstream of the shock wave with $\theta = 0$ [Eq. (26)]. This corresponds to the thick rear layer of the type-C profile. To be more specific, we replace the thin front layer with a jump satisfying the Rankine-Hugoniot relations for $\theta = 0$ and the thick layer with the solution corresponding to $\hat{v}_1$ obtained here. In this way, we can describe the type-C profile by the slowly varying solution.

In summary, the slowly varying solution, i.e., $\hat{v}_1$ obtained from Eq. (64) and the corresponding $\hat{\rho}$, $\hat{T}_{tr}$, and $\hat{T}_{int}$ in Eq. (63), can successfully describe the type-A profile when $\widetilde{M}_{-} < 1 < M_{-}$, the type-B profile when $\widetilde{M}_{-} = 1$, and the type-C profile, with the help of the Rankine-Hugoniot relations for $\theta = 0$ [Eq. (26) or (A20) with $\hat{T}_{tr-} = \hat{T}_{-}$], when $\widetilde{M}_{-} > 1$.

In Ref. [30], the shock-wave structure of a polyatomic gas is investigated by a set of macroscopic equations that is derived by the extended thermodynamics [31] or from the Boltzmann equation by an appropriate moment closure [31,32] (see also Ref. [30]). In this Boltzmann equation, the internal modes are modeled by a single continuous variable [22] as in the ES model used here. The macroscopic equations expressed in terms of the slowly varying variable y_1 in Eq. (44) are essentially the same as our equations (53). It should also be mentioned that a system of macroscopic equations corresponding to a slowly varying kinetic solution has been obtained to describe the structure of a shock wave in a gas mixture with slow chemical reactions in Ref. [41], where the profiles are classified according to the parameters.

B. Comparison with numerical results

In this subsection, we compare the slowly varying solution with the numerical solutions. The pseudo-CO$_2$ gas with $\mu_b/\mu = 100$ and 1000 gives $\theta = 5.00... \times 10^{-3}$ and $5.00... \times 10^{-4}$, respectively, which are quite small. Therefore, we expect from its derivation that the leading-order slowly varying solution obtained in Sec. V A describes the shock profile accurately. To confirm this statement, we consider the case of $\mu_b/\mu = 100$, for which the leading-order solution should be less accurate than the case of $\mu_b/\mu = 1000$, and make some comparisons. In Figs. 16–19 below, $x_1 = 0$ is set in the same way as in Figs. 2, 7, 12, and 14, respectively, for the numerical solution. Then, the profiles obtained by the slowly varying solution is shifted in such a way that the point at which $\check{\rho} = 0.5$ coincides with that of the numerical solution.

Figure 16 shows the profiles of $\check{\rho}$, $\check{v}$, and $\check{T}$ at $M_{-} = 5$ and for $\mu_b/\mu = 100$. Figure 16(b) is a magnified figure of Fig. 16(a). The colored lines show the numerical solution obtained in Sec. IV D 2: the red line indicates $\check{\rho}$, the green line $\check{v}$, and the blue line $\check{T}$. The black dot-dashed line indicates the profile of the thick rear layer obtained on the basis of the Rankine-Hugoniot relations for $\mu_b/\mu = \infty$ [Eq. (A20) with $\hat{T}_{Tr-} = \hat{T}_{-}$] and the slowly varying solution corresponding to Eq. (64) in the case of $\widetilde{M}_{-} > 1$ (see Sec. V A). In Fig. 16(b), the numerical result for $\mu_b/\mu = \infty$ is also shown by the black dashed line. As one can see, the slowly varying solution describes perfectly the profiles in the thick rear layer. Figure 17 shows the profiles at $M_{-} = 1.2$ and for $\mu_b/\mu = 100$, where the colors and types of the lines are the same as Fig. 16. In this case, the profiles of the rear layer given by the slowly varying solution deviates slightly from the numerical solution. However, we can say that the agreement is still good. Figures 16 and 17 correspond to type-C profile.
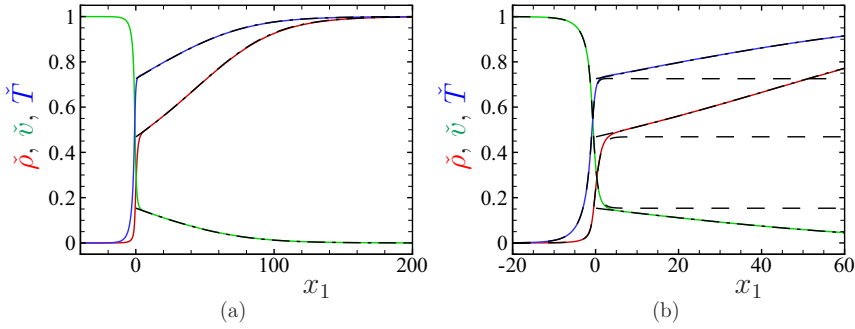
FIG. 16. Comparison between the profiles based on the slowly varying solution and those of numerical solution. Profiles of $\check{\rho}$, $\check{v}$, and $\check{T}$ at $M_- = 5$ for $\delta = 4$, $\mathrm{Pr} = 0.761$, $A_c = \mathrm{const}$, and $\mu_b/\mu = 100$ are shown in the figure. (a) Profiles for $-40 \leqslant x_1 \leqslant 200$; (b) profiles for $-20 \leqslant x_1 \leqslant 60$. The red line indicates $\check{\rho}$, the green line $\check{v}$, and the blue line $\check{T}$ of the numerical solution. The black dot-dashed line indicates the corresponding profiles obtained on the basis of the slowly varying solution. In panel (b), the numerical solution of the ES model for $\mu_b/\mu = \infty$ is also shown by the black dashed line.

The comparison of the profiles at $M_- = 1.138...$ ($\widetilde{M}_- = 1$) and for $\mu_b/\mu = 100$ is made in Fig. 18. As in Figs. 16 and 17, Fig. 18(b) is a magnified figure. Note that the scale of $\check{v}$ is shown on the right side in Fig. 18(b). In this case, the slowly varying solution based on Eq. (64) gives a profile that starts suddenly with a corner, as shown by the dot-dashed lines in Fig. 18(b). We may call this case *strict* type B. It agrees with the numerical solution on the whole, though there is a visible difference in the magnified figure, Fig. 18(b). The numerical solution gives profiles that start smoothly without a corner. However, as μ_b/μ becomes large, say 1000, the start of the profiles becomes sharper, and the difference between the numerical and slowly varying solutions becomes invisible.

Figure 19 shows the comparison of the profiles at $M_- = 1.05$ and for $\mu_b/\mu = 100$. In this case, the agreement between the numerical and slowly varying solutions is good even in the magnified Fig. 19(b). This corresponds to type-A profile.

In this subsection, we compared the numerical and slowly varying solutions for the pseudo-CO_2 gas with a smaller μ_b/μ, i.e., $\mu_b/\mu = 100$, and confirmed the agreement. It should be emphasized that we have much better agreement for the real CO_2 gas with μ_b/μ of the order of 1000.

FIG. 17. Comparison between the profiles based on the slowly varying solution and those of numerical solution. Profiles of $\check{\rho}$, $\check{v}$, and $\check{T}$ at $M_- = 1.2$ for $\delta = 4$, $\mathrm{Pr} = 0.761$, $A_c = \mathrm{const}$, and $\mu_b/\mu = 100$ are shown in the figure. (a) Profiles for $-100 \leqslant x_1 \leqslant 1200$; (b) profiles for $-40 \leqslant x_1 \leqslant 200$. See the caption of Fig. 16.
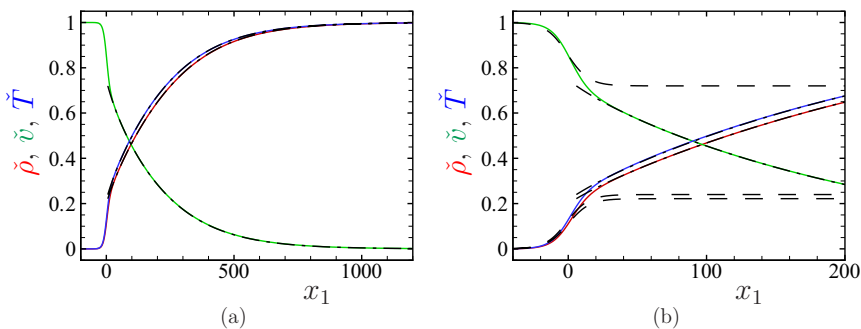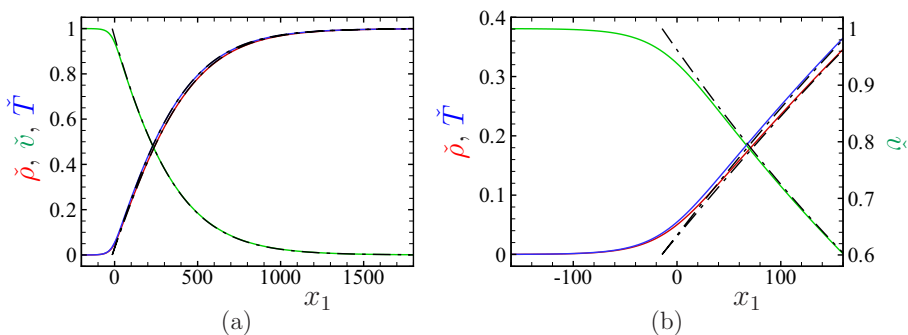
FIG. 18. Comparison between the profiles based on the slowly varying solution and those of numerical solution. Profiles of $\check{\rho}$, $\check{v}$, and $\check{T}$ at $M_- = 1.138...$ ($\widetilde{M}_- = 1$) for $\delta = 4$, $\mathrm{Pr} = 0.761$, $A_c = \mathrm{const}$, and $\mu_b/\mu = 100$ are shown in the figure. (a) Profiles for $-200 \leqslant x_1 \leqslant 1800$; (b) profiles for $-160 \leqslant x_1 \leqslant 160$. The red line indicates $\check{\rho}$, the green line $\check{v}$, and the blue line $\check{T}$ of the numerical solution. The black dot-dashed line indicates the corresponding profiles obtained on the basis of the slowly varying solution.

VI. CONCLUDING REMARKS

In the present study, we investigated the structure of a standing shock wave in a polyatomic gas with a large bulk viscosity on the basis of the polyatomic version of the ES model for the Boltzmann equation. It is known that the CO_2 gas has a large value of the ratio of the bulk viscosity to the viscosity (μ_b/μ), which is of the order of 1000. Therefore, we considered a pseudo-CO_2 gas with the same properties as the CO_2 gas except that μ_b/μ takes arbitrary values and investigated its behavior as μ_b/μ increases up to 2000 to understand the properties of the shock profiles when μ_b/μ is large. The study was motivated by the recent results based on the extended thermodynamics [14–16].

We first carried out direct numerical computations of the ES model and obtained the profiles of the macroscopic quantities inside the shock wave accurately for the pseudo-CO_2 gas and the real CO_2 gas, i.e., the pseudo-CO_2 gas with the real value of μ_b/μ (Sec. IV). In this step, we were able to reproduce the type-A, B, and C profiles defined in Ref. [14] (Fig. 1) at relatively small upstream Mach numbers (i.e., for small $M_- - 1$) for the CO_2 gas. Here, the type-A profile is a profile almost symmetric with respect to the center for each macroscopic quantities, the type-B profile is the profile that is nonsymmetric and has a corner upstream, and the type-C profile is the profile consisting of a thin upstream layer with a sharp change and a thick downstream layer with a slow change. We obtained the type-C profile also for higher upstream Mach numbers, which is consistent with the result in Ref. [16] based on the nonlinear extended thermodynamics. In addition, we observed that

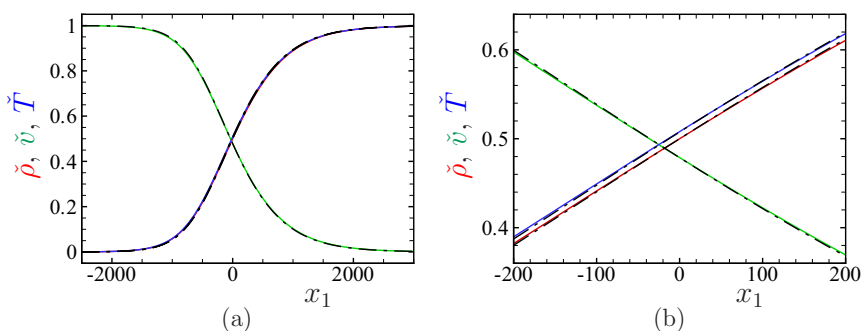FIG. 19. Comparison between the profiles based on the slowly varying solution and those of numerical solution. Profiles of $\check{\rho}$, $\check{v}$, and $\check{T}$ at $M_- = 1.05$ for $\delta = 4$, $\mathrm{Pr} = 0.761$, $A_c = \mathrm{const}$, and $\mu_b/\mu = 100$ are shown in the figure. (a) Profiles for $-2500 \leqslant x_1 \leqslant 3000$; (b) profiles for $-200 \leqslant x_1 \leqslant 200$. See the caption of Fig. 18.

as the ratio μ_b/μ increases, the thin front layer in the type-C profile does not change, whereas the thickness of the thick rear layer increases indefinitely. In the limit when $\mu_b/\mu \to \infty$, the shock wave reduces to the thin upstream layer only and its downstream state approaches a uniform equilibrium state satisfying the different Rankine-Hugoniot relations [Eq. (A20)] that hold when $\mu_b/\mu = \infty$.

Then, motivated by the numerical results, we tried to describe the behavior of the thick rear layer of the type-C profile by a slowly varying solution of the ES model, the length scale of which is of the order of μ_b/μ (or the inverse of the parameter θ appearing in the ES model) (Sec. V). Carrying out an asymptotic analysis for small θ (or large μ_b/μ) using a Hilbert-type expansion, we derived a simple set of ordinary differential equations for the macroscopic quantities, which can be solved analytically. We showed that the type-C profile can be described by this slowly varying solution correctly if its upstream condition is set to be the downstream condition of the Rankine-Hugoniot relations for $\mu_b/\mu = \infty$. This is a kind of revival of the Bethe-Teller theory [17] discussed in Ref. [14]. In addition, we showed that the slowly varying solution can also describe the entire type-A and B profiles correctly.

In this study, we assumed that the ratio μ_b/μ is large (1000 to 2000) for the CO_2 gas according to the literature [28,29]. However, there are some doubts about it, e.g., Ref. [42]. This discrepancy should be an important subject to be investigated. Nevertheless, the slowly varying solution derived here should give a good approximation even if μ_b/μ is much smaller, say, of the order of 10, such as the hydrogen gas for which $\mu_b/\mu \approx 30$ [28,29].

In the present paper, we have restricted ourselves to the structure of the plane shock wave. However, the macroscopic equations corresponding to the slowly varying solution have been derived for the general three-dimensional case. Therefore, they can be applied easily to the structure of a curved shock wave in a polyatomic gas with large bulk viscosity.

Finally, we comment on possible extensions of the present work. The present study is fully based on the ES model, not on the original Boltzmann equation. However, in order to describe the complicated process of energy exchange during collisions and relaxation processes, one needs to introduce some phenomenological models [22,43] even in the Boltzmann equation. Nevertheless, the extension of the present study to such Boltzmann models would be an important problem to be tackled. Another possible extension is to investigate the shock-wave structure for a mixture of polyatomic gases (containing CO_2) by the use of a Boltzmann-type model (e.g., Ref. [44]) or a Bhatnagar-Gross-Krook (BGK)–type model (e.g, [45]) for polyatomic gas mixtures. In the present study, we restricted ourselves to a calorically perfect (or polytropic) gas, for which the specific heat at constant pressure and that at constant volume are constants. The extension of the present study to a thermally perfect (or nonpolytropic) gas with the specific heats depending on the temperature would also be possible if one uses appropriate existing models, such as the Boltzmann-type models in Ref. [22,44] and the BGK-type models in Ref. [45].

APPENDIX A: SOME PROPERTIES OF THE ES MODEL

1. Moments of Gaussian

We first calculate moments of the Gaussian (6b). Let us consider the following moments: With $i, j = 1, 2, 3$,

$$I_0[\mathcal{G}] = \iint_0^\infty \mathcal{G} d\mathcal{E} d\boldsymbol{\xi}, \tag{A1a}$$

$$I_i[\mathcal{G}] = \iint_0^\infty \xi_i \mathcal{G} d\mathcal{E} d\xi = \iint_0^\infty (\xi_i - v_i)\mathcal{G} d\mathcal{E} d\xi + v_i I_0[\mathcal{G}], \tag{A1b}$$

$$I_4[\mathcal{G}] = \iint_0^\infty \mathcal{E} \mathcal{G} d\mathcal{E} d\xi, \tag{A1c}$$

$$I_{ij}[\mathcal{G}] = \iint_0^\infty \xi_i \xi_j \mathcal{G} d\mathcal{E} d\xi = \iint_0^\infty (\xi_i - v_i)(\xi_j - v_j)\mathcal{G} d\mathcal{E} d\xi + v_j I_i[\mathcal{G}] + v_i I_j[\mathcal{G}] - v_i v_j I_0[\mathcal{G}]. \tag{A1d}$$

If we let $x_i = (\xi_i - v_i)/\sqrt{2}$ and $y = \mathcal{E}/RT_{\text{rel}}$, the Gaussian $\mathcal{G}$ [Eq. (6b)] is expressed as

$$\mathcal{G} = \frac{\rho y^{\delta/2-1}}{(2\pi)^{3/2}[\det(\mathsf{T})]^{1/2} R T_{\text{rel}} \Gamma(\delta/2)} \exp(-{}^t\boldsymbol{x}\mathsf{T}^{-1}\boldsymbol{x} - y). \tag{A2}$$

In this subsection, bold-faced letters indicate column vectors; for instance, $\boldsymbol{x}$ is the column vector with components x_1, x_2, and x_3, and ${}^t\boldsymbol{x}$ is its transpose, i.e., ${}^t\boldsymbol{x} = [x_1, x_2, x_3]$. Let us denote the eigenvalues of T^{-1} by $\lambda^{(i)}$ ($i = 1, 2, 3$), where $\lambda^{(i)} > 0$ because T is positive definite, and the orthogonal matrix that diagonalizes T^{-1} by P, i.e.,

$${}^t\mathsf{P}\mathsf{T}^{-1}\mathsf{P} = \text{diag}\,[\lambda^{(1)}, \lambda^{(2)}, \lambda^{(3)}], \tag{A3}$$

where diag [ ] indicates a diagonal matrix. Then, we have $\det(\mathsf{T}) = [\det(\mathsf{T}^{-1})]^{-1} = (\lambda^{(1)}\lambda^{(2)}\lambda^{(3)})^{-1}$. If we introduce the column vector $\boldsymbol{c}$ with components c_1, c_2, and c_3 by $\boldsymbol{x} = \mathsf{P}\boldsymbol{c}$ and another column vector $\boldsymbol{z}$ with components $z_1 = (\lambda^{(1)})^{1/2}c_1$, $z_2 = (\lambda^{(2)})^{1/2}c_2$, and $z_3 = (\lambda^{(3)})^{1/2}c_3$, then we have

$${}^t\boldsymbol{x}\mathsf{T}^{-1}\boldsymbol{x} = {}^t\boldsymbol{c}{}^t\mathsf{P}\mathsf{T}^{-1}\mathsf{P}\boldsymbol{c} = \sum_{i=1}^3 \lambda^{(i)}c_i^2 = |\boldsymbol{z}|^2. \tag{A4}$$

Therefore, the Gaussian $\mathcal{G}$ and $\xi_i - v_i$ are expressed in the following form:

$$\mathcal{G} = \frac{\rho y^{\delta/2-1}}{(2\pi)^{3/2}(\lambda^{(1)}\lambda^{(2)}\lambda^{(3)})^{-1/2} R T_{\text{rel}} \Gamma(\delta/2)} \exp(-|\boldsymbol{z}|^2 - y), \tag{A5a}$$

$$\xi_i - v_i = \sqrt{2}\,x_i = \sqrt{2}\,(\mathsf{P})_{ij}c_j = \sum_{j=1}^3 (2/\lambda^{(j)})^{1/2}(\mathsf{P})_{ij}z_j. \tag{A5b}$$

Let us change the integration variables from $(\mathcal{E}, \xi)$ to $(y, \boldsymbol{z})$ in Eqs. (A1). Then, the domain of integration becomes from 0 to ∞ for y and the whole space for $\boldsymbol{z}$, and the relation $d\mathcal{E} d\xi = 2\sqrt{2}RT_{\text{rel}}(\lambda^{(1)}\lambda^{(2)}\lambda^{(3)})^{-1/2}dyd\boldsymbol{z}$ holds, where $d\boldsymbol{z} = dz_1 dz_2 dz_3$. Thus, we obtain the following expressions:

$$I_0[\mathcal{G}] = \frac{\rho}{\pi^{3/2}\Gamma(\delta/2)} \iint_0^\infty y^{\delta/2-1} \exp(-|\boldsymbol{z}|^2 - y)dyd\boldsymbol{z} = \rho, \tag{A6a}$$

$$I_i[\mathcal{G}] - v_i I_0[\mathcal{G}] = \frac{\rho}{\pi^{3/2}\Gamma(\delta/2)} \sum_{j=1}^3 (2/\lambda^{(j)})^{1/2}(\mathsf{P})_{ij} \iint_0^\infty y^{\delta/2-1} z_j \exp(-|\boldsymbol{z}|^2 - y)dyd\boldsymbol{z} = 0, \tag{A6b}$$

$$I_4[\mathcal{G}] = \frac{\rho R T_{\text{rel}}}{\pi^{3/2}\Gamma(\delta/2)} \iint_0^\infty y^{\delta/2} \exp(-|\boldsymbol{z}|^2 - y)dyd\boldsymbol{z} = \rho\frac{\delta R T_{\text{rel}}}{2}, \tag{A6c}$$

$$I_{ij}[\mathcal{G}] - v_i v_j I_0[\mathcal{G}] = \frac{2\rho}{\pi^{3/2}\Gamma(\delta/2)} \sum_{k,l=1}^3 (\mathsf{P})_{ik}(\mathsf{P})_{jl}(\lambda^{(k)}\lambda^{(l)})^{-1/2} \iint_0^\infty y^{\delta/2-1} z_k z_l \exp(-|\boldsymbol{z}|^2 - y)dyd\boldsymbol{z}$$

$$= \rho \sum_{k,l=1}^{3} (\mathsf{P})_{ik}(\mathsf{P})_{jl}(\lambda^{(k)}\lambda^{(l)})^{-1/2}\delta_{kl} = \rho \sum_{k=1}^{3}(\lambda^{(k)})^{-1}(\mathsf{P})_{ik}(\mathsf{P})_{jk}. \tag{A6d}$$

Taking the inverse of ${}^{t}\mathsf{P}\mathsf{T}^{-1}\mathsf{P} = \mathrm{diag}\,[\lambda^{(1)}, \lambda^{(2)}, \lambda^{(3)}]$ and multiplying by P from the left and by ${}^{t}\mathsf{P}$ from the right, we have $\mathsf{T} = \mathsf{P}\,\mathrm{diag}\,[1/\lambda^{(1)}, 1/\lambda^{(2)}, 1/\lambda^{(3)}]\,{}^{t}\mathsf{P}$, or $(\mathsf{T})_{ij} = \sum_{k=1}^{3}(\lambda^{(k)})^{-1}(\mathsf{P})_{ik}(\mathsf{P})_{jk}$. Therefore, the last line of Eq. (A6d) becomes $\rho\,(\mathsf{T})_{ij}$.

In summary, we have the following expressions of the moments of the Gaussian:

$$I_0[\mathcal{G}] = \rho, \quad I_i[\mathcal{G}] = \rho v_i, \quad I_4[\mathcal{G}] = \rho\frac{\delta RT_{\mathrm{rel}}}{2}, \tag{A7a}$$

$$I_{ij}[\mathcal{G}] = \rho\,(\mathsf{T})_{ij} + \rho v_i v_j, \quad I_{kk}[\mathcal{G}] = 3(1-\theta)\rho RT_{\mathrm{tr}} + 3\theta\rho RT + \rho v_k^2, \tag{A7b}$$

$$\frac{1}{2}I_{kk}[\mathcal{G}] + I_4[\mathcal{G}] = \frac{3+\delta}{2}\rho RT + \frac{1}{2}\rho v_k^2. \tag{A7c}$$

2. Conservation laws

From Eqs. (6d)–(6j), the following relations hold:

$$I_0[f] = \rho, \quad I_i[f] = \rho v_i, \quad I_4[f] = \rho\frac{\delta RT_{\mathrm{int}}}{2}, \tag{A8a}$$

$$I_{ij}[f] = p_{ij} + \rho v_i v_j, \quad I_{kk}[f] = 3\rho RT_{\mathrm{tr}} + \rho v_k^2, \tag{A8b}$$

$$\frac{1}{2}I_{kk}[f] + I_4[f] = \frac{3+\delta}{2}\rho RT + \frac{1}{2}\rho v_k^2. \tag{A8c}$$

Equations (A7) and (A8) immediately show that Eq. (11) holds and verify the fact that $Q(f) = 0$ and $f = f_{\mathrm{eq}}$ are equivalent [see the paragraph containing Eq. (10)].

Multiplying Eq. (5) by 1, ξ_i, and $\xi_k^2/2 + \mathcal{E}$ and integrating the resulting equations with respect to $\mathcal{E}$ from 0 to ∞ and with respect to $\boldsymbol{\xi}$ over its whole space, we obtain, from Eq. (11), the following relations:

$$\frac{\partial}{\partial X_1}\iint_0^{\infty}\xi_1 f d\mathcal{E}d\boldsymbol{\xi} = \frac{\partial}{\partial X_1}(\rho v_1) = 0, \tag{A9a}$$

$$\frac{\partial}{\partial X_1}\iint_0^{\infty}\xi_1\xi_i f d\mathcal{E}d\boldsymbol{\xi} = \frac{\partial}{\partial X_1}(p_{1i} + \rho v_1 v_i) = 0, \tag{A9b}$$

$$\frac{\partial}{\partial X_1}\iint_0^{\infty}\xi_1\left(\frac{1}{2}\xi_k^2 + \mathcal{E}\right) f d\mathcal{E}d\boldsymbol{\xi} = \frac{\partial}{\partial X_1}\left[q_1 + p_{1k}v_k + v_1\left(\frac{3+\delta}{2}p + \frac{1}{2}\rho v_k^2\right)\right] = 0. \tag{A9c}$$

That is, we obtain the following conservation laws:

$$\rho v_1 = \mathrm{const}, \quad p_{1i} + \rho v_1 v_i = \mathrm{const}, \tag{A10a}$$

$$q_1 + p_{1k}v_k + v_1\left(\frac{3+\delta}{2}p + \frac{1}{2}\rho v_k^2\right) = \mathrm{const}. \tag{A10b}$$

If we apply these relations to the equilibrium states at the upstream and downstream infinities, we have

$$\rho_- v_- = \rho_+ v_+, \quad p_- + \rho_- v_-^2 = p_+ + \rho_+ v_+^2, \tag{A11a}$$

$$v_-\left(\frac{5+\delta}{2}p_- + \frac{1}{2}\rho_- v_-^2\right) = v_+\left(\frac{5+\delta}{2}p_+ + \frac{1}{2}\rho_+ v_+^2\right), \tag{A11b}$$

from which the Rankine-Hugoniot relations (2) follow.

3. Case of $\theta = 0$

In the case of $\theta = 0$, i.e., $\mu_b/\mu = \infty$, Eq. (6j) gives $T_{rel} = T_{int}$, so that Eqs. (6b) and (6c) reduce respectively to

$$\mathcal{G} = \frac{\rho \mathcal{E}^{\delta/2-1}}{(2\pi)^{3/2}[\det(\mathsf{T})]^{1/2}(RT_{int})^{\delta/2}\Gamma(\delta/2)} \exp\left(-\frac{1}{2}(\xi_i - v_i)(\mathsf{T}^{-1})_{ij}(\xi_j - v_j) - \frac{\mathcal{E}}{RT_{int}}\right), \quad \text{(A12a)}$$

$$(\mathsf{T})_{ij} = (1 - \nu)RT_{tr}\delta_{ij} + \nu p_{ij}/\rho. \quad \text{(A12b)}$$

In this case, it follows from Eqs. (A7a) and (A8a) that $I_4[\mathcal{G}] - I_4[f] = \iint_0^\infty \mathcal{E}(\mathcal{G} - f)d\mathcal{E}d\boldsymbol{\xi} = 0$. Therefore, the relation (11) is replaced by

$$\iint_0^\infty \phi_r Q(g)d\mathcal{E}d\boldsymbol{\xi} = 0, \quad \text{(A13)}$$

where ϕ_r ($r = 0, ..., 5$) are the new collision invariants, i.e.,

$$\phi_0 = 1, \quad \phi_i = \xi_i \ (i = 1, 2, 3), \quad \phi_4 = \tfrac{1}{2}|\boldsymbol{\xi}|^2, \quad \phi_5 = \mathcal{E}. \quad \text{(A14)}$$

Correspondingly, in place of Eq. (A10), the following four conservation laws hold:

$$\rho v_1 = \text{const}, \quad p_{1i} + \rho v_1 v_i = \text{const}, \quad \text{(A15a)}$$

$$(q_{tr})_1 + p_{1k}v_k + v_1\left(\frac{3}{2}\rho RT_{tr} + \frac{1}{2}\rho v_k^2\right) = \text{const}, \quad \text{(A15b)}$$

$$(q_{int})_1 + v_1\frac{\delta}{2}\rho RT_{int} = \text{const}, \quad \text{(A15c)}$$

where

$$(q_{tr})_i = \frac{1}{2}\iint_0^\infty (\xi_i - v_i)(\xi_k - v_k)^2 f d\mathcal{E}d\boldsymbol{\xi}, \quad \text{(A16a)}$$

$$(q_{int})_i = \iint_0^\infty (\xi_i - v_i)\mathcal{E} f d\mathcal{E}d\boldsymbol{\xi}. \quad \text{(A16b)}$$

In addition, it is easy to show that the local equilibrium distribution f_{eq} is given by

$$f_{eq} = \frac{\rho \mathcal{E}^{\delta/2-1}}{(2\pi RT_{tr})^{3/2}(RT_{int})^{\delta/2}\Gamma(\delta/2)} \exp\left(-\frac{|\boldsymbol{\xi} - \boldsymbol{v}|^2}{2RT_{tr}} - \frac{\mathcal{E}}{RT_{int}}\right), \quad \text{(A17)}$$

instead of Eq. (10).

The form of the local equilibrium distribution in Eq. (A17) indicates that the equilibrium state at upstream infinity is determined by specifying ρ_-, v_-, T_{tr-}, and T_{int-} and that at downstream infinity by specifying ρ_+, v_+, T_{tr+}, and T_{int+}, where T_{tr-} and T_{int-} are the translational and internal temperatures at upstream infinity, and T_{tr+} and T_{int+} are those at downstream infinity. That is, we can impose the following conditions at upstream and downstream infinities:

$$f = \frac{\rho_- \mathcal{E}^{\delta/2-1}}{(2\pi RT_{tr-})^{3/2}(RT_{int-})^{\delta/2}\Gamma(\delta/2)} \exp\left(-\frac{(\xi_1 - v_-)^2 + \xi_2^2 + \xi_3^2}{2RT_{tr-}} - \frac{\mathcal{E}}{RT_{int-}}\right), \quad (X_1 \to -\infty),$$

$$\text{(A18a)}$$

$$f = \frac{\rho_+ \mathcal{E}^{\delta/2-1}}{(2\pi RT_{tr+})^{3/2}(RT_{int+})^{\delta/2}\Gamma(\delta/2)} \exp\left(-\frac{(\xi_1 - v_+)^2 + \xi_2^2 + \xi_3^2}{2RT_{tr+}} - \frac{\mathcal{E}}{RT_{int+}}\right), \quad (X_1 \to \infty).$$

$$\text{(A18b)}$$

If we apply Eq. (A15) to upstream and downstream infinities, we have

$$\rho_- v_- = \rho_+ v_+, \quad \rho_- R T_{\text{tr}-} + \rho_- v_-^2 = \rho_+ R T_{\text{tr}+} + \rho_+ v_+^2, \quad \text{(A19a)}$$

$$v_- \left(\frac{5}{2} \rho_- R T_{\text{tr}-} + \frac{1}{2} \rho_- v_-^2 \right) = v_+ \left(\frac{5}{2} \rho_+ R T_{\text{tr}+} + \frac{1}{2} \rho_+ v_+^2 \right), \quad \text{(A19b)}$$

$$v_- \frac{\delta}{2} \rho_- R T_{\text{int}-} = v_+ \frac{\delta}{2} \rho_+ R T_{\text{int}+}. \quad \text{(A19c)}$$

The first and last equations show that $T_{\text{int}-} = T_{\text{int}+}$. On the other hand, Eqs. (A19a) and (A19b) are the same as Eqs. (A11a) and (A11b) with $\delta = 0$ (or $\gamma = 5/3$) if T_{tr} is regarded as the temperature T. Therefore, the Rankine-Hugoniot relations for $\theta = 0$ follow immediately from Eq. (2), that is,

$$\rho_+ = \frac{4 \widetilde{M}_-^2}{\widetilde{M}_-^2 + 3} \rho_-, \quad v_+ = \frac{\widetilde{M}_-^2 + 3}{4 \widetilde{M}_-^2} v_-, \quad \text{(A20a)}$$

$$T_{\text{tr}+} = \frac{(5 \widetilde{M}_-^2 - 1)(\widetilde{M}_-^2 + 3)}{16 \widetilde{M}_-^2} T_{\text{tr}-}, \quad T_{\text{int}+} = T_{\text{int}-}, \quad \text{(A20b)}$$

$$\widetilde{M}_+ = \left(\frac{\widetilde{M}_-^2 + 3}{5 \widetilde{M}_-^2 - 1} \right)^{1/2}, \quad \text{(A20c)}$$

where

$$\widetilde{M}_{\mp} = \frac{v_{\mp}}{\sqrt{5 R T_{\text{tr}\mp}/3}}. \quad \text{(A21)}$$

Here, $\widetilde{M}_-$ plays the role of the upstream Mach number, so that $\widetilde{M}_- > 1$ if there is a standing shock. It is noted that when $T_{\text{tr}-} = T_-$, $\widetilde{M}_- < M_-$ holds because $\widetilde{M}_-/M_- = \sqrt{3\gamma/5}$ and $\gamma < 5/3$.

APPENDIX B: SUPPLEMENTARY DATA FOR NUMERICAL ANALYSIS

Since the profiles of types A, B, and C are very different, we need different grid systems depending on the types of the profile. In particular, for type C, use should be made of a grid system in x_1 that concentrates inside the thin front layer and cover the wide range of the thick rear layer and one in ζ_1 that covers the high $\hat{T}_{\text{tr}}$ behind the thin front layer. Because the jump due to the thin front layer corresponds to the jump given by the Rankine-Hugoniot relations for $\mu_b/\mu = \infty$ (cf. Secs. IV D 2 and V A), we need to take into account the information about the downstream condition of this Rankine-Hugoniot relations in the grid systems. For this purpose, we use the dimensionless downstream density $\hat{\rho}_{**}$, velocity $\hat{v}_{**}$, and temperature $\hat{T}_{**}$ defined by Eq. (26).

1. Grid systems

For the x_1 coordinate, the range of which has been limited to $-D_n \leqslant x_1 \leqslant D_p$, we use the grid points $x_{(i)}$ concentrated near $x_1 = 0$ based on functions containing pth power and qth power of x_1, i.e.,

$$x_{(i)} = \frac{D_n}{1 + a} \left[\frac{i}{N_n} + a \left(\frac{i}{N_n} \right)^p \right], \quad x_{(-i)} = -x_{(i)}, \quad (i = 0, 1, \ldots, N_n), \quad \text{(B1a)}$$

$$x_{(i)} = D_n + \frac{D_p - D_n}{1 + b} \left[\frac{i - N_n}{N_p - N_n} + b \left(\frac{i - N_n}{N_p - N_n} \right)^q \right], \quad (i = N_n + 1, N_n + 2, \ldots, N_p). \quad \text{(B1b)}$$

This grid system is prepared to capture the type-C profile composed of a thin front layer with a sharp change and a thick rear layer with slow relaxation: Equation (B1a) is for the thin front layer, and

Eq. (B1b) is for the thick rear layer. With Eq. (B1), the grid interval $d_i = x_{(i)} - x_{(i-1)}$ becomes

$$d_1 \approx \frac{D_n}{(1+a)N_n}, \quad d_{N_n} \approx d_1(1+ap), \tag{B2a}$$

$$d_{N_n+1} \approx \frac{D_p - D_n}{(1+b)(N_p - N_n)}, \quad d_{N_p} \approx d_{N_n+1}(1+bq). \tag{B2b}$$

We first choose D_n and D_p ($>D_n$). For Eq. (B1a), we determine N_n and a based on the minimum interval d_1 and the ratio d_{N_n}/d_1 [Eq. (B2a)] and choose the growth rate p. For Eq. (B1b), we determine N_p and b based on the condition $d_{N_n+1} \approx d_{N_n}$ and the ratio d_{N_p}/d_{N_n+1} [Eq. (B2b)] and choose the growth rate q.

For the molecular velocity ζ_1, whose range has been limited to $-Z_n \leqslant \zeta_1 \leqslant Z_p$, we use the grid points that are suitable for the bimodal distribution based on the upstream equilibrium distribution (33a) centered at $\zeta_1 = \hat{v}_-$ and the downstream equilibrium distribution (33b) centered at $\zeta_1 = \hat{v}_+$ ($<\hat{v}_-$). More specifically, we use a uniform grid interval for $\hat{v}_+ \leqslant \zeta_1 \leqslant \hat{v}_-$ and nonuniform grid intervals suitable to describe the half-range distribution of Eq. (33a) [or Eq. (33b)] for $\hat{v}_- \leqslant \zeta_1 \leqslant Z_p$ (or $-Z_n \leqslant \zeta_1 \leqslant \hat{v}_+$). The explicit expression of the grid points $\zeta_{(j)}$ is as follows:

$$\zeta_{(j)} = \hat{v}_+ - \zeta^{**}_{(2M_n-j)}, \quad (j = 0, 1, \ldots, 2M_n), \tag{B3a}$$

$$\zeta_{(j)} = \hat{v}_+ + (\hat{v}_- - \hat{v}_+)\frac{j - 2M_n}{2M_0}, \quad (j = 2M_n + 1, \ldots, 2M_n + 2M_0), \tag{B3b}$$

$$\zeta_{(j)} = \hat{v}_- + \zeta^{*}_{(j-2M_n-2M_0)}, \quad (j = 2M_n + 2M_0 + 1, \ldots, 2M), \tag{B3c}$$

where $\zeta^{*}_{(j)}$ and $\zeta^{**}_{(j)}$ are auxiliary grid systems defined below. Equation (B3a) with $2M_n + 1$ grid points is for $-Z_n \leqslant \zeta_1 \leqslant \hat{v}_+$, Eq. (B3b) with $2M_0$ grid points is for $\hat{v}_+ \leqslant \zeta_1 \leqslant \hat{v}_-$, and Eq. (B3c) with $2M - 2(M_n + M_0)$ grid points is for $\hat{v}_- \leqslant \zeta_1 \leqslant Z_p$. The auxiliary system $\zeta^{*}_{(j)}$ is defined by

$$\zeta^{*}_{(j)} = \frac{Z}{1+c}\left[\frac{j}{2\widetilde{M}_p} + c\left(\frac{j}{2\widetilde{M}_p}\right)^r\right], \quad (j = 0, 1, \ldots, 2\widetilde{M}_p), \tag{B4}$$

with appropriate constants c, r, Z, and $\widetilde{M}_p$. This is a grid system for the right half of the shifted distribution, Eq. (33a) with $\hat{v}_- = 0$, in the limited interval $0 \leqslant \zeta_1 \leqslant Z$ and gives the grid interval $\delta^{*}_j = \zeta^{*}_{(j)} - \zeta^{*}_{(j-1)}$ as follows:

$$\delta^{*}_1 \approx \frac{Z}{2(1+c)\widetilde{M}_p}, \quad \delta^{*}_{2\widetilde{M}_p} \approx \delta^{*}_1(1+cr). \tag{B5}$$

We choose the number of the grid points in Eq. (B3c) [$2M - 2(M_n + M_0)$] larger than that in Eq. (B4), i.e., $M - (M_n + M_0) \geqslant \widetilde{M}_p$. The auxiliary system $\zeta^{**}_{(j)}$ is defined by

$$\zeta^{**}_{(j)} = \frac{Z\sqrt{\tau}}{1+c}\left[\frac{j}{2M_n} + c\left(\frac{j}{2M_n}\right)^r\right], \quad (j = 0, 1, \ldots, 2M_n), \tag{B6a}$$

$$\tau = \begin{cases} \max(\hat{T}_+, \hat{T}_{**}), & (\widetilde{M}_- > 1), \\ \hat{T}_+, & (\widetilde{M}_- \leqslant 1), \end{cases} \tag{B6b}$$

where M_n is chosen to be the minimum integer such that $M_n \geqslant \widetilde{M}_p\sqrt{\tau}$, and the constants c, r, and Z are common to $\zeta^{*}_{(j)}$. The $\hat{T}_{**}$ in Eq. (B6b) is the downstream value of $\hat{T}_{tr}$ for the shock wave with $\mu_b/\mu = \infty$, and $\widetilde{M}_-$ is the parameter playing the role of the upstream Mach number for such a shock wave [see Eq. (26b)]. This is basically a grid system for the right half of the shifted distribution, Eq. (33b) with $\hat{v}_+ = 0$, in the limited interval $0 \leqslant \zeta_1 \leqslant Z\sqrt{\hat{T}_+}$. However, to capture the possible significant overshoot of $\hat{T}_{tr}$ in type-C profiles, the choice of τ in Eq. (B6b) is introduced (note that

$\widetilde{M}_- > 1$ corresponds to type-C profile). This $\zeta_{(j)}^{**}$ is used in Eq. (B3a) after being reflected and shifted. We choose the number of grid points (i.e., M_n, M_0, and M) in such a way that the minimum and maximum of the grid intervals in $\zeta_{(j)}^*$ are more or less the same as those in $\zeta_{(j)}^{**}$ and that the uniform interval for $\hat{v}_+ \leqslant \zeta_1 \leqslant \hat{v}_-$ is approximately the same as the minimum interval in $\zeta_{(j)}^*$ (or $\zeta_{(j)}^{**}$).

2. Data for numerical analysis

a. Convergence of iteration

If the computation can be carried out without any error, the shock wave stops somewhere when the solution has converged. However, because of the small error in the practical computation, the shock wave exhibits a small shift at each iteration step even after the profile has converged. We obtain the numerical solution whose shift is small enough compared with the numerical error contained in the solution.

Let us define the location of the shock wave x_s by the point that satisfies

$$\hat{\rho}(x_s) = \begin{cases} (1 + \hat{\rho}_{**})/2, & (\widetilde{M}_- > 1, \text{ i.e., type C}), \\ 0.95 + 0.05\hat{\rho}_+, & (\widetilde{M}_- = 1,, \text{ i.e., type B}), \\ (1 + \hat{\rho}_+)/2, & (\widetilde{M}_- < 1, \text{ i.e., type A}), \end{cases} \tag{B7}$$

where the expression for $\widetilde{M}_- = 1$ is equivalent to $\check{\rho} = 0.05$. Let h stand for the macroscopic quantities $\hat{\rho}$, $\hat{v}_1$, $\hat{p}_{11}$, $\hat{p}_{22}$, $\hat{T}_{\text{tr}}$, and $\hat{T}_{\text{int}}$. If we denote the position of the shock wave at the nth iteration step by $x_s^{[n]}$ and the macroscopic quantities h at the grid point $x_{(i)}$ at the nth step by $h^{[n,i]}$, then the relative position of the grid point $x_{(i)}$ with respect to the shock location is $x_{(i)} - x_s^{[n]}$.

The convergence is judged by comparing, at each r steps, $h^{[kr,i]}$ and $h^{[(k-1)r,i]}$ ($k = 1, 2, \ldots$). In this process, we need to compare them at the points whose relative positions with respect to the shock location are the same. We first obtain $x_s^{[kr]}$ from $\hat{\rho}^{[kr,i]}$ by the spline interpolation, and $x_s^{[(k-1)r,i]}$ from $\hat{\rho}^{[(k-1)r,i]}$ by the same. Then, we interpolate $h^{[kr,i]}$ to obtain the value at the point $x_{(i)} - x_s^{[(k-1)r]} + x_s^{[kr]}$, which we denote by $\widetilde{h^{[kr,i]}}$, and compare it with $h^{[(k-1)r,i]}$. If the following inequality

$$\max_i \left| \frac{\widetilde{h^{[kr,i]}} - h^{[(k-1)r,i]}}{h_- - h_+} \right| < \epsilon, \quad (h = \hat{\rho}, \hat{v}_1, \hat{p}_{11}, \hat{p}_{22}, \hat{T}_{\text{tr}}, \hat{T}_{\text{int}}), \tag{B8}$$

holds with a given small ϵ, we judge that the solution has converged. Here, h_- and h_+ are the values of h at upstream infinity and downstream infinity, respectively.

If we judge that the convergence has been attained at the nth step, we shift the solution in such a way that $x_s^{[n]}$ becomes 0 and repeat the iteration process with the shifted solution as the initial condition until the convergence is attained. We repeat this process several times to obtain the solution that satisfies $x_s = 0$ within the error of the computation.

In all the computations, we have set $r = 10$ and $\epsilon = 10^{-8}$.

b. Data for grid systems in x_1

For the grid system in x_1 defined by Eq. (B1), the parameters a, p, b, and q were set to be $a = 3$, $p = 3$, $b = 1$, and $q = 2$ for all the computations. Then, the number of grid points N_p in the downstream side is determined by the range of computation D_n, the number of grid points N_n in the upstream side, and the range of computation D_p in the downstream side from the condition $d_{N_n+1} \approx d_{N_n}$.

Depending on M_-, we used the grid systems (M1) to (M4) in Table I. In (M1) and (M2), N_p increases with μ_b/μ (when μ_b/μ is finite), so that the minimum and maximum intervals are unchanged: In (M1), $N_p = 404$ ($\mu_b/\mu = 10$), 820 (100), and 5320 (1000), and $(d_1, d_{N_n}, d_{N_p}) \approx$ (0.050, 0.50, 1.5); and in (M2), $N_p = 404$ ($\mu_b/\mu = 10$), 920 (100), and 6320 (1000), and $(d_1, d_{N_n}, d_{N_p}) \approx$ (0.25, 2.5, 7.5). On the other hand, in (M4), $N_p = 520$ is kept constant, and the

TABLE I. Grid systems in x_1.

Grid system	M_- or $\widetilde{M}_-$	D_n	N_n	D_p
(M1)	$M_- = 5$	80	400	$\max(5\mu_b/\mu, 84)$[a]
(M2)	$M_- = 1.2$	400	400	$\max(30\mu_b/\mu, 420)$[b]
(M3)	$\widetilde{M}_- = 1$	$\max(400, 2\mu_b/\mu)$	400	$\max(40\mu_b/\mu, 420)$
(M4)	$M_- = 1.05$	$100\mu_b/\mu$	500	$120\mu_b/\mu$
(M1′)	$M_- = 5$	64	320	$\max(4\mu_b/\mu, 68)$
(M1″)	$M_- = 5$	80	320	$\max(5\mu_b/\mu, 84)$
(M2′)	$M_- = 1.2$	320	320	$\max(24\mu_b/\mu, 336)$
(M2″)	$M_- = 1.2$	400	320	$\max(30\mu_b/\mu, 420)$

[a]$D_p = 84$ for $\mu_b/\mu = \infty$.
[b]$D_p = 420$ for $\mu_b/\mu = \infty$.

grid intervals are proportional to μ_b/μ, so that $(d_1, d_{N_n}, d_{N_p}) \approx (0.050\mu_b/\mu, 0.50\mu_b/\mu, 1.5\mu_b/\mu)$. In (M3), the number of grid points as well as the grid intervals change with μ_b/μ: $N_p = 404$ and $(d_1, d_{N_n}, d_{N_p}) \approx (0.25, 2.5, 6.9)$ for $\mu_b/\mu = 10$, $N_p = 1120$ and $(d_1, d_{N_n}, d_{N_p}) \approx (0.25, 2.5, 7.5)$ for $\mu_b/\mu = 100$, and $N_p = 1920$ and $(d_1, d_{N_n}, d_{N_p}) \approx (0.0013\mu_b/\mu, 0.012\mu_b/\mu, 0.037\mu_b/\mu)$ for $\mu_b/\mu \geqslant 200$.

For $M_- = 5$ and 1.2, we also used systems (M1′) and (M2′) (Table I) in which the ranges of computation are 80% of those of (M1) and (M2), respectively, and systems (M1″) and (M2″) (Table I) in which the numbers of grid points are 80% of (M1) and (M2), respectively, for comparison.

c. Data for grid systems in ζ_1

The parameters c and r in the auxiliary system $\zeta_{(j)}^*$ [Eq. (B4)] and $\zeta_{(j)}^{**}$ [Eq. (B6)] were set to be $c = 3$ and $r = 3$ for all the computation. As described at the end of Appendix B 1, if we give the width Z and the number of grid points $\widetilde{M}_p$ in $\zeta_{(i)}^*$, M_0 and M_n are determined. We determine M from the condition

$$\zeta_{(2M)} \approx \max(\hat{v}_- + Z, \hat{v}_+ + Z\sqrt{\tau}), \tag{B9}$$

where τ is defined by Eq. (B6b). It should be noted that M_0, M_n, and M depend on δ and M_- as well as Z and $\widetilde{M}_p$.

We used the following two grid systems (Z1) and (Z2):

$$(\text{Z1})\ Z = 5, \quad \widetilde{M}_p = 50, \quad (\text{Z2})\ Z = 6, \quad \widetilde{M}_p = 150.$$

The system (Z1) is for $M_- = 5$ and (Z2) for $M_- \leqslant 1.2$. In Table II, we show the numbers of grid points M_n, M_0, and M together with the minimum and maximum values of the grid interval δ_j $(=\zeta_{(j)} - \zeta_{(j-1)})$ and those of $\zeta_{(j)}$ when the internal degrees of freedom $\delta = 4$.

For $M_- = 5$ and 1.2, we also used systems (Z1′) and (Z2′) in which the ranges of computation are 80% of those of (Z1) and (Z2), respectively, and systems (Z1″) and (Z2″) in which the numbers

TABLE II. Data for the grid system in ζ_1 when the internal degrees of freedom $\delta = 4$.

M_-	M_n	M_0	M	$(\delta_{2M_n+1}, \delta_{2M})$	$(\zeta_{(0)}, \zeta_{(2M)})$
5	132	135	332	(0.012, 0.20)	(−12.5, 13.9)
1.2	157	26	334	(0.0049, 0.050)	(−5.6, 7.1)
1.138... $(\widetilde{M}_- = 1)$	155	19	325	(0.0048, 0.050)	(−5.5, 7.0)
1.05	152	7	310	(0.0049, 0.050)	(−5.3, 6.9)

of grid points are 80% of (Z1) and (Z2), respectively, for comparison. That is,

$$(Z1') \, Z = 4, \quad \widetilde{M}_p = 40, \quad (Z1'') \, Z = 5, \quad \widetilde{M}_p = 40,$$
$$(Z2') \, Z = 4.8, \quad \widetilde{M}_p = 120, \quad (Z2'') \, Z = 6, \quad \widetilde{M}_p = 120.$$

3. Accuracy of computation

In this subsection, we denote by $h^{[i]}$ and $\phi_k^{[i,j]}$ the values of the macroscopic quantities h ($h = \hat{\rho}$, $\hat{v}_1$, $\hat{p}_{11}$, $\hat{p}_{22}$, $\hat{T}_{tr}$, $\hat{T}_{int}$, and their polynomials) and the marginal velocity distribution functions ϕ_k ($k = 1, 2, 3$) at the grid points after the solution has converged.

a. Comparison of the results based on different grid systems

We carried out computations with different grid systems for $M_- = 5$ and 1.2, $\delta = 4$, and $\mu_b/\mu = 10, 100$, and 1000 and confirmed that the results are close each other. We compare the reference result of a macroscopic quantity $h_*^{[i]}$ with the result based on a different grid system $h^{[i]}$. We first shift $h_*^{[i]}$ in such a way that its shock-wave location coincides with that of the solution $h^{[i]}$ and then interpolate $h_*^{[i]}$ at the grid points of $h^{[i]}$. Denoting the interpolated result by $h_*^{[i]}$ anew, we obtain the following D:

$$D = \max_h \left(\max_i \left| \frac{h^{[i]} - h_*^{[i]}}{h_- - h_+} \right| \right), \tag{B10}$$

where the maximum with respect to h means the maximum over the six macroscopic quantities $\hat{\rho}$, $\hat{v}_1$, $\hat{p}_{11}$, $\hat{p}_{22}$, $\hat{T}_{tr}$, and $\hat{T}_{int}$.

For $M_- = 5$, we regard the result based on (M1, Z1) as the reference solution and compare it with the results based on (M1′, Z1), (M1″, Z1), (M1, Z1′), and (M1, Z1″). The values of D are as follows: $D = 2.4 \times 10^{-5}$ for (M1′, Z1), 3.5×10^{-4} for (M1″, Z1), 8.3×10^{-5} for (M1, Z1′), and 7.0×10^{-6} for (M1, Z1″). For $M_- = 1.2$, we regard the result based on (M2, Z2) as the reference solution and compare it with the results based on (M2′, Z2), (M2″, Z2), (M2, Z2′), and (M2, Z2″). The values of D are as follows: $D = 2.9 \times 10^{-5}$ for (M2′, Z2), 4.8×10^{-5} for (M2″, Z2), 3.2×10^{-6} for (M2, Z2′), and 2.3×10^{-7} for (M2, Z2″).

b. Conservation laws and others

In order to check the conservation laws, we compute the following C_1, C_2, and C_3:

$$C_1 = \max_i |[(\hat{\rho}\hat{v}_1)^{[i]} - \hat{v}_-]/\hat{v}_-|,$$
$$C_2 = \max_i \left| \left[(\hat{p}_{11} + 2\hat{\rho}\hat{v}_1^2)^{[i]} - (1 + 2\hat{v}_-^2) \right] / (1 + 2\hat{v}_-^2) \right|,$$
$$C_3 = \max_i |(\hat{e}^{[i]} - \hat{e}_-)/\hat{e}_-|, \tag{B11}$$

where

$$\hat{e} = \hat{q}_1 + \hat{p}_{11}\hat{v}_1 + \hat{v}_1 \left(\frac{3+\delta}{2}\hat{p} + \hat{\rho}\hat{v}_1^2 \right), \quad \hat{e}_- = \hat{v}_- \left(\frac{5+\delta}{2} + \hat{v}_-^2 \right),$$

and let $C = \max(C_1, C_2, C_3)$.

Next, as a measure of the closeness of the solution to the equilibrium values at the edges of the ranges of the computation in x_1, we compute the following D_- and D_+:

$$D_- = \max_h \left(\max_{-D_n \leqslant x_{(i)} \leqslant -0.95D_n} |(h^{[i]} - h_-)/(h_+ - h_-)| \right),$$
$$D_+ = \max_h \left(\max_{0.95D_p \leqslant x_{(i)} \leqslant D_p} |(h^{[i]} - h_+)/(h_+ - h_-)| \right). \tag{B12}$$

Here, the maximum with respect to h is the same as in Eq. (B10).

The maximum values of C, D_-, and D_+ over the all computations (for all computations for different μ_b/μ and δ) are as follows: $(C, D_-, D_+) = (3.6 \times 10^{-5}, 1.6 \times 10^{-7}, 4.8 \times 10^{-5})$ for $M_- = 5$; $(C, D_-, D_+) = (9.2 \times 10^{-6}, 3.4 \times 10^{-8}, 2.2 \times 10^{-5})$ for $M_- = 1.2$; $(C, D_-, D_+) = (2.8 \times 10^{-6}, 2.9 \times 10^{-6}, 2.8 \times 10^{-5})$ for $\widetilde{M}_- = 1$; and $(C, D_-, D_+) = (2.1 \times 10^{-6}, 8.1 \times 10^{-6}, 5.8 \times 10^{-5})$ for $M_- = 1.05$.

Finally, we show the magnitude of the marginal velocity distribution function ϕ_k ($k = 1, 2, 3$) at the edges of the computational range in ζ_1. Let D_ζ denote

$$D_\zeta = \max_{k,i} \left(\left| \phi_k^{[i,0]} \right|, \left| \phi_k^{[i,2M]} \right| \right). \tag{B13}$$

For $M_- = 5$, $D_\zeta = 4.2 \times 10^{-10}$ [except (Z1')] and 8.4×10^{-7} [(Z1')]; for $M_- = 1.2$, $D_\zeta = 1.1 \times 10^{-15}$ [except (Z2')] and 2.2×10^{-10} [(Z2')]; and for $\widetilde{M}_- = 1$ and $M_- = 1.05$, $D_\zeta < 7.1 \times 10^{-16}$.

APPENDIX C: DERIVATION OF THE MACROSCOPIC EQUATIONS

In this Appendix, we consider the case of large ratio μ_b/μ (or small θ) and obtain the slowly varying solution of Eq. (16) whose length scale of variation is of the order of $1/\theta$. Although our original problem is spatially one dimensional, we consider the more general spatially three-dimensional case where $f = f(X_i, \xi_i, \mathcal{E})$ or $\hat{f} = \hat{f}(x_i, \zeta_i, \hat{\mathcal{E}})$ on the basis of the ES model,

$$\zeta_i \frac{\partial \hat{f}}{\partial x_i} = \frac{2}{\sqrt{\pi}} \hat{Q}(\hat{f}), \tag{C1}$$

in place of Eq. (16). In this case, the parameters ρ_-, T_-, and p_- in Eq. (15) should be interpreted as the reference density, temperature, and pressure, and Eqs. (17)–(19) are valid as they stand.

1. Hilbert expansion

Let us introduce a new space coordinates $y_i = (2/\sqrt{\pi})\theta x_i$ whose length scale of variation is of $O(1/\theta)$. Then, Eq. (C1) becomes

$$\theta \zeta_i \frac{\partial \hat{f}}{\partial y_i} = \hat{A}_c(\hat{T})\hat{\rho}(\hat{\mathcal{G}} - \hat{f}). \tag{C2}$$

Assuming that $\theta \ll 1$, we expand $\hat{f}$ as a power series in θ:

$$\hat{f} = \hat{f}^{(0)} + \hat{f}^{(1)}\theta + \hat{f}^{(2)}\theta^2 + \cdots. \tag{C3}$$

Correspondingly, the macroscopic quantities $\hat{\rho}$, $\hat{v}_i$, $\hat{p}_{ij}$, ..., which are represented by $\hat{h}$, are expanded as

$$\hat{h} = \hat{h}^{(0)} + \hat{h}^{(1)}\theta + \hat{h}^{(2)}\theta^2 + \cdots. \tag{C4}$$

The expressions of $\hat{h}^{(k)}$ ($k = 0, 1, ...$) in terms of $\hat{f}^{(l)}$ ($l = 0, 1, ...$) are obtained by a straightforward calculation in the following form:

$$\hat{\rho}^{(k)} = \iint\int_0^\infty \hat{f}^{(k)} d\hat{\mathcal{E}} d\boldsymbol{\zeta} \quad (k = 0, 1, 2, \ldots), \tag{C5}$$

$$\hat{\rho}^{(0)}\hat{v}_i^{(0)} = \iint\int_0^\infty \zeta_i \hat{f}^{(0)} d\hat{\mathcal{E}} d\boldsymbol{\zeta}, \quad \hat{\rho}^{(0)}\hat{v}_i^{(1)} = \iint\int_0^\infty \zeta_i \hat{f}^{(1)} d\hat{\mathcal{E}} d\boldsymbol{\zeta} - \hat{\rho}^{(1)}\hat{v}_i^{(0)}, \quad \ldots, \tag{C6}$$

$$\hat{p}_{ij}^{(0)} = 2\iint\int_0^\infty \left(\zeta_i - \hat{v}_i^{(0)} \right)\left(\zeta_j - \hat{v}_j^{(0)} \right) \hat{f}^{(0)} d\hat{\mathcal{E}} d\boldsymbol{\zeta}, \tag{C7a}$$

$$\hat{p}_{ij}^{(1)} = 2\iint\int_0^\infty \left(\zeta_i - \hat{v}_i^{(0)} \right)\left(\zeta_j - \hat{v}_j^{(0)} \right) \hat{f}^{(1)} d\hat{\mathcal{E}} d\boldsymbol{\zeta}, \quad \ldots, \tag{C7b}$$

$$\hat{\rho}^{(0)}\hat{T}_{\text{tr}}^{(0)} = \left(\hat{p}_{11}^{(0)} + \hat{p}_{22}^{(0)} + \hat{p}_{33}^{(0)}\right)/3, \quad \hat{\rho}^{(0)}\hat{T}_{\text{tr}}^{(1)} = \left(\hat{p}_{11}^{(1)} + \hat{p}_{22}^{(1)} + \hat{p}_{33}^{(1)}\right)/3 - \hat{\rho}^{(1)}\hat{T}_{\text{tr}}^{(0)}, \quad \ldots, \quad \text{(C8)}$$

$$\hat{\rho}^{(0)}\hat{T}_{\text{int}}^{(0)} = \frac{2}{\delta}\iint_0^{\infty}\hat{\mathcal{E}}\hat{f}^{(0)}d\hat{\mathcal{E}}d\boldsymbol{\zeta}, \quad \hat{\rho}^{(0)}\hat{T}_{\text{int}}^{(1)} = \frac{2}{\delta}\iint_0^{\infty}\hat{\mathcal{E}}\hat{f}^{(1)}d\hat{\mathcal{E}}d\boldsymbol{\zeta} - \hat{\rho}^{(1)}\hat{T}_{\text{int}}^{(0)}, \quad \ldots, \quad \text{(C9)}$$

$$\hat{T}^{(k)} = \frac{3\hat{T}_{\text{tr}}^{(k)} + \delta\hat{T}_{\text{int}}^{(k)}}{3+\delta}, \quad (k = 0, 1, 2, \ldots), \quad \text{(C10)}$$

$$\hat{T}_{\text{rel}}^{(0)} = \hat{T}_{\text{int}}^{(0)}, \quad \text{(C11a)}$$

$$\hat{T}_{\text{rel}}^{(k)} = \hat{T}_{\text{int}}^{(k)} + \left(\hat{T}^{(k-1)} - \hat{T}_{\text{int}}^{(k-1)}\right) = \hat{T}_{\text{int}}^{(k)} + \frac{3}{3+\delta}\left(\hat{T}_{\text{tr}}^{(k-1)} - \hat{T}_{\text{int}}^{(k-1)}\right), \quad (k = 1, 2, \ldots). \quad \text{(C11b)}$$

Consequently, $\hat{A}_c(\hat{T})$ and $\hat{\mathcal{G}}$ are also expanded, i.e.,

$$\hat{A}_c(\hat{T}) = \hat{A}_c^{(0)} + \hat{A}_c^{(1)}\theta + \hat{A}_c^{(2)}\theta^2 + \cdots, \quad \text{(C12a)}$$

$$\hat{\mathcal{G}} = \hat{\mathcal{G}}^{(0)} + \hat{\mathcal{G}}^{(1)}\theta + \hat{\mathcal{G}}^{(2)}\theta^2 + \cdots. \quad \text{(C12b)}$$

Here

$$\hat{A}_c^{(0)} = (\hat{A}_c)_{\theta=0} = \hat{A}_c(\hat{T}^{(0)}), \quad \text{(C13a)}$$

$$\hat{A}_c^{(1)} = \left(\frac{d\hat{A}_c}{d\theta}\right)_{\theta=0} = \left(\frac{d\hat{A}_c}{d\hat{T}}\frac{d\hat{T}}{d\theta}\right)_{\theta=0} = \left(\frac{d\hat{A}_c}{d\hat{T}}\right)_{\hat{T}=\hat{T}^{(0)}}\hat{T}^{(1)}, \quad \ldots, \quad \text{(C13b)}$$

$$\hat{\mathcal{G}}^{(0)} = \hat{\mathcal{G}}|_{\theta=0}$$
$$= \frac{\hat{\rho}^{(0)}\hat{\mathcal{E}}^{\delta/2-1}}{\pi^{3/2}([\det(\hat{\mathsf{T}})]^{(0)})^{1/2}\left(\hat{T}_{\text{rel}}^{(0)}\right)^{\delta/2}\Gamma(\delta/2)}\exp\left(-(\zeta_i - \hat{v}_i^{(0)})(\hat{\mathsf{T}}^{-1})_{ij}^{(0)}(\zeta_j - \hat{v}_j^{(0)}) - \frac{\hat{\mathcal{E}}}{\hat{T}_{\text{rel}}^{(0)}}\right), \quad \text{(C13c)}$$

$$\hat{\mathcal{G}}^{(1)} = \left(\frac{d\hat{\mathcal{G}}}{d\theta}\right)_{\theta=0} = \left(\hat{\mathcal{G}}\frac{d\ln\hat{\mathcal{G}}}{d\theta}\right)_{\theta=0} = \hat{\mathcal{G}}^{(0)}\Psi^{(1)}, \quad \ldots, \quad \text{(C13d)}$$

where

$$\Psi^{(1)} = \frac{\hat{\rho}^{(1)}}{\hat{\rho}^{(0)}} - \frac{1}{2}\frac{[\det(\hat{\mathsf{T}})]^{(1)}}{[\det(\hat{\mathsf{T}})]^{(0)}} + \frac{\hat{T}_{\text{rel}}^{(1)}}{\hat{T}_{\text{rel}}^{(0)}}\left(\frac{\hat{\mathcal{E}}}{\hat{T}_{\text{rel}}^{(0)}} - \frac{\delta}{2}\right) - (\zeta_i - \hat{v}_i^{(0)})(\hat{\mathsf{T}}^{-1})_{ij}^{(1)}(\zeta_j - \hat{v}_j^{(0)})$$
$$+ \hat{v}_i^{(1)}(\hat{\mathsf{T}}^{-1})_{ij}^{(0)}(\zeta_j - \hat{v}_j^{(0)}) + (\zeta_i - \hat{v}_i^{(0)})(\hat{\mathsf{T}}^{-1})_{ij}^{(0)}\hat{v}_j^{(1)}. \quad \text{(C14)}$$

In Eqs. (C13c) and (C14), $\hat{\mathsf{T}}^{(k)}$, $(\hat{\mathsf{T}}^{-1})^{(k)}$, and $[\det(\hat{\mathsf{T}})]^{(k)}$ ($k = 0$ and 1) are the coefficients of the expansions of $\hat{\mathsf{T}}$, $\hat{\mathsf{T}}^{-1}$, and $\det(\hat{\mathsf{T}})$:

$$\hat{\mathsf{T}} = \hat{\mathsf{T}}^{(0)} + \hat{\mathsf{T}}^{(1)}\theta + \cdots, \quad \text{(C15a)}$$

$$\hat{\mathsf{T}}^{-1} = (\hat{\mathsf{T}}^{-1})^{(0)} + (\hat{\mathsf{T}}^{-1})^{(1)}\theta + \cdots, \quad \text{(C15b)}$$

$$\det(\hat{\mathsf{T}}) = [\det(\hat{\mathsf{T}})]^{(0)} + [\det(\hat{\mathsf{T}})]^{(1)}\theta + \cdots, \quad \text{(C15c)}$$

and are obtained as follows.

Let us write the (i, j) component of $\hat{\mathsf{T}}$ as

$$(\hat{\mathsf{T}})_{ij} = (1 - \theta)\Lambda_{ij} + \theta\hat{T}\delta_{ij}, \quad \Lambda_{ij} = (1 - \nu)\hat{T}_{\text{tr}}\delta_{ij} + \nu\hat{p}_{ij}/\hat{\rho}. \quad \text{(C16)}$$

Since Λ_{ij} is expanded as

$$\Lambda_{ij} = \Lambda_{ij}^{(0)} + \Lambda_{ij}^{(1)}\theta + \cdots, \quad \text{(C17)}$$

with

$$\Lambda_{ij}^{(0)} = (1 - \nu)\hat{T}_{\mathrm{tr}}^{(0)}\delta_{ij} + \nu \hat{p}_{ij}^{(0)}/\hat{\rho}^{(0)}, \tag{C18a}$$

$$\Lambda_{ij}^{(1)} = (1 - \nu)\hat{T}_{\mathrm{tr}}^{(1)}\delta_{ij} + \nu\big(\hat{p}_{ij}^{(1)} - \hat{\rho}^{(1)}\hat{p}_{ij}^{(0)}/\hat{\rho}^{(0)}\big)/\hat{\rho}^{(0)}, \quad \ldots, \tag{C18b}$$

the (i, j) components of the coefficients of the expansion of $\hat{\mathsf{T}}$ [Eq. (C15a)] are obtained as follows:

$$(\hat{\mathsf{T}}^{(0)})_{ij} = \Lambda_{ij}^{(0)}, \quad (\hat{\mathsf{T}}^{(k)})_{ij} = \Lambda_{ij}^{(k)} + \big(\hat{T}^{(k-1)}\delta_{ij} - \Lambda_{ij}^{(k-1)}\big), \quad (k = 1, 2, \ldots). \tag{C19}$$

Next, we consider the relation $\hat{\mathsf{T}}\hat{\mathsf{T}}^{-1} = \mathsf{E}$, where E is the 3×3 unit matrix. Substituting the expansions of $\hat{\mathsf{T}}$ and $\hat{\mathsf{T}}^{-1}$ [Eqs. (C15a) and (C15b)] into this relation, we immediately have

$$\hat{\mathsf{T}}^{(0)}(\hat{\mathsf{T}}^{-1})^{(0)} = \mathsf{E}, \quad \hat{\mathsf{T}}^{(0)}(\hat{\mathsf{T}}^{-1})^{(1)} + \hat{\mathsf{T}}^{(1)}(\hat{\mathsf{T}}^{-1})^{(0)} = \mathsf{O}, \quad \ldots, \tag{C20}$$

where O is the 3×3 zero matrix. That is, we have the following relations:

$$(\hat{\mathsf{T}}^{-1})^{(0)} = (\hat{\mathsf{T}}^{(0)})^{-1}, \quad (\hat{\mathsf{T}}^{-1})^{(1)} = -(\hat{\mathsf{T}}^{(0)})^{-1}\hat{\mathsf{T}}^{(1)}(\hat{\mathsf{T}}^{(0)})^{-1}, \quad \ldots. \tag{C21}$$

Finally, the coefficients of the expansion of $\det(\hat{\mathsf{T}})$ [Eq. (C15c)] can be obtained as follows:

$$[\det(\hat{\mathsf{T}})]^{(0)} = \det(\hat{\mathsf{T}})|_{\theta=0} = \det(\hat{\mathsf{T}}^{(0)}), \tag{C22a}$$

$$\begin{aligned}
[\det(\hat{\mathsf{T}})]^{(1)} &= \frac{d\det(\hat{\mathsf{T}})}{d\theta}\bigg|_{\theta=0} \\
&= \det\begin{bmatrix} (\hat{\mathsf{T}}^{(1)})_{11} & (\hat{\mathsf{T}}^{(0)})_{12} & (\hat{\mathsf{T}}^{(0)})_{13} \\ (\hat{\mathsf{T}}^{(1)})_{21} & (\hat{\mathsf{T}}^{(0)})_{22} & (\hat{\mathsf{T}}^{(0)})_{23} \\ (\hat{\mathsf{T}}^{(1)})_{31} & (\hat{\mathsf{T}}^{(0)})_{32} & (\hat{\mathsf{T}}^{(0)})_{33} \end{bmatrix} + \det\begin{bmatrix} (\hat{\mathsf{T}}^{(0)})_{11} & (\hat{\mathsf{T}}^{(1)})_{12} & (\hat{\mathsf{T}}^{(0)})_{13} \\ (\hat{\mathsf{T}}^{(0)})_{21} & (\hat{\mathsf{T}}^{(1)})_{22} & (\hat{\mathsf{T}}^{(0)})_{23} \\ (\hat{\mathsf{T}}^{(0)})_{31} & (\hat{\mathsf{T}}^{(1)})_{32} & (\hat{\mathsf{T}}^{(0)})_{33} \end{bmatrix} \\
&\quad + \det\begin{bmatrix} (\hat{\mathsf{T}}^{(0)})_{11} & (\hat{\mathsf{T}}^{(0)})_{12} & (\hat{\mathsf{T}}^{(1)})_{13} \\ (\hat{\mathsf{T}}^{(0)})_{21} & (\hat{\mathsf{T}}^{(0)})_{22} & (\hat{\mathsf{T}}^{(1)})_{23} \\ (\hat{\mathsf{T}}^{(0)})_{31} & (\hat{\mathsf{T}}^{(0)})_{32} & (\hat{\mathsf{T}}^{(1)})_{33} \end{bmatrix},
\end{aligned}$$

$$\ldots. \tag{C22b}$$

If we use Eqs. (C3), (C4), and (C12) in Eq. (C2) and equate the terms of the same power of θ, we obtain

$$\hat{f}^{(0)} = \hat{\mathcal{G}}^{(0)}, \tag{C23a}$$

$$\hat{f}^{(1)} = \hat{\mathcal{G}}^{(1)} - \frac{1}{\hat{A}_c^{(0)}\hat{\rho}^{(0)}}\zeta_i\frac{\partial \hat{f}^{(0)}}{\partial y_i}, \tag{C23b}$$

$$\ldots.$$

Equations (C23a) and (C23b) are, respectively, the integral equations for $\hat{f}^{(0)}$ and $\hat{f}^{(1)}$. The conservation property (21) indicates that

$$\iint_0^\infty \hat{\varphi}_r(\hat{\mathcal{G}}^{(n)} - \hat{f}^{(n)})d\hat{\mathcal{E}}d\boldsymbol{\zeta} = 0, \quad (n = 0, 1, 2, \ldots), \tag{C24}$$

holds, where $\hat{\varphi}_r$ ($r = 0, \ldots, 4$) are the dimensionless collision invariants given in Eq. (22). Equation (C24) with $n = 1$ gives the compatibility condition of Eq. (C23b), i.e.,

$$\iint_0^\infty \begin{pmatrix} \zeta_j \\ \zeta_i\zeta_j \\ (\zeta_k^2 + \hat{\mathcal{E}})\zeta_j \end{pmatrix} \frac{\partial \hat{f}^{(0)}}{\partial y_j}d\hat{\mathcal{E}}d\boldsymbol{\zeta} = 0. \tag{C25}$$

a. Zeroth-order solution

Equations (C13c) and (C23a) and the relations $\hat{T}_{\text{rel}}^{(0)} = \hat{T}_{\text{int}}^{(0)}$ [Eq. (C11a)], $(\hat{T}^{-1})^{(0)} = (\hat{T}^{(0)})^{-1}$ [Eq. (C21)], and $[\det(\hat{T})]^{(0)} = \det(\hat{T}^{(0)})$ [Eq. (C22a)] give the following $\hat{f}^{(0)}$:

$$\hat{f}^{(0)} = \frac{\hat{\rho}^{(0)}\hat{\mathcal{E}}^{\delta/2-1}}{\pi^{3/2}[\det(\hat{T}^{(0)})]^{1/2}\left(\hat{T}_{\text{int}}^{(0)}\right)^{\delta/2}\Gamma(\delta/2)}\exp\left(-\left(\zeta_i - \hat{v}_i^{(0)}\right)[(\hat{T}^{(0)})^{-1}]_{ij}\left(\zeta_j - \hat{v}_j^{(0)}\right) - \frac{\hat{\mathcal{E}}}{\hat{T}_{\text{int}}^{(0)}}\right).\tag{C26}$$

If we calculate $\hat{p}_{ij}^{(0)}$ using Eqs. (C26) and (C7a), we have

$$\hat{p}_{ij}^{(0)} = \hat{\rho}^{(0)}(\hat{T}^{(0)})_{ij} = (1-\nu)\hat{\rho}^{(0)}\hat{T}_{\text{tr}}^{(0)}\delta_{ij} + \nu\hat{p}_{ij}^{(0)}.\tag{C27}$$

Since $\nu \neq 1$, we obtain

$$\hat{p}_{ij}^{(0)} = \hat{\rho}^{(0)}\hat{T}_{\text{tr}}^{(0)}\delta_{ij}.\tag{C28}$$

In consequence, we obtain the following $(\hat{T}^{(0)})_{ij}$ and thus $\hat{f}^{(0)}$:

$$(\hat{T}^{(0)})_{ij} = \hat{T}_{\text{tr}}^{(0)}\delta_{ij},\tag{C29}$$

$$\hat{f}^{(0)} = \frac{\hat{\rho}^{(0)}\hat{\mathcal{E}}^{\delta/2-1}}{\left(\pi\hat{T}_{\text{tr}}^{(0)}\right)^{3/2}\left(\hat{T}_{\text{int}}^{(0)}\right)^{\delta/2}\Gamma(\delta/2)}\exp\left(-\frac{\left(\zeta_k - \hat{v}_k^{(0)}\right)^2}{\hat{T}_{\text{tr}}^{(0)}} - \frac{\hat{\mathcal{E}}}{\hat{T}_{\text{int}}^{(0)}}\right).\tag{C30}$$

Here, $\hat{\rho}^{(0)}$, $\hat{v}_i^{(0)}$, $\hat{T}_{\text{tr}}^{(0)}$, and $\hat{T}_{\text{int}}^{(0)}$ are unknown functions, the equation for which will be derived in Appendix C 2. Equation (C30) is the dimensionless local equilibrium distribution for $\theta = 0$ [cf. Eq. (A17)].

b. First-order solution

From Eq. (C23b), the first-order solution is expressed as

$$\hat{f}^{(1)} = \hat{f}^{(0)}\Psi^{(1)} - \frac{1}{\hat{A}_c^{(0)}\hat{\rho}^{(0)}}\zeta_i\frac{\partial\hat{f}^{(0)}}{\partial y_i}.\tag{C31}$$

From the zeroth-order result and Eqs. (C19), (C21), and (C22b), we have the following expressions:

$$(\hat{T}^{(1)})_{ij} = \left[\hat{T}_{\text{tr}}^{(1)} + \left(\hat{T}^{(0)} - \hat{T}_{\text{tr}}^{(0)}\right)\right]\delta_{ij} + \nu\frac{1}{\hat{\rho}^{(0)}}\left(\hat{p}_{ij}^{(1)} - \frac{1}{3}\hat{p}_{kk}^{(1)}\delta_{ij}\right),\tag{C32a}$$

$$(\hat{T}^{-1})^{(1)} = -\frac{1}{\left(\hat{T}_{\text{tr}}^{(0)}\right)^2}\hat{T}^{(1)}, \quad [\det(\hat{T})]^{(1)} = \left(\hat{T}_{\text{tr}}^{(0)}\right)^2\text{tr}(\hat{T}^{(1)}),\tag{C32b}$$

where $\text{tr}(\hat{T}^{(1)})$ indicates the trace of $\hat{T}^{(1)}$. With these relations, $\Psi^{(1)}$ in Eq. (C14) is transformed into the following form:

$$\begin{aligned}\Psi^{(1)} &= \frac{\hat{\rho}^{(1)}}{\hat{\rho}^{(0)}} - \frac{\text{tr}(\hat{T}^{(1)})}{2\hat{T}_{\text{tr}}^{(0)}} + \frac{\hat{T}_{\text{rel}}^{(1)}}{\hat{T}_{\text{int}}^{(0)}}\left(\frac{\hat{\mathcal{E}}}{\hat{T}_{\text{int}}^{(0)}} - \frac{\delta}{2}\right) + (\hat{T}^{(1)})_{ij}\frac{\left(\zeta_i - \hat{v}_i^{(0)}\right)\left(\zeta_j - \hat{v}_j^{(0)}\right)}{\left(\hat{T}_{\text{tr}}^{(0)}\right)^2} + 2\frac{\left(\zeta_j - \hat{v}_j^{(0)}\right)\hat{v}_j^{(1)}}{\hat{T}_{\text{tr}}^{(0)}}\\ &= \frac{\hat{\rho}^{(1)}}{\hat{\rho}^{(0)}} + 2\frac{\left(\zeta_j - \hat{v}_j^{(0)}\right)\hat{v}_j^{(1)}}{\hat{T}_{\text{tr}}^{(0)}} + \frac{\text{tr}(\hat{T}^{(1)})}{3\hat{T}_{\text{tr}}^{(0)}}\left[\frac{\left(\zeta_k - \hat{v}_k^{(0)}\right)^2}{\hat{T}_{\text{tr}}^{(0)}} - \frac{3}{2}\right] + \frac{\hat{T}_{\text{rel}}^{(1)}}{\hat{T}_{\text{int}}^{(0)}}\left(\frac{\hat{\mathcal{E}}}{\hat{T}_{\text{int}}^{(0)}} - \frac{\delta}{2}\right)\\ &\quad + \left[(\hat{T}^{(1)})_{ij} - \frac{1}{3}\text{tr}(\hat{T}^{(1)})\delta_{ij}\right]\frac{\left(\zeta_i - \hat{v}_i^{(0)}\right)\left(\zeta_j - \hat{v}_j^{(0)}\right)}{\left(\hat{T}_{\text{tr}}^{(0)}\right)^2}\end{aligned}$$

$$= \frac{\hat{\rho}^{(1)}}{\hat{\rho}^{(0)}} + 2\frac{\left(\zeta_j - \hat{v}_j^{(0)}\right)\hat{v}_j^{(1)}}{\hat{T}_{\text{tr}}^{(0)}} + \frac{1}{\hat{T}_{\text{tr}}^{(0)}}\left[\hat{T}_{\text{tr}}^{(1)} + \left(\hat{T}^{(0)} - \hat{T}_{\text{tr}}^{(0)}\right)\right]\left[\frac{\left(\zeta_k - \hat{v}_k^{(0)}\right)^2}{\hat{T}_{\text{tr}}^{(0)}} - \frac{3}{2}\right]$$

$$+ \frac{1}{\hat{T}_{\text{int}}^{(0)}}\left[\hat{T}_{\text{int}}^{(1)} + \left(\hat{T}^{(0)} - \hat{T}_{\text{int}}^{(0)}\right)\right]\left(\frac{\hat{\mathcal{E}}}{\hat{T}_{\text{int}}^{(0)}} - \frac{\delta}{2}\right)$$

$$+ \nu\frac{1}{\hat{\rho}^{(0)}\hat{T}_{\text{tr}}^{(0)}}\left(\hat{p}_{ij}^{(1)} - \frac{1}{3}\hat{p}_{kk}^{(1)}\delta_{ij}\right)\frac{\left(\zeta_i - \hat{v}_i^{(0)}\right)\left(\zeta_j - \hat{v}_j^{(0)}\right)}{\hat{T}_{\text{tr}}^{(0)}}. \tag{C33}$$

2. Macroscopic equations

By using Eq. (C30) in the compatibility condition (C25), we obtain the following five equations containing six functions $\hat{\rho}^{(0)}$, $\hat{v}_j^{(0)}$, $\hat{T}_{\text{tr}}^{(0)}$, and $\hat{T}_{\text{int}}^{(0)}$:

$$\frac{\partial}{\partial y_j}\left(\hat{\rho}^{(0)}\hat{v}_j^{(0)}\right) = 0, \tag{C34a}$$

$$\frac{\partial}{\partial y_j}\left(\frac{1}{2}\hat{\rho}^{(0)}\hat{T}_{\text{tr}}^{(0)}\delta_{ij} + \hat{\rho}^{(0)}\hat{v}_i^{(0)}\hat{v}_j^{(0)}\right) = 0, \tag{C34b}$$

$$\frac{\partial}{\partial y_j}\left[\hat{\rho}^{(0)}\hat{v}_j^{(0)}\left(\hat{v}_k^{(0)}\right)^2 + \hat{\rho}^{(0)}\hat{v}_j^{(0)}\frac{5\hat{T}_{\text{tr}}^{(0)} + \delta\hat{T}_{\text{int}}^{(0)}}{2}\right] = 0. \tag{C34c}$$

Therefore, we need one more equation to close the system, which will be obtained in the following process.

In addition to the zeroth-order variables $\hat{\rho}^{(0)}$, $\hat{v}_j^{(0)}$, $\hat{T}_{\text{tr}}^{(0)}$, and $\hat{T}_{\text{int}}^{(0)}$, the first-order solution $\hat{f}^{(1)}$ contains the first-order variables $\hat{\rho}^{(1)}$, $\hat{v}_i^{(1)}$, $\hat{p}_{ij}^{(1)}$, $\hat{T}_{\text{tr}}^{(1)}$, and $\hat{T}_{\text{int}}^{(1)}$. If we calculate $\hat{\rho}^{(1)}$ and $\hat{v}_i^{(1)}$ using Eqs. (C31), (C33), (C5), and (C6) and taking Eq. (C25) into account, we obtain the trivial result, i.e., $\hat{\rho}^{(1)} = \hat{\rho}^{(1)}$ and $\hat{v}_i^{(1)} = \hat{v}_i^{(1)}$.

Now, let us calculate $\hat{p}_{ij}^{(1)}$ from Eq. (C7b), that is,

$$\hat{p}_{ij}^{(1)} = 2\iint_0^\infty \left(\zeta_i - \hat{v}_i^{(0)}\right)\left(\zeta_j - \hat{v}_j^{(0)}\right)\hat{f}^{(1)}d\hat{\mathcal{E}}d\boldsymbol{\zeta}$$

$$= 2\iint_0^\infty \left(\zeta_i - \hat{v}_i^{(0)}\right)\left(\zeta_j - \hat{v}_j^{(0)}\right)\left(\hat{f}^{(0)}\Psi^{(1)} - \frac{1}{\hat{A}_c^{(0)}\hat{\rho}^{(0)}}\zeta_k\frac{\partial\hat{f}^{(0)}}{\partial y_k}\right)d\hat{\mathcal{E}}d\boldsymbol{\zeta}. \tag{C35}$$

The calculation of the term containing $\Psi^{(1)}$ is straightforward. The term containing $\partial\hat{f}^{(0)}/\partial y_k$ can be calculated conveniently as follows. Let $c_i = \zeta_i - \hat{v}_i^{(0)}$ and write $(\zeta_i - \hat{v}_i^{(0)})(\zeta_j - \hat{v}_j^{(0)})\zeta_k\partial\hat{f}^{(0)}/\partial y_k$ as

$$c_i c_j \zeta_k \frac{\partial\hat{f}^{(0)}}{\partial y_k} = c_i c_j c_k \frac{\partial\hat{f}^{(0)}}{\partial y_k} + \hat{v}_k^{(0)}c_i c_j \frac{\partial\hat{f}^{(0)}}{\partial y_k}$$

$$= \frac{\partial}{\partial y_k}(c_i c_j c_k \hat{f}^{(0)}) + \frac{\partial\hat{v}_i^{(0)}}{\partial y_k}c_j c_k \hat{f}^{(0)} + c_i\frac{\partial\hat{v}_j^{(0)}}{\partial y_k}c_k \hat{f}^{(0)} + c_i c_j\frac{\partial\hat{v}_k^{(0)}}{\partial y_k}\hat{f}^{(0)}$$

$$+ \hat{v}_k^{(0)}\frac{\partial}{\partial y_k}(c_i c_j \hat{f}^{(0)}) + \hat{v}_k^{(0)}\frac{\partial\hat{v}_i^{(0)}}{\partial y_k}c_j \hat{f}^{(0)} + \hat{v}_k^{(0)}c_i\frac{\partial\hat{v}_j^{(0)}}{\partial y_k}\hat{f}^{(0)}. \tag{C36}$$

Taking into account the relations

$$\iint_0^\infty c_i\hat{f}^{(0)}d\hat{\mathcal{E}}d\boldsymbol{\zeta} = \iint_0^\infty c_i c_j c_k\hat{f}^{(0)}d\hat{\mathcal{E}}d\boldsymbol{\zeta} = 0, \quad \iint_0^\infty c_i c_j\hat{f}^{(0)}d\hat{\mathcal{E}}d\boldsymbol{\zeta} = \frac{1}{2}\hat{\rho}^{(0)}\hat{T}_{\text{tr}}^{(0)}\delta_{ij}, \tag{C37}$$

we can immediately integrate Eq. (C36) to obtain

$$2 \iint_0^\infty c_i c_j \zeta_k \frac{\partial \hat{f}^{(0)}}{\partial y_k} d\hat{\mathcal{E}} d\boldsymbol{\zeta} = \hat{\rho}^{(0)} \hat{T}_{\mathrm{tr}}^{(0)} \left(\frac{\partial \hat{v}_i^{(0)}}{\partial y_j} + \frac{\partial \hat{v}_j^{(0)}}{\partial y_i} + \frac{\partial \hat{v}_k^{(0)}}{\partial y_k} \delta_{ij} \right) + \hat{v}_k^{(0)} \frac{\partial}{\partial y_k} (\hat{\rho}^{(0)} \hat{T}_{\mathrm{tr}}^{(0)}) \delta_{ij}. \quad \text{(C38)}$$

As the result, Eq. (C35) leads to the following expression of $\hat{p}_{ij}^{(1)}$:

$$\hat{p}_{ij}^{(1)} = (\hat{\rho}^{(0)} \hat{T}_{\mathrm{tr}}^{(1)} + \hat{\rho}^{(1)} \hat{T}_{\mathrm{tr}}^{(0)}) \delta_{ij} + \frac{1}{1-\nu} \hat{\rho}^{(0)} (\hat{T}^{(0)} - \hat{T}_{\mathrm{tr}}^{(0)}) \delta_{ij}$$

$$- \frac{1}{1-\nu} \frac{\hat{T}_{\mathrm{tr}}^{(0)}}{\hat{A}_c^{(0)}} \left(\frac{\partial \hat{v}_i^{(0)}}{\partial y_j} + \frac{\partial \hat{v}_j^{(0)}}{\partial y_i} + \frac{\partial \hat{v}_k^{(0)}}{\partial y_k} \delta_{ij} \right) - \frac{1}{1-\nu} \frac{\hat{v}_k^{(0)}}{\hat{A}_c^{(0)} \hat{\rho}^{(0)}} \frac{\partial}{\partial y_k} (\hat{\rho}^{(0)} \hat{T}_{\mathrm{tr}}^{(0)}) \delta_{ij}. \quad \text{(C39)}$$

In this way, we obtain the expression of $\hat{p}_{ij}^{(1)}$ in terms of $\hat{\rho}^{(1)}$ and $\hat{T}_{\mathrm{tr}}^{(1)}$ and the zeroth-order quantities.

Next, let us calculate $\hat{T}_{\mathrm{tr}}^{(1)}$ from Eq. (C8), i.e., $\hat{\rho}^{(0)} \hat{T}_{\mathrm{tr}}^{(1)} + \hat{\rho}^{(1)} \hat{T}_{\mathrm{tr}}^{(0)} = (1/3) \hat{p}_{kk}^{(1)}$. If we calculate $\hat{p}_{kk}^{(1)}$ by contracting Eq. (C39) and using it in this relation, the term $\hat{\rho}^{(0)} \hat{T}_{\mathrm{tr}}^{(1)} + \hat{\rho}^{(1)} \hat{T}_{\mathrm{tr}}^{(0)}$ is canceled, and we are left with the following relation:

$$\hat{v}_k^{(0)} \frac{\partial \hat{T}_{\mathrm{tr}}^{(0)}}{\partial y_k} = \hat{A}_c^{(0)} \hat{\rho}^{(0)} (\hat{T}^{(0)} - \hat{T}_{\mathrm{tr}}^{(0)}) - \frac{2}{3} \hat{T}_{\mathrm{tr}}^{(0)} \frac{\partial \hat{v}_k^{(0)}}{\partial y_k}, \quad \text{(C40)}$$

where use has been made of Eq. (C34a). Because of the relations

$$\hat{A}_c^{(0)} = \hat{A}_c(\hat{T}^{(0)}), \quad \hat{T}^{(0)} = \frac{3\hat{T}_{\mathrm{tr}}^{(0)} + \delta \hat{T}_{\mathrm{int}}^{(0)}}{3 + \delta}, \quad \text{(C41)}$$

Eq. (C40) is an equation containing only the zeroth-order quantities $\hat{\rho}^{(0)}, \hat{v}_i^{(0)}, \hat{T}_{\mathrm{tr}}^{(0)}$, and $\hat{T}_{\mathrm{int}}^{(0)}$. Therefore, it can be the equation to be added to Eq. (C34) to form a closed set.

Finally, we calculate $\hat{T}_{\mathrm{int}}^{(1)}$ from Eq. (C9), i.e.,

$$\hat{\rho}^{(0)} \hat{T}_{\mathrm{int}}^{(1)} + \hat{\rho}^{(1)} \hat{T}_{\mathrm{int}}^{(0)} = \frac{2}{\delta} \iint_0^\infty \hat{\mathcal{E}} \hat{f}^{(1)} d\hat{\mathcal{E}} d\boldsymbol{\zeta} = \frac{2}{\delta} \iint_0^\infty \hat{\mathcal{E}} \left(\hat{f}^{(0)} \Psi^{(1)} - \frac{1}{\hat{A}_c^{(0)} \hat{\rho}^{(0)}} \zeta_k \frac{\partial \hat{f}^{(0)}}{\partial y_k} \right) d\hat{\mathcal{E}} d\boldsymbol{\zeta}. \quad \text{(C42)}$$

Again, the calculation of the term containing $\Psi^{(1)}$ is straightforward. From the fact that the term $\hat{\mathcal{E}} \zeta_k (\partial \hat{f}^{(0)} / \partial y_k)$ can be transformed into $\hat{\mathcal{E}} (\partial c_k \hat{f}^{(0)} / \partial y_k) + \hat{\mathcal{E}} (\partial \hat{v}_k^{(0)} \hat{f}^{(0)} / \partial y_k)$ and that $\iint_0^\infty \hat{\mathcal{E}} c_k \hat{f}^{(0)} d\hat{\mathcal{E}} d\boldsymbol{\zeta} = 0$ and $\iint_0^\infty \hat{\mathcal{E}} \hat{f}^{(0)} d\hat{\mathcal{E}} d\boldsymbol{\zeta} = (\delta/2) \hat{\rho}^{(0)} \hat{T}_{\mathrm{int}}^{(0)}$ hold, we immediately have

$$\frac{2}{\delta} \iint_0^\infty \hat{\mathcal{E}} \zeta_k \frac{\partial \hat{f}^{(0)}}{\partial y_k} d\hat{\mathcal{E}} d\boldsymbol{\zeta} = \frac{\partial}{\partial y_k} (\hat{v}_k^{(0)} \hat{\rho}^{(0)} \hat{T}_{\mathrm{int}}^{(0)}). \quad \text{(C43)}$$

Then, Eq. (C42) becomes

$$\hat{\rho}^{(0)} \hat{T}_{\mathrm{int}}^{(1)} + \hat{\rho}^{(1)} \hat{T}_{\mathrm{int}}^{(0)} = \hat{\rho}^{(1)} \hat{T}_{\mathrm{int}}^{(0)} + \hat{\rho}^{(0)} \hat{T}_{\mathrm{int}}^{(1)} + \hat{\rho}^{(0)} (\hat{T}^{(0)} - \hat{T}_{\mathrm{int}}^{(0)}) - \frac{1}{\hat{A}_c^{(0)} \hat{\rho}^{(0)}} \frac{\partial}{\partial y_k} (\hat{v}_k^{(0)} \hat{\rho}^{(0)} \hat{T}_{\mathrm{int}}^{(0)}), \quad \text{(C44)}$$

which gives, with the help of Eq. (C34a),

$$\hat{v}_k^{(0)} \frac{\partial \hat{T}_{\mathrm{int}}^{(0)}}{\partial y_k} = \hat{A}_c^{(0)} \hat{\rho}^{(0)} (\hat{T}^{(0)} - \hat{T}_{\mathrm{int}}^{(0)}). \quad \text{(C45)}$$

From Eq. (C41), this is also an equation containing $\hat{\rho}^{(0)}, \hat{v}_i^{(0)}, \hat{T}_{\mathrm{tr}}^{(0)}$, and $\hat{T}_{\mathrm{int}}^{(0)}$, which can be another candidate of the equation to be added to Eq. (C34) to form a closed set.

Here, we should note the fact that we can recover Eq. (C34c) by adding Eq. (C40) $\times 3\hat{\rho}^{(0)}$ and Eq. (C45) $\times \delta\hat{\rho}^{(0)}$. Therefore, only two equations out of Eqs. (C34c), (C40), and (C45) are independent.

In summary, the zeroth-order quantities $\hat{\rho}^{(0)}$, $\hat{v}_i^{(0)}$, $\hat{T}_{\text{tr}}^{(0)}$, and $\hat{T}_{\text{int}}^{(0)}$ are governed by Eqs. (C34a) and (C34b) and two equations out of Eqs. (C34c), (C40), and (C45). This scheme should also work in the higher order. For instance, from the compatibility condition for the equation for $\hat{f}^{(2)}$, we obtain the counterparts of Eq. (C34) for the first-order variables $\hat{\rho}^{(1)}$, $\hat{v}_i^{(1)}$, $\hat{T}_{\text{tr}}^{(1)}$, and $\hat{T}_{\text{int}}^{(1)}$. Then, by calculating $\hat{T}_{\text{tr}}^{(2)}$ and $\hat{T}_{\text{int}}^{(2)}$ with $\hat{f}^{(2)}$, we derive the two counterparts of Eqs. (C40) and (C45) for the first-order variables. We use the counterparts of Eqs. (C34a) and (C34b) and choose two from the counterparts of Eqs. (C34c), (C40), and (C45) to have a closed set for $\hat{\rho}^{(1)}$, $\hat{v}_i^{(1)}$, $\hat{T}_{\text{tr}}^{(1)}$, and $\hat{T}_{\text{int}}^{(1)}$.

It should be remarked that Eqs. (C34) and (C40) [or (C45)] are essentially the same as the macroscopic equations for six macroscopic variables derived in [31,32] if the slowly varying variables corresponding to y_i [Eq. (49)] are used in the latter equations. These equations, which are not restricted to slowly varying solutions, are obtained by the theory of extended thermodynamics [31] or by an appropriate moment closure based on kinetic theory [31,32]. On the other hand, Eqs. (C34) and (C40) [or (C45)], which are restricted to slowly varying solutions, are derived without any moment-closure assumption. We should also mention that the macroscopic equations for six macroscopic variables have been extended to the case of a thermally perfect (or nonpolytropic) gas for which the specific heats at constant pressure and at constant volume are both temperature dependent [46].

APPENDIX D: INTEGRAL IN EQ. (64)

In this Appendix, we summarize the explicit form of the indefinite integral of the integral in Eq. (64) for $\hat{A}_c(\hat{T}) = 1$, $\hat{T}$, and $\sqrt{\hat{T}}$.

Case of $\hat{A}_c(\hat{T}) = 1$:

$$\int \frac{u^2(\hat{v}_* - u)}{(\hat{v}_- - u)(u - \hat{v}_+)} du = \frac{1}{2}u^2 + Au + B \ln(\hat{v}_- - u) + C \ln(u - \hat{v}_+), \tag{D1a}$$

$$A = \hat{v}_- + \hat{v}_+ - \hat{v}_*, \quad B = \frac{\hat{v}_-^2(\hat{v}_- - \hat{v}_*)}{\hat{v}_- - \hat{v}_+}, \quad C = \frac{\hat{v}_+^2(\hat{v}_* - \hat{v}_+)}{\hat{v}_- - \hat{v}_+}. \tag{D1b}$$

Case of $\hat{A}_c(\hat{T}) = \hat{T}$:

$$(\gamma - 1) \int \frac{u^2(\hat{v}_* - u)}{\hat{T}(u)(\hat{v}_- - u)(u - \hat{v}_+)} du$$

$$= A \ln(\hat{v}_- - u) + B \ln(u - \hat{v}_+) + C \ln((u - \alpha)^2 + \beta^2) + \frac{D}{\beta} \tan^{-1} \frac{u - \alpha}{\beta}, \tag{D2a}$$

$$\alpha = \frac{8}{5}\hat{v}_*, \quad \beta = \sqrt{\frac{1}{\gamma - 1} - \frac{1}{4\hat{v}_-^2}}, \tag{D2b}$$

$$A = \frac{\hat{v}_-^2(\hat{v}_- - \hat{v}_*)}{(\hat{v}_- - \hat{v}_+)[(\hat{v}_- - \alpha)^2 + \beta^2]}, \quad B = \frac{\hat{v}_+^2(\hat{v}_* - \hat{v}_+)}{(\hat{v}_- - \hat{v}_+)[(\hat{v}_+ - \alpha)^2 + \beta^2]}, \tag{D2c}$$

$$C = \frac{1}{2}(1 - A - B), \quad D = (\alpha^2 + \beta^2)\left(\frac{A}{\hat{v}_-} + \frac{B}{\hat{v}_+}\right) + 2\alpha C. \tag{D2d}$$

Case of $\hat{A}_c(\hat{T}) = \sqrt{\hat{T}}$:

$$\sqrt{\gamma - 1} \int \frac{u^2(\hat{v}_* - u)}{\sqrt{\hat{T}(u)}(\hat{v}_- - u)(u - \hat{v}_+)} du$$

$$= A(\ln|t - t_{A+}| - \ln|t - t_{A-}|) + B(\ln|t - t_{B+}| - \ln|t - t_{B-}|) + C(\ln|t + 1| - \ln|t - 1|)$$

$$+ \beta\left(\frac{1}{t + 1} - \frac{1}{t - 1}\right), \tag{D3a}$$

$$t = \frac{\sqrt{(u - \alpha)^2 + \beta^2} - \beta}{u - \alpha}, \quad \alpha = \frac{8}{5}\hat{v}_*, \quad \beta = \sqrt{\frac{1}{\gamma - 1} - \frac{1}{4\hat{v}_-^2}}, \tag{D3b}$$

$$t_{A\pm} = \frac{1}{\hat{v}_- - \alpha}[-\beta \pm \sqrt{(\hat{v}_- - \alpha)^2 + \beta^2}], \quad t_{B\pm} = \frac{1}{\hat{v}_+ - \alpha}[-\beta \pm \sqrt{(\hat{v}_+ - \alpha)^2 + \beta^2}], \tag{D3c}$$

$$A = \frac{\hat{v}_-^2(\hat{v}_- - \hat{v}_*)}{(\hat{v}_- - \hat{v}_+)\sqrt{(\hat{v}_- - \alpha)^2 + \beta^2}}, \quad B = \frac{\hat{v}_+^2(\hat{v}_* - \hat{v}_+)}{(\hat{v}_- - \hat{v}_+)\sqrt{(\hat{v}_+ - \alpha)^2 + \beta^2}}, \tag{D3d}$$

$$C = \hat{v}_- + \hat{v}_+ + \frac{3}{5}\hat{v}_*. \tag{D3e}$$

[1] G. R. Cowan and D. F. Hornig, The experimental determination of the thickness of a shock front in a gas, J. Chem. Phys. **18**, 1008 (1950).

[2] M. Linzer and D. F. Hornig, Structure of shock fronts in argon and nitrogen, Phys. Fluids **6**, 1661 (1963).

[3] H. Alsmeyer, Density profiles in argon and nitrogen shock waves measured by the absorption of an electron beam, J. Fluid Mech. **74**, 497 (1976).

[4] R. E. Caflisch and B. Nicolaenko, Shock profile solutions of the Boltzmann equation, Commun. Math. Phys. **86**, 161 (1982).

[5] T.-P. Liu and S.-H. Yu, Boltzmann equation: Micro-macro decompositions and positivity of shock profiles, Commun. Math. Phys. **246**, 133 (2004).

[6] G. A. Bird, The velocity distribution function within a shock wave, J. Fluid Mech. **30**, 479 (1967).

[7] T. Ohwada, Structure of normal shock waves: Direct numerical analysis of the Boltzmann equation for hard-sphere molecules, Phys. Fluids A **5**, 217 (1993).

[8] M. N. Kogan, *Rarefied Gas Dynamics* (Plenum, New York, 1969).

[9] J. H. Ferziger and H. G. Kaper, *Mathematical Theory of Transport Processes in Gases* (North Holland, Amsterdam, 1972).

[10] C. Cercignani, *The Boltzmann Equation and Its Applications* (Springer, Berlin, 1988).

[11] G. A. Bird, *Molecular Gas Dynamics and the Direct Simulation of Gas Flows* (Oxford University Press, Oxford, 1994).

[12] C. Cercignani, *Rarefied Gas Dynamics: From Basic Concepts to Actual Calculations* (Cambridge University Press, Cambridge, UK, 2000).

[13] Y. Sone, *Molecular Gas Dynamics: Theory, Techniques, and Applications* (Birkhäuser, Boston, 2007).

[14] S. Taniguchi, T. Arima, T. Ruggeri, and M. Sugiyama, Thermodynamic theory of the shock wave structure in a rarefied polyatomic gas: Beyond the Bethe-Teller theory, Phys. Rev. E **89**, 013025 (2014).

[15] T. Ruggeri and M. Sugiyama, *Rational Extended Thermodynamics beyond the Monatomic Gas* (Springer, Cham, Switzerland, 2015).

[16] S. Taniguchi, T. Arima, T. Ruggeri, and M. Sugiyama, Overshoot of the non-equilibrium temperature in the shock wave structure of a rarefied polyatomic gas subject to the dynamic pressure, Int. J. Non-Linear Mech. **79**, 66 (2016).

[17] H. A. Bethe and E. Teller, Deviations from thermal equilibrium in shock waves, Office of Scientific and Technical Information, Office of Science, US Department of Energy, Report No. NP-4898; BRL-X-117, https://www.osti.gov/scitech/servlets/purl/4420349; cited in Ref. [14].

[18] Ya. B. Zel'dovich and Yu. P. Raizer, *Physics of Shock Waves and High-Temperature Hydrodynamic Phenomena* (Dover, Mineola, NY, 2002).

[19] N. H. Johannesen, H. K. Zienkiewicz, P. A. Blythe, and J. H. Gerrard, Experimental and theoretical analysis of vibrational relaxation regions in carbon dioxide, J. Fluid Mech. **13**, 213 (1962).

[20] T. Arima, S. Taniguchi, T. Ruggeri, and M. Sugiyama, Extended thermodynamics of dense gases, Continuum Mech. Thermodyn. **24**, 271 (2012).

[21] M. Pavić, T. Ruggeri, and S. Simić, Maximum entropy principle for rarefied polyatomic gases, Phys. A (Amsterdam, Neth.) **392**, 1302 (2013).

[22] J.-F. Bourgat, L. Desvillettes, P. Le Tallec, and B. Perthame, Microreversible collisions for polyatomic gases and Boltzmann's theorem, Eur. J. Mech. B **13**, 237 (1994).

[23] S. Kosuge, K. Aoki, and T. Goto, Shock wave structure in polyatomic gases: Numerical analysis using a model Boltzmann equation, in *Thirtieth International Symposium on Rarefied Gas Dynamics*, edited by A. Ketsdever and H. Struchtrup, AIP Conf. Proc. No. 1786 (AIP, New York, 2016), p. 180004.

[24] L. H. Holway Jr., New statistical models for kinetic theory: Methods of construction, Phys. Fluids **9**, 1658 (1966).

[25] P. Andries, P. Le Tallec, J.-P. Perlat, and B. Perthame, The Gaussian-BGK model of Boltzmann equation with small Prandtl number, Eur. J. Mech. B **19**, 813 (2000).

[26] S. Brull and J. Schneider, On the ellipsoidal statistical model for polyatomic gases, Continuum Mech. Thermodyn. **20**, 489 (2009).

[27] C. Cercignani and M. Lampis, On the H-theorem for polyatomic gases, J. Stat. Phys. **26**, 795 (1981).

[28] G. Emanuel, Bulk viscosity of a dilute polyatomic gas, Phys. Fluids A **2**, 2252 (1990).

[29] M. S. Cramer, Numerical estimates for the bulk viscosity of ideal gases, Phys. Fluids **24**, 066102 (2012).

[30] M. Pavić-Čolić, D. Madjarević, and S. Simić, Polyatomic gases with dynamic pressure: Kinetic non-linear closure and the shock structure, Int. J. Non-Linear Mech. **92**, 160 (2017).

[31] T. Arima, S. Taniguchi, T. Ruggeri, and M. Sugiyama, Extended thermodynamics of real gases with dynamic pressure: An extension of Meixner's theory, Phys. Lett. A **376**, 2799 (2012).

[32] T. Ruggeri, Non-linear maximum entropy principle for a polyatomic gas subject to the dynamic pressure, Bull. Inst. Math., Acad. Sinica (New Ser.) **11**, 1 (2016).

[33] I. V. Alekseev and E. V. Kustova, Shock wave structure in CO_2 taking into account bulk viscosity. Vestnik SPbSU. Mathematics, Mech. Astron. **4**, 642 (2017).

[34] H. Funagane, S. Takata, K. Aoki, and K. Kugimoto, Poiseuille flow and thermal transpiration of a rarefied polyatomic gas through a circular tube with applications to microflows, Bollettino dell'Unione Matematica Italiana Ser. 9, **4**, 19 (2011).

[35] F. J. Uribe, E. A. Mason, and J. Kestin, Thermal conductivity of nine polyatomic gases at low density, J. Phys. Chem. Ref. Data **19**, 1123 (1990).

[36] R. Span and W. Wagner, A new equation of state for carbon dioxide covering the fluid region from the triple-point temperature to 1100 K at pressures up to 800 MPa, J. Phys. Chem. Ref. Data **25**, 1509 (1996).

[37] *JSME Data Book: Thermophysical Properties of Fluids* (Japan Society of Mechanical Engineers, Tokyo, 1983).

[38] E. Kustova (private communication).

[39] V. Vesovic, W. A. Wakeham, G. A. Olchowy, J. V. Sengers, J. T. R. Watson, and J. Millat, The transport properties of carbon dioxide, J. Phys. Chem. Ref. Data **19**, 763 (1990).

[40] E. V. Kustova, E. A. Nagnibeda, Yu. D. Shevelev, and N. G. Syzranova, Comparison of different models for non-equilibrium CO_2 flows in a shock layer near a blunt body, Shock Waves **21**, 273 (2011).

[41] M. Groppi, A. Rossani, and G. Spiga, Fluid-dynamic model equations for a gas with slow reversible bimolecular reactions, Commun. Math. Sci. **7**, 143 (2009).

[42] W. E. Meador, G. A. Miner, and L. W. Townsend, Bulk viscosity as a relaxation parameter: Fact or fiction?, Phys. Fluids **8**, 258 (1996).

[43] C. Borgnakke and P. S. Larsen, Statistical collision model for Monte Carlo simulation of polyatomic gas mixture, J. Comp. Phys. **18**, 405 (1975).

[44] M. Groppi and G. Spiga, Kinetic approach to chemical reactions and inelastic transitions in a rarefied gas, J. Math. Chem. **26**, 197 (1999).

[45] M. Bisi and M. J. Cáceres, A BGK relaxation model for polyatomic gas mixtures, Commun. Math. Sci. **14**, 297 (2016).

[46] M. Bisi, T. Ruggeri, and G. Spiga, Dynamical pressure in a polyatomic gas: Interplay between kinetic theory and extended thermodynamics, Kinet. Relat. Mod. **11**, 71 (2018).